COMBINATORIAL SYNTHESIS AND HIGH-THROUGHPUT CHARACTERIZATION OF POLYURETHANEUREAS AND THEIR NANOCOMPOSITES WITH LAPONITE

A Thesis

Presented to

The Academic Faculty

by

Joe-Lahai Sormana

In Partial Fulfillment

of the Requirements for the Degree

Doctor of Philosophy in Chemical Engineering

Georgia Institute of Technology
August, 2005

COMBINATORIAL SYNTHESIS AND HIGH-THROUGHPUT CHARACTERIZATION OF POLYURETHANEUREAS AND THEIR NANOCOMPOSITES WITH LAPONITE

Approved by:

Dr. J. Carson Meredith, Advisor
School of Chemical and Biomolecular Engineering
Georgia Institute of Technology

Dr. William J. Koros
School of Chemical and Biomolecular Engineering
Georgia Institute of Technology

Dr. Peter J. Ludovice
School of Chemical and Biomolecular Engineering
Georgia Institute of Technology

Dr. F. Joseph Schork
School of Chemical and Biomolecular Engineering
Georgia Institute of Technology

Dr. Mohan Srinivasarao
Polymer, Textile and Fiber Engineering
Georgia Institute of Technology

Date Approved: August 5, 2005

“Life is like a page, please turn to the next one”

-Anonymous

Dedicated

To my Mother

For everything

ACKNOWLEDGEMENTS

I am deeply grateful to everyone who helped me successfully complete my graduate studies. I would like to thank my thesis advisor, Dr. J. Carson Meredith, for his unwavering support and encouragement over the past five years. Thank you for your guidance, and also for the wealth of knowledge that I have acquired from you. Your work habit serves as a model that I strive to emulate. I would like to thank the members of the Meredith Research Group for all your contributions to my success in graduate school. Especially I thank Dr. Santanu Chattopadhyay, for all your input and suggestions on a significant portion of this dissertation.

I would also like to thank my thesis committee members, Dr. William J. Koros, Dr. Peter J. Ludovice, Dr. F. Joseph Schork and Dr. Mohan Srinivasarao for agreeing to serve on my committee. Jeffrey T. Andrews and Bradley K. Parker were very helpful in the design and construction of the high-throughput mechanical apparatus. Thanks to Air Products & Chemicals and ARKEMA for providing materials and financial support. I would also like to thank 3M Corporation for supporting a GEM Fellowship.

Thanks to my family, especially my mother and my sister, for your high expectations of me, and also for your support throughout my academic trials. I would also like to thank my wife, Amie, for her support and immense patience and understanding while I completed my studies. Finally, I would like to thank the almighty God for giving me the strength and courage needed to endure and overcome all challenges associated with obtaining a graduate degree.

TABLE OF CONTENTS

LIST OF TABLES

LIST OF FIGURES

SUMMARY

Segmented polyurethaneureas (SPUU) are thermoplastic elastomers with excellent elastic properties, high abrasion resistance and tear strength, making them very useful in numerous industrial applications ranging from microelectronics (slurry pad) to biomedical (artificial heart vessels) applications. The elastic and mechanical properties of these materials are strongly influenced by their two phase morphology. The factors that influence phase separation include difference in polarity between the hard and soft phases, ***composition*** and ***temperature***. In general good phase separation results in materials with superior mechanical and elastic properties. Due to the immense potential applications of SPUU elastomers, there is a need for materials with higher strength. However, higher strength is not desired at the detriment of elasticity. If fact, stronger materials with enhanced elasticity are desired. In this thesis, high-strength SPUU elastomers were synthesized by incorporating reactive Laponite® particles with surface-active free amine. The synthesis of pure SPUU is very complex, and addition of a reactive silicate further increases the complexity. To remedy this challenge, combinatorial methods and high-throughput screening techniques were used to optimize the diamine concentration and cure temperature. It was determined that pure SPUU elastomers prepared at a diamine stoichiometry of 85 – 100 mole %, and cured at 90 – 95 ^{o}C produced materials with higher strength and elongation at break. SPUU nanocomposites were prepared by maintaining the overall diamine stoichiometry at 95 mole %, and cured at 90 ^{o}C. Uniaxial tensile strength was optimized at a particle weight

fraction of 1 wt. %, with a nearly 200 % increase in tensile strength and a 40 % increase in elongation at break, compared to pristine SPUU.

CHAPTER 1

INTRODUCTION

Recent developments in the synthesis of polymer/silicate nanocomposites have shown that incorporation of reactive silicates as chain extenders in polyurethane networks can improve the tensile properties.[1, 2] Improvement in tensile properties can be achieved at a lower silicate content compared to nanocomposites resulting from physical mixing of the polymer and the silicate.[2] The primary objective of this dissertation is to synthesize high-strength segmented polyurethaneurea nanocomposites. This goal is achieved by chemically incorporating Laponite® particles through covalent bonding with the polymer matrix. The synthesis of segmented polyurethaneurea (SPUU) is inherently complex, and the addition of reactive particles to make SPUU nanocomposites further increases the complexity. Combinatorial Methods (CM), an alternative approach in polymer research, is employed to rapidly screen the large range of parameters needed to synthesize these nanocomposites. This chapter provides a brief introduction to concepts germane to achieving the objective stated above. An outline describing the remaining chapters in this document is also presented in this chapter.

1.1 MOTIVATION

Segmented Polyurethaneurea (SPUU) elastomers are physically and chemically crosslinked materials with alternating rubbery (soft) and glassy or crystalline (hard) segments. Physical crosslinking is caused by a two-phase morphology due to the incompatibility of the soft and hard phases. The factors that influence phase separation include difference in polarity and chemical composition of the hard and soft phases, length of the segments, crystallizability of the hard or soft segment, hydrogen bonding within and between the segments, composition and temperature.[3, 4] The hard segment of SPUU is the product of a polyaddition reaction between a diisocyanate and a multi-functional amine. The soft segment is usually composed of low molecular weight (500 g/mol – 5000 g/mol) polyester or polyether diol. The hard segment provides physical crosslinks that act as reinforcing fillers for the soft matrix. The study of SPUU elastomers has attracted tremendous attention because of their superior mechanical properties, such as high elasticity and strength. The soft segment contributes high extension and elasticity, while the hard segment contributes to modulus and strength. These properties are sensitive functions of the two-phase morphology, strength of the hydrogen bonding, and the rate of urethane and urea forming reactions[5-9], which in turn depends on the factors listed above.

The large parameter space involved in the processing of these materials challenges the conventional paradigm of 1-sample-1-measurement synthesis and characterization. Adding a reactive Laponite® particle to synthesize SPUU nanocomposites further increases the challenges in processing these materials. Combinatorial sample preparation techniques[10, 11] and high-throughput screening

techniques allows accurate and rapid investigation of the effect of processing parameters on the mechanical properties of SPUU . These methods allow accelerated discovery of materials with desired properties and the development of structure-property relationships. Here, combinatorial synthesis and high-throughput screening techniques are used to determine the optimum conditions of cure temperature and chain extender concentration for producing strong SPUU elastomers. SPUU nanocomposites are prepared by varying the reactive particle concentration, while maintaining the final chain extender concentration and cure temperature at the optimum values determined from combinatorial and high-throughput studies.

1.2 BACKGROUND

The general term "polyurethanes" is used to describe a broad class of polymers prepared by polyaddition polymerization between a di- or poly-isocyanate with compounds containing two or more hydroxyl or amino groups.[3, 12, 13] The urethane group [-NHCO-O-] formed in these polyaddition reactions is a characteristic feature common to all polyurethanes. Other polymers such as polyurethaneureas are also referred to as polyurethanes because they contain some amount of urethane-groups. Polyurethane is a versatile polymeric material which can be tailored to meet the diversified demands of modern technologies such as coatings, plastics, fibers, artificial heart and blood vessels, foams, textiles, paints, rubber, elastomers and composites.[5, 8, 9, 14]

Due to the immense industrial importance of polyurethanes, the chemistry of isocyanate and the polyaddition reaction has been studied extensively. Isocyanates are very reactive and allow easy conversion into urethanes and ureas.[3, 13] The high reactivity

of isocyanates also leads to unwanted reactions with water or with urethane or urea groups to form allophanates and biurets respectively. Hence, moisture and stoichiometry of the reactants must be carefully controlled to prevent byproduct formation. For the sake of clarity, segmented polyurethane elastomers as depicted in Figure 1.1 can be divided into two groups. The first group is characterized by the presence of urethane linkages in the hard segment, and the other is characterized by the presence of urea linkages in the hard segment. Segmented polyurethane elastomers with urea linkages in the hard segments are called segmented polyurethaneurea. It has been shown that SPUU elastomers have superior mechanical properties compared to segmented polyurethanes.[15] This is because the incorporation of urea linkages in the hard segments leads to stronger hydrogen bonds in the hard domains and enhanced phase separation.[4, 7, 16-18]

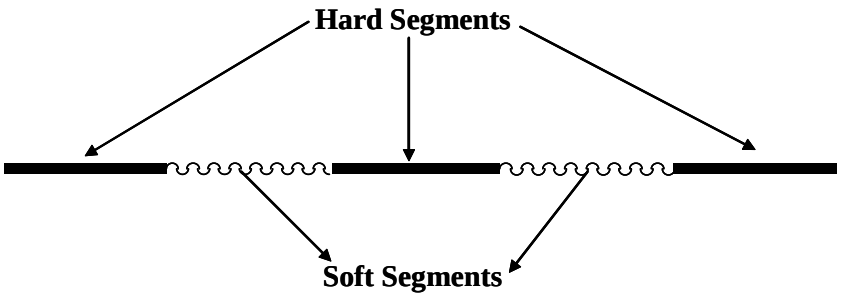

Figure 1.1: Schematic representation of segmented polyurethane.

1.2.1 Polyurethane Elastomer Chemistry

Below is a list of representative polyaddition reactions in polyurethane formation:

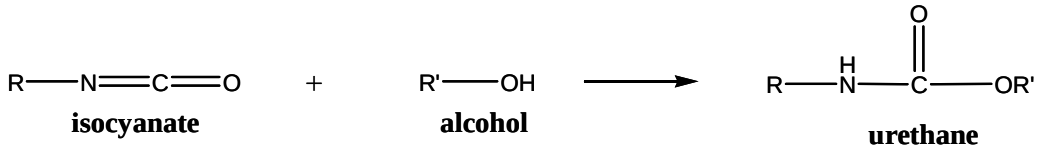

(1.1)

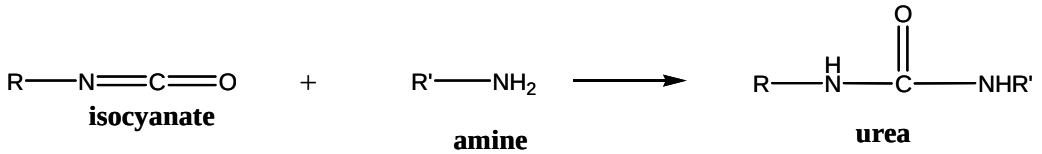

(1.2)

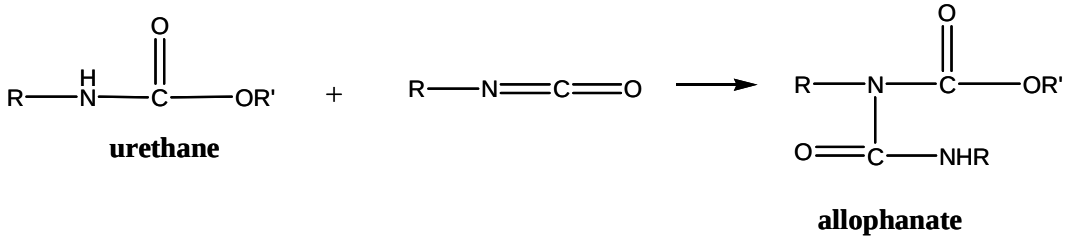

(1.3)

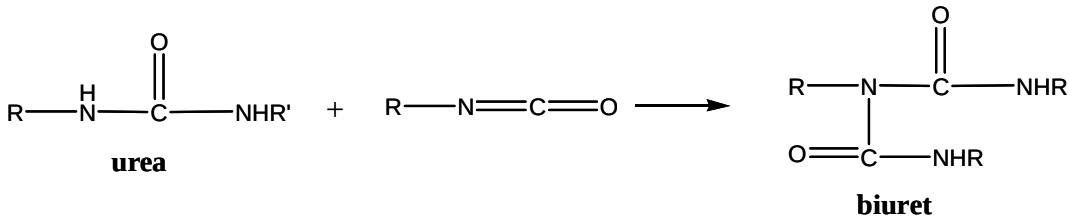

(1.4)

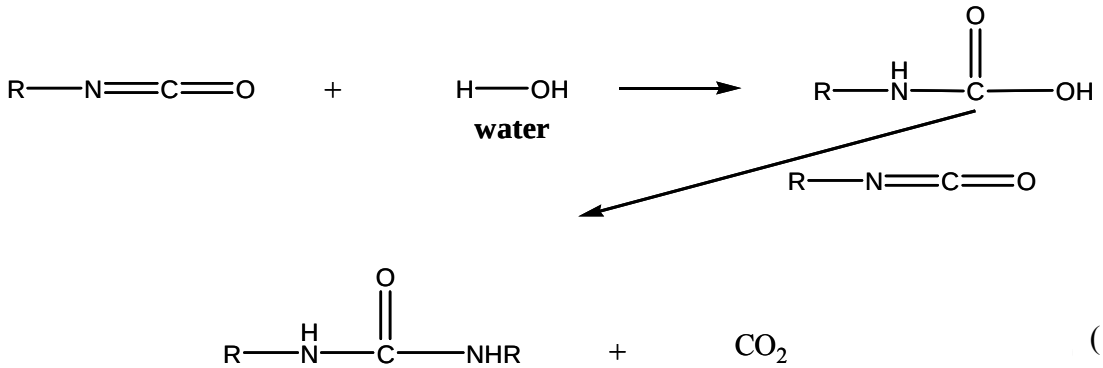

(1.5)

For synthesis of thermoplastic polyurethane elastomers, where crosslinking occurs by physical phase-separation of hard and soft domains, reactions (1.1) and (1.2) are desirable. The reaction path and hence the final product (urethane or urea) depends on whether a hydroxyl or amine curative is reacted with the isocyanate. Water's ubiquitous nature makes it difficult to suppress reaction (1.5), and a small amount of water is usually present in commercially available solvents. Formation of allophanates and biurets at high temperatures (100 ^{o}C – 150 ^{o}C) and also at low temperatures in the presence of excess diisocyanate,[3, 13] lead to chemical crosslinking in polyurethanes. Chemical crosslinks in the polyurethane network tend to prevent hard segment crystallization, increasing phase mixing and form a more homogenous network. These changes in the two-phase morphology of segmented polyurethanes lead to an increase in the soft segment glass transition temperature and a broadening of the glass transition region.[18-22]

1.2.2 Phase-Separation and Hydrogen Bonding in Segmented Polyurethanes

As stated above, segmented polyurethanes are a two-phase system, with alternating hard and soft phases. Figure 1.2 (a) shows an ideally phase-separated polyurethane network. However, the network of most synthesized polyurethane materials is far from ideal. As shown in Figure 1.2 (b), polyurethane networks are marked by some degree of phase mixing, wherein hard segments are found within soft segment domains, and soft segments within hard segments domains. Hard segment lengths and distribution of lengths also varies within the polyurethane network. The mechanical properties of polyurethanes are strongly dependent on the kind and strength of hydrogen bonding within the hard segment, which influences the degree of phase mixing in polyurethanes. Phase mixing in segmented polyurethanes have been studied using Digital Scanning

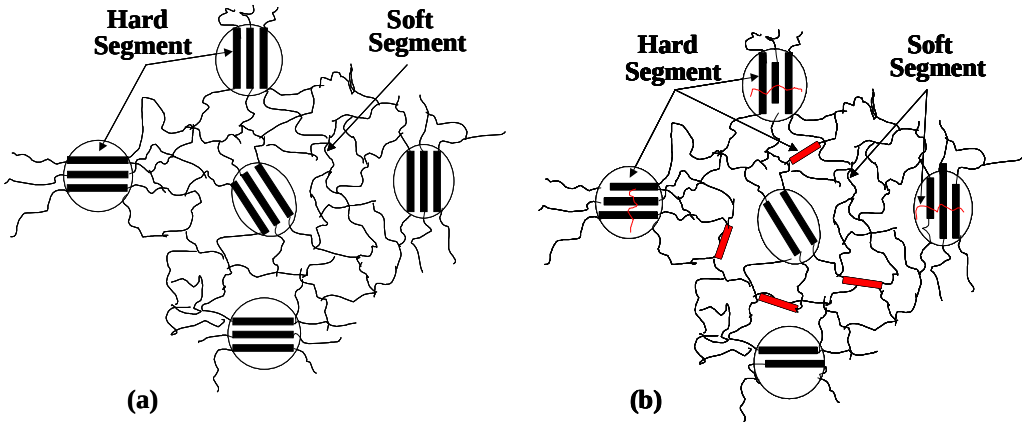

Figure 1.2: Schematic representation of the morphology of segmented polyurethane network: (a) ideally phase separated network, (b) mixed phase network.

Calorimetry (DSC), X-ray diffraction, Transmission Electron microscope (TEM) if there is enough contrast between the hard and soft phases, SEM, AFM and FTIR.[4, 6, 8, 9, 23, 24,25-34] FTIR can be used to measure the degree of phase mixing by analyzing the IR spectra and estimating the degree of interurethane or interurea hydrogen bonding.

The perfection and degree of phase separation, which is reflected in the size and perfection of the domains has been studied successfully using FTIR, because of the existence of bands sensitive to mixed and phase separated states.[3] Polyurethanes and polyurethaneureas are capable of forming different kind of hydrogen bonds. Invariably, the hydrogen bond donor is the hydrogen atom on the N-H group in the urethane or urea linkage. Potential hydrogen bond acceptors are: (1) the carbonyl oxygen in urethane or urea linkages, (2) adjacent ether oxygen or nitrogen in the urethane or urea linkages respectively, (3) carbonyl and adjacent oxygen atom when a polyester soft segment is used, and (4) ether oxygen when a polyether soft segment is used. Hydrogen bonding in polyurethanes (see Figure 1.3) and polyurethaneureas is manifested by shifts in the N-H and C=O stretching frequencies to lower values compared to non-hydrogen bonding N-H and C=O groups.[17, 24] The stretching frequency range for the N-H and C=O groups in polyurethanes and polyurethaneureas are (ν = 3200 – 3500 cm^{-1}) and (ν = 1600 – 1740 cm^{-1}) respectively.

Quantitative analysis of the degree of hydrogen bonding is usually conducted using peaks in the carbonyl region. This is because the carbonyl stretching vibration is sensitive to long-range order in the phases, and the peaks ('free' non-hydrogen bonded, ordered and disordered hydrogen bonded) in this region can be differentiated easily.[24]

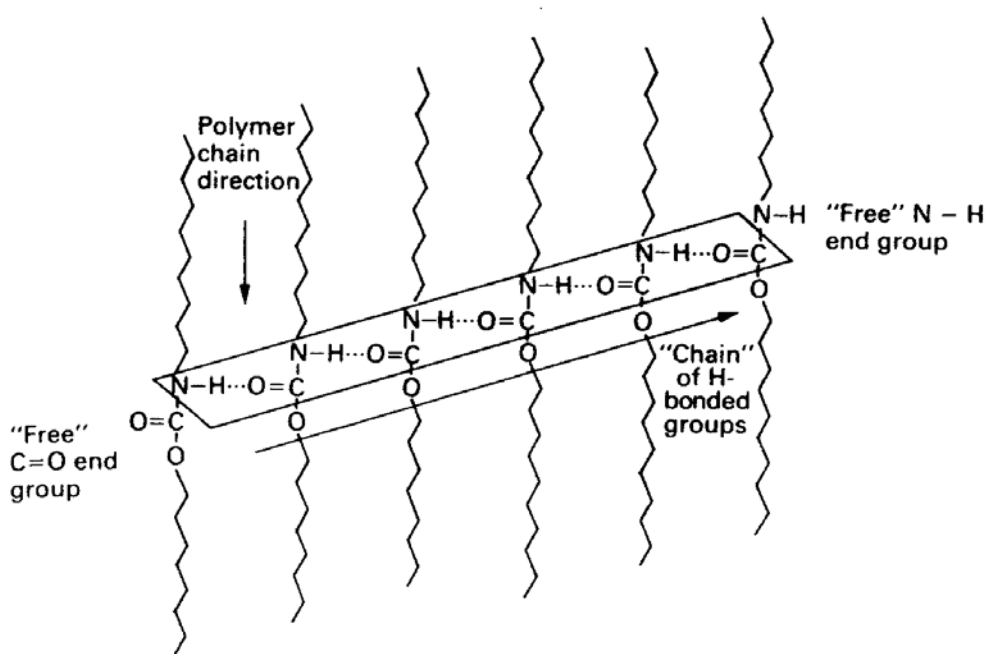

Figure 1.3: A representation of hydrogen bond formation in polyurethanes.[3]

Also, the strength of hydrogen bonds decreases with increase in temperature, and the absorptivity coefficient strongly depends on the strength of the hydrogen bonds.[6] Unlike the N-H stretching mode, the three different peaks in the carbonyl region have similar absorptivity coefficients, making the carbonyl region more suitable for quantitative measurements of free and bonded hydrogen atoms.[4, 35] The equation shown below[4] has been used to characterize the degree of phase mixing.

$$X_b = \frac{C_B}{C_F + C_B} = \frac{A_B / \varepsilon_B}{A_F / \varepsilon_F + A_B / \varepsilon_B} \tag{1.6}$$

A, C and ϵ are the absorbance, concentration, and absorptivity coefficient respectively. The subscripts (b) and (f) represent bonded and free carbonyl groups. A quantitative determination of the fraction of ordered and disordered phase hydrogen bonding is central to understanding the degree of phase-separation. Improvements in the degree of phase separation in SPUU is attributed to the very large polarity difference between hard and soft segments relative to urethanes, and the potential formation of a three-dimensional hydrogen bonding network (see Figure 1.4).[36, 37] In this three-dimensional network, a single urea carbonyl is bonded to two N-H groups in a nonplanar configuration.[36]

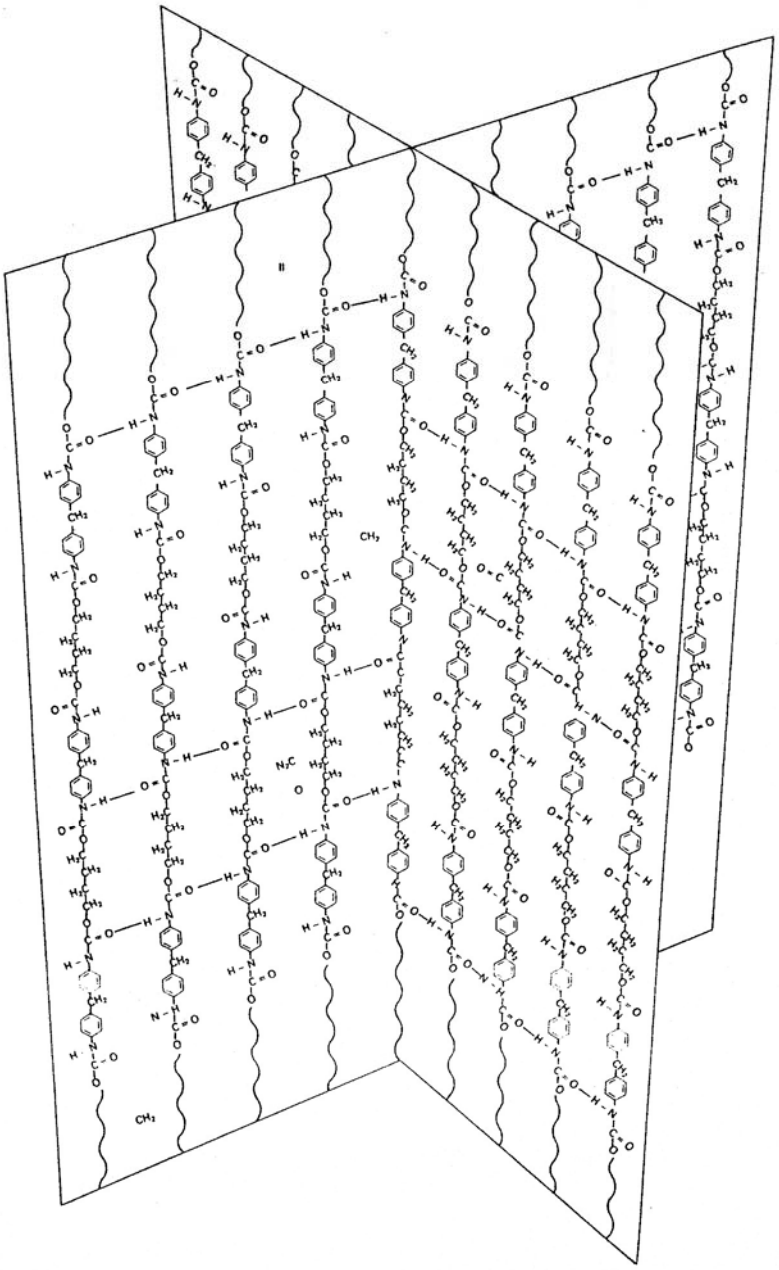

Figure 1.4: Three-dimensional hydrogen bonding network in polyurethanes.[36]

1.3 COMBINATORIAL METHODS AND HIGH-THROUGHPUPUT MEASUREMENTS

Combinatorial Methods (CM) can be thought of as a set of sample preparation techniques that allow the study of a combination of parameters within a single sample "library", as opposed to the traditional method of investigating one parameter per sample. Compared with the traditional method of sample preparation, CM also offers the advantage of investigating the combined effect(s) of competing parameters within the sample. CM, used in conjunction with high-throughput characterization of properties, can lead to rapid discovery of materials with desired properties and to efficient development of accurate structure-property relationships.

CM and high-throughput techniques have been utilized by the pharmaceutical industry with great success. Until recently,[10, 11] these techniques were impossible to implement in polymer research, since library preparation equipment was not suitable to accommodate the phase transitions, reactions, transport properties and interfacial phenomena that occur during synthesis and processing of polymers. In addition, a large number of variables, including, composition, processing temperature, and thickness control these complex phenomena, and the parameters involved often counteract one another. Meredith and coworkers[10, 11] have successfully prepared combinatorial polymer films with gradients in compositions, thickness and processing temperature. The introduction of chemical, thermal and thickness gradients drives nonequilibrium processes that will eliminate the gradient over time. The timescale and lengthscale over which gradient library measurements are valid are determined in part by the magnitude of these transport fluxes. For high molecular mass (M_W = 10000 g/mol), it has been shown that the mass transport and flow lengthscale and times are orders of magnitude lower than

those of the measurements, making it possible for properties to be measured near equilibrium.[10, 11, 38] This novel sample preparation technique, can lead to rapid discovery of polymeric materials with desired mechanical, physical and chemical properties.

1.3.1 Thickness Gradient Library

Sample libraries with gradients in thickness are made by placing approximately 50 to 80 μL polymer solution under a 40 mm wide stainless steel knife-edge, inclined at 5^{o} with respect to the substrate. The substrate is placed on a computer-controlled motion stage, which moves the substrate at a constant acceleration in the coat direction as shown in Figure 1.5. This causes the substrate velocity in the coat direction to increase from zero to the final setpoint. The increase in substrate velocity leads to an increase in the fluid volume passing under the knife-edge. This result in polymer films with controllable thickness gradients.

1.3.2 Temperature Gradient Library

In order to investigate the effect of processing temperature on the chemical and physical properties of polymers, uniform samples or samples with gradients in thickness or composition can be placed on a temperature-gradient stage. Samples with gradient in composition or thickness in one direction, should be placed on the temperature gradient in a manner that will ensure orthogonality of the two gradients. The temperature gradient stage, as shown in Figure 1.6 is made of aluminum, with a heat source at one end and a heat sink at the other, maintaining a linear temperature gradient across the stage.

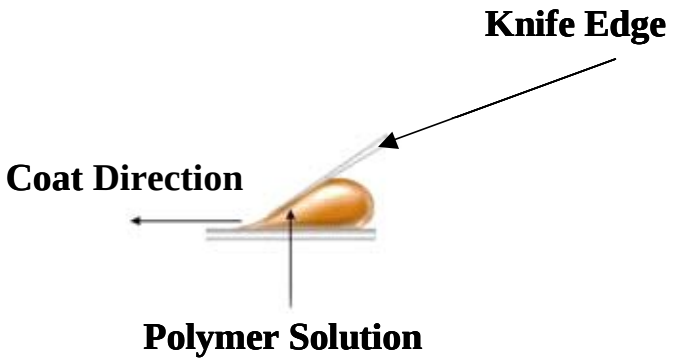

Figure 1.5: Schematic representation of the thickness gradient coating process.

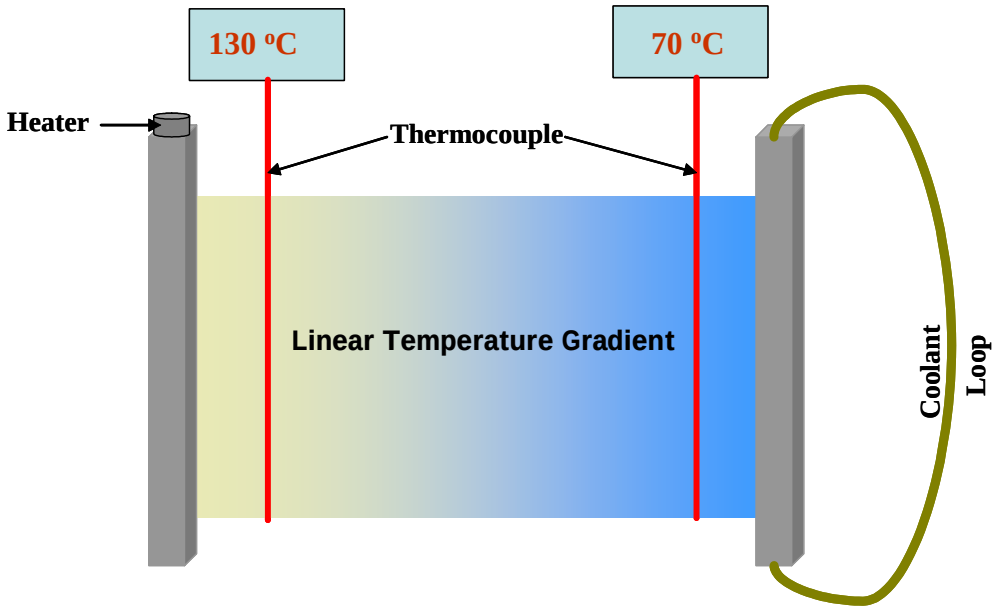

Figure 1.6: Linear temperature gradient stage.

Fourier's law of heat conduction predicts a linear temperature gradient across the stage, and this prediction can be verified by measuring the surface temperature of the stage at different positions. The temperature stage is placed under 1 bar vacuum to minimize oxidation of sample and convective heat transfer from the surface of the substrate.

1.3.3 Composition Gradient Library

Three steps are involved in preparing composition gradient films, as shown in Figure 1.7. Details of this process are discussed in the literature.[10] Two pumps (see Figure 1.7 (a)) introduce and withdraw polymer solutions A and B to and from a small mixing vial at rates I and W. Initially loaded with pure B solution, infusion of solution A causes a time-dependent gradient in composition in the vial. The solution in the vial is continuously stirred throughout the experiment. A small amount of this solution is continuously extracted with an automated sample syringe at a sampling rate S. At the end of the sampling process, the sample syringe contains a solution of polymers A and B with a gradient in composition, ∇x_A, along the length of the syringe needle. The rates I and W control the slope of the composition gradient, which is linear only if I = (W + S)/2. The sample time determines the composition at the endpoint. The gradient solution (Figure 1.7 (b)) is deposited as a thin stripe on the substrate, and then (Figure 1.7 (c)) spread as a film orthogonal to the composition gradient using a knife-edge coater. The solvent evaporates, resulting in a film with a continuous linear gradient in composition from polymer A to polymer B. The remaining solvent is removed under vacuum during annealing. This gradient-mixing process is used to prepare SPUU elastomers with gradients in the diamine curative composition relative to the diisocyanate prepolymer.

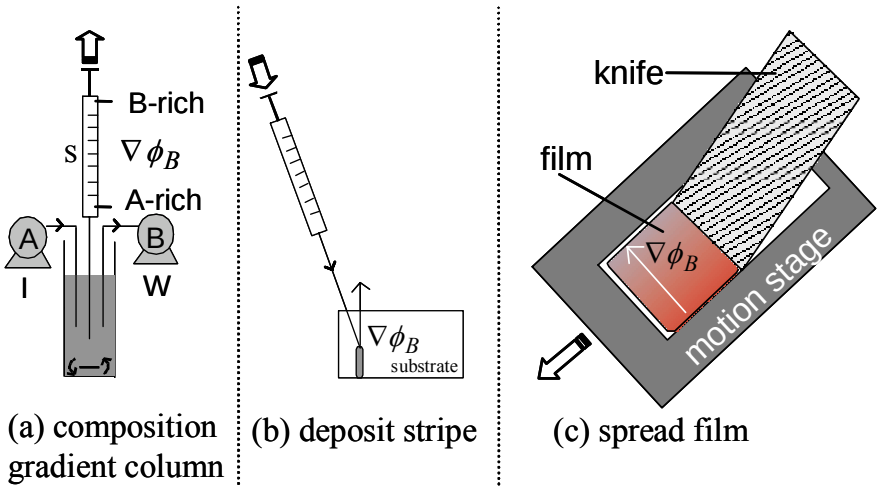

Figure 1.7: Schematic of the composition gradient film coating procedure.

1.4 ELASTOMERS AND RUBBER ELASTICITY

Polymeric elastomers exhibit rubber elastic properties and undergo reversible deformations provided the applied stress is less than the breaking stress. The rubber-elastic behavior of elastomers stems from the storage of elastic strain energy as chains are extended. The ultimate strength is related to the ability to dissipate energy via viscoelasticity, chain rupture, hydrogen bonding, etc. Such behavior requires highly flexible, low glass transition (T_g) chains, i.e. low degree of intermolecular interactions, connected by physical or chemical crosslinks that prevent plastic flow by hindering sliding of chains against their neighbors.[3, 39] Segmented polyurethane and polyurethaneurea elastomers have both physical and chemical crosslinks in their network, and can be explored to first order using the theory of rubber elasticity. Unlike natural rubber, segmented polyurethanes have hard domains that are not point crosslinks. The hard domains act as a filler within the network and are also deformable, which complicates interpretation of experimental results.

1.4.1 The Rubber Elastic State

The equations describing rubber elasticity can be derived from classical thermodynamics based on free energy considerations. Elasticity of rubber is predominantly driven by entropy, rather than energy. This was proposed by Gough (1805), and later confirmed by Lord Kelvin (1857) and Joule (1859) by measuring sample length and force at different temperatures. These measurements revealed that: (1) under constant uniaxial loading, a stretched rubber sample contracts reversibly on heating, (2) heat is generated when rubber is stretched, suggesting that the entropy of

rubber decreased on stretching. The elastic force in stretched rubber is due mainly to the decrease in conformational entropy upon chain stretching.

The classical theory of rubber elasticity is based on the following assumptions: (1) affine deformation, i.e., deformation on the molecular level is the same as that on the macroscopic level, (2) isotropic undeformed network, (3) constant volume during deformation, (4) Gaussian distribution for the end-to-end length of chains in network, (5) fixed crosslinks and (6) the entropy of the network is the sum of the entropies of the individual chains.[39, 40] For a Gaussian distribution of chains, the change in Helmholtz free energy of a single network chain reduces to,

$$\nabla A = \left(\frac{3kT}{2\langle r^2 \rangle_o} \right) \left[\left(\alpha_x^2 x^2 + \alpha_y^2 y^2 + \alpha_z^2 z^2 \right) - \left(x^2 + y^2 + z^2 \right) \right] \tag{1.7}$$

where A, k, T $\langle r^2 \rangle_0$, are the free energy, Boltzmann constant, absolute temperature in Kelvin and average end-to-end chain distance respectively. The deformation ratio of stressed to unstressed length, α, is defined as

$$\alpha_x = L_x / L_{xi} \quad ; \qquad \alpha_y = L_y / L_{yi} \qquad \alpha_z = L_z / L_{zi} \tag{1.8}$$

The assumption of an isotropic undeformed state requires that $\langle x^2 \rangle = \langle y^2 \rangle = \langle z^2 \rangle$. The dimension of the undeformed crosslinked chains is given by

$$\langle r^2 \rangle_i = \langle x^2 \rangle + \langle y^2 \rangle + \langle z^2 \rangle = 3\langle z^2 \rangle \tag{1.9}$$

Substituting the above simplifications in Eq. (1.7) for n chains, gives

$$\nabla A = \left(\frac{nkT}{2} \right) \left(\frac{\langle r^2 \rangle_i}{\langle r^2 \rangle_o} \right) \left[\alpha_x^2 + \alpha_y^2 + \alpha_z^2 - 3 \right] \tag{1.10}$$

For simplicity, the ratio $\langle r^2 \rangle_i / \langle r^2 \rangle_o$, is set equal to 1, assuming that the dimensions of the crosslinked chains is equal to that of the unperturbed end-to-end distance to give Eq. 1.11.

$$\nabla A = \left(\frac{nkT}{2} \right) \left[\alpha_x^2 + \alpha_y^2 + \alpha_z^2 - 3 \right] \tag{1.11}$$

Equations 1.10 and 1.11 are fundamental to theories of rubber elasticity and can be used to obtain the equations of state for rubber networks undergoing any type of deformation. For uniaxial elongation of rubber in the z direction at constant volume,

$$\alpha_x = \alpha_y; \qquad \alpha_x^2 \alpha_z = 1; \qquad \alpha_x = \alpha_z^{-1/2} \tag{1.12}$$

Substituting Eq. 1.12 into Eq. 1.11 gives

$$\nabla A = \left(\frac{nkT}{2} \right) \left[\alpha_z^2 + 2\alpha_z^{-1} - 3 \right] \tag{1.13}$$

Differentiating Eq. 1.13 gives the elastic force, *f,*

$$f_z = \left(\frac{\partial (\nabla A)}{\partial L_z} \right)_{V,T} = \left(\frac{\partial (\nabla A)}{\partial \alpha_z} \right)_{V,T} \left(\frac{\partial \alpha_z}{\partial L_z} \right)_{V,T} \tag{1.14}$$

Since $\alpha_z = L_z / L_{zi}$, $(\partial \alpha_z / \partial L_z) = 1 / L_{zi}$, and Eq. 1.14 becomes

$$f_z = \left(\frac{nkT}{L_{zi}} \right) \left[\alpha_z - \alpha_z^{-2} \right] \tag{1.15}$$

Therefore, the "engineering" stress is

$$\sigma_o = \frac{f_z}{L_{xi} L_{yi}} = \left(\frac{nkT}{L_{xi} L_{yi} L_{zi}} \right) \left[\alpha_z - \alpha_z^{-2} \right] = \left(\frac{nkT}{V} \right) \left[\alpha_z - \alpha_z^{-2} \right] \tag{1.16}$$

where $L_{xi}L_{zi}$ is the original cross sectional area and V is volume. The stress based on the true cross sectional area is,

$$\sigma = \frac{f_z}{L_x L_y} = \frac{f_z}{(\alpha_x L_{xi})(\alpha_y L_{yi})} = \frac{\sigma_o}{\alpha_x \alpha_y} = \left(\frac{nkT}{V}\right)\left[\alpha_z - \alpha_z^{-2}\right] \tag{1.17}$$

The ratio, *n/V*, in Eqs. 1.15 and 1.16 is network density of chains. The 'modulus', nkT/V, from Eqs. 1.16 and 1.17 linearly increases with an increase in temperature. This is characteristic of entropic elastic materials, and the opposite behavior is observed in thermoplastics. The stress for a given elongation, α, also has a linear dependence on temperature, with a stress of 0 Pa at 0 K. Any deviation from the origin is due to energetic contribution to the elastic force.

At higher elongations, the affine assumption begins to fail, and the 'phantom network' model is assumed. In this model, the crosslink positions are not fixed, but fluctuate about their average affine deformation positions.[39, 40] Swelling of the rubber network also tends to loosen the chain entanglements, allowing fluctuations in the crosslink positions. This modification lowers the modulus by a factor A_ϕ, which is less than 1,[39] and Eq. 1.16 becomes

$$\sigma_o = \frac{A_\phi f_z}{L_{xi}L_{yi}} = A_\phi\left(\frac{nkT}{L_{xi}L_{yi}L_{zi}}\right)\left[\alpha_z - \alpha_z^{-2}\right] = A_\phi\left(\frac{nkT}{V}\right)\left[\alpha_z - \alpha_z^{-2}\right] \tag{1.18}$$

A_ϕ is defined as

$$A_\phi = 1 - \left(\frac{2}{\phi}\right) \tag{1.19}$$

Where ϕ, the crosslink functionality is a measure of the number of chains emerging from a crosslink in the network.

For biaxial stretching in the x and y directions at constant volume, $\alpha_z = 1/(\alpha_x \alpha_y)$ and Eq. 1.11 becomes

$$\nabla A = \left(\frac{nkT}{2}\right)\left[\alpha_x^2 + \alpha_y^2 + \frac{1}{\alpha_x^2 \alpha_y^2} - 3\right] \tag{1.20}$$

Differentiating Eq. 1.15 gives

$$f_x = \left(\frac{\partial(\nabla A)}{\partial L_x}\right)_{V,T} = \left(\frac{\partial(\nabla A)}{\partial \alpha_x}\right)_{V,T}\left(\frac{\partial \alpha_x}{\partial L_x}\right)_{V,T} = \frac{nKT}{L_{xi}}\left[\alpha_x - \frac{1}{\alpha_x^3 \alpha_y^2}\right] \tag{1.21}$$

Therefore,

$$\sigma_x = \frac{f_x \alpha_x}{L_{yi} L_{zi}} = \left(\frac{nkT}{V}\right)\left[\alpha_x^2 - \frac{1}{\alpha_x^2 \alpha_y^2}\right] \tag{1.22}$$

Similarly,

$$\sigma_y = \left(\frac{nkT}{V}\right)\left[\alpha_y^2 - \frac{1}{\alpha_x^2 \alpha_y^2}\right] \tag{1.23}$$

If the stress in both x and y directions are equal, i.e., a "balanced" biaxial stress, $\alpha_x = \alpha_y = \alpha$, and $\sigma_x = \sigma_y$. Equations (1.22) and (1.23) become

$$\sigma_x = \sigma_y = \left(\frac{nkT}{V}\right)\left[\alpha^2 - \frac{1}{\alpha^4}\right] \tag{1.24}$$

"Balanced" biaxial stress in the x and y is tantamount to uniaxial compression in the z direction.

1.4.2 Fracture of Elastomers

Fracture can be defined as the mechanical rupture of a material under stress in to two or more pieces. In a typical fracture process, only few molecules (one in a million) that cross the fracture plane are broken successively as the fracture propagates across the specimen at a finite speed.[41] Fracture occurs because every solid body contains flaws and region of weakness, characterized by cuts, dirt particles or scratches, where the applied stress is greatly magnified and the flaw begins to grow as a crack.

Elastomers are viscoelastic and have the ability to store strain energy in the form of decreased chain conformational entropy and dissipate energy via local viscoelastic chain motion, chain alignment, chain rupture, strain-induced crystallization, hydrogen bonding and cavitation of hard fillers. Of course, the design of optimally strengthened elastomers involves increasing energy dissipation and prolonging chain rupture. During crack propagation, new surface area is created at the crack location, which increases the surface free energy of the system. Griffith suggested that a crack will propagate in a stressed material provided the crack propagation process reduces the elastically stored energy, W, to a value that will meet the surface free energy requirements γ of the newly formed fractured surfaces.[41] This requirement for crack propagation can be mathematically represented as

$$\left(\frac{\partial W}{\partial l}\right) \geq \frac{1}{2} G_c \frac{\partial A}{\partial L} \tag{1-25}$$

where l is the length or radius of the fracture surface, A is the surface area of the material, and G_c is the amount of energy needed to advance the fracture per unit area. The factor of $1/2$ is introduced to account for the two newly formed surfaces resulting from the

fracture of the material. An alternative criterion for fracture was proposed by Irwin. Irwin proposed that a critical value of the stress intensity factor, K_c is required in order for fracture to occur. The above criteria are equally valid, regardless of specimen geometry or loading condition. The stress intensity factor, K_c is defined

$$K_c = \left(\frac{\pi^{1/2}}{2} \right) \sigma_t r^{1/2} \tag{1-26}$$

or

$$K_c = \pi^{1/2} \sigma_b l^{1/2} \tag{1-27}$$

where, σ_t, r, σ_b and l are the stress at the tip of the flaw, radius of the unstressed flaw, applied breaking stress and length of the flaw respectively.

The mechanical response of elastomers is affected by temperature, strain rate, and the ability of the elastomer to crystallize under strain. Even though the crack initiation process appears to be similar in all elastomers, the propagation of cracks in amorphous elastomers is different from that in strain-crystallizing elastomers.[41-43] In amorphous elastomers, tear propagation depends on temperature, T, and the rate at which strain energy is converted in to fracture energy (G) as the tear advances. Fracture energy, G, is defined as

$$G = -\frac{2}{A} \left(\frac{\partial W}{\partial l} \right) \tag{1-28}$$

where, W is the total strain energy of the material, and A is the area of the crack, which increases as the crack advances. The dependence of the fracture energy on temperature of amorphous elastomers is due to changes in segmental mobility with temperature. When corrected for segmental mobility, the fracture energies of six unfilled amorphous

elastomers at different temperatures superpose to form a single master curve.[41] Hence the fracture energy, G, ought to be the same for all unfilled amorphous elastomers at the same segmental mobility. However, the fracture energy increases with tearing rate in a manner similar to the dependence of energy dissipation on deformation rate in viscous materials. This implies that high tear strengths correspond to large energy dissipations.

Tear strength of strain-crystallizing elastomers increases during straining, provided straining is performed at a rate and temperature that promotes crystallization.[41, 43] At high temperatures and strain rates, crystallization does not occur, and the molecules do not have enough time to align into crystallites. The high strength observed in strain-crystallizing elastomers is related primarily to increased energy dissipation on stretching, alignment of chains, the potential for hydrogen bond formation between the chains in the material.

An empirical equation given by Grosch[44],

$$W_b = 410 W_d^{2/3} \tag{1-29}$$

shows a direct relationship between the energy W_b per unit volume required to break elastomers, and the energy dissipated, W_d, by stretching the elastomer almost to the point of breaking. The relationship is true for all elastomers, and indicates that stronger elastomers dissipate most of their energy before they break.

1.5 POLYLER/SILICATE NANOCOMPOSITES

The idea of adding silicates to polymers in order to make polymer/silicate nanocomposites have received a lot of attention over the past decade because of the enhancement in the polymer properties (mechanical, thermal, barrier, etc.). This novel idea was first introduced by Toyota researchers using Nylon 6. Specifically, the mechanical and thermal properties of Nylon 6 were significantly enhanced by dispersing nanometer sized clay particles in the polymer matrix.[45-48] Since this revelation, many polymer/silicate nanocomposite systems have been investigated and all of these systems have shown improvement in the properties of the polymer. [49, 50] Homogenous dispersion of the silicate is required for enhancement in polymer properties.

Achieving homogenous dispersions is very difficult because the silicates are hydrophilic, and possess high surface energies relative to the hydrophobic polymer. Ion exchange reactions between the silicate cations (typically Na^+ and Ca^{2+}) and organic cations reduces the silicate surface energy, making the silicates organophilic (compatible with the polymer). Several synthesis routes, including, melt intercalation and in-situ polymerization are available for making polymer/silicate nanocomposites. Melt intercalation involves the mixing of the silicate with a molten polymer and in-situ polymerization involves monomer intercalation, followed by polymerization.

Depending on the nature of the components used (layered silicate, organic cation and polymer matrix) and the method of preparation, three main types of composites structures may be obtained as shown in Figure 1.8. Exfoliated structures are usually

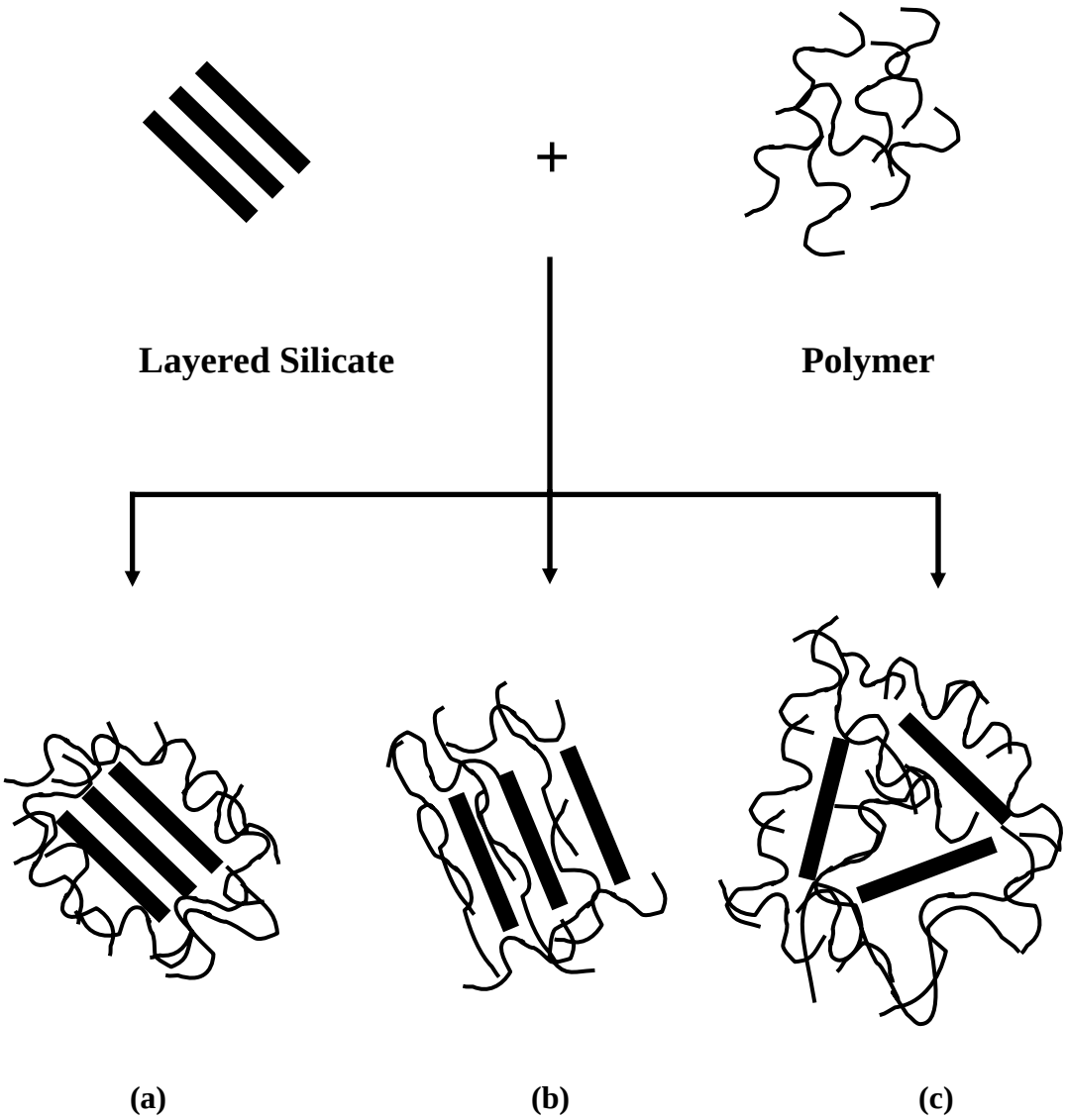

Figure 1.8: Schematic representation of different composite structures resulting from polymer silicate nanocomposite synthesis; (a) phase-separated microcomposite, (b) intercalated nanocomposite, and (c) exfoliated nanocomposite.

preferred because they produce materials with significant improvement in polymer properties relative to phase-separated microcomposite and intercalated structures.

1.6 OUTLINE

In chapters 2 and 3, the design and construction of a high-throughput apparatus (*HTMECH)* for characterizing the mechanical properties of polymers is described in detail. Validation measurements on a wide range of polymers are performed to demonstrate the instrument's reproducibility and sensitivity to chemical and structural changes. Measurements are also performed to determine the effect of strain rate on the mechanical properties of polymers. The effect of process parameters such as thickness, cure temperature and chain extender composition on mechanical properties of segmented polyurethaneureas is also investigated. The deformation mechanics with this instrument is also described based on well-developed plate and membrane theories. The instrument is compared and contrasted with conventional implementations of the dart impact and shaft-loaded blister techniques.

In chapters 4 and 5, previously developed combinatorial libraries synthesis techniques are extended to reactive polymer systems. Segmented polyurethaneurea libraries are prepared with continuous linear gradients in chain extender composition and cure temperature. Libraries are mechanically characterized with the *HTMECH* described in chapters 2 and 3 to determine optimum conditions of composition and temperature. Mechanical measurements from the HTMECH are combined with structural information from other measurement techniques to develop structure-mechanical property

relationships. Finally, measurements from the *HTMECH* are compared with measurements from a commercial instrument.

The optimized conditions of cure temperature and chain extender composition from chapters 4 and 5 are used to prepare novel segmented polyurethaneurea nanocomposites in chapter 6. The nanocomposites are prepared with reactive Laponite® particles that have free amines attached to the surface of the particle. Uniaxial tensile strength is optimized by varying the reactive particle concentration. The effect of particle type is investigated by comparing nanocomposites made with reactive Montmorillonite. Also, the effect of polymer-particle interactions is studied by comparing nanocomposites prepared with reactive versus non-reactive Laponite® particle. The mechanism of reinforcement is presented based on the effect of particle size and polymer-particle interactions on mechanical properties.

1.7 REFERENCES

(1) Ni, P., Li, J., Suo, J., Li, S, Novel Polyether Polyurethane/Clay Nanocomposites Synthesized with Organic-Modified Montmorillonite as Chain Extenders. *J. App. Polym. Sci.* **2004,** 94, 534.

(2) Tien, Y.-I., Wei, K.H., High-Tensile-Property Layered Silicates/Polyurethane Nanocomposites by Using Reactive Silicate as Psuedo Chain Extenders. *Macromolecules* **2001,** 34, 9045.

(3) Petrovic, Z. S.; Ferguson, J., Polyurethane Elastomers. *Prog. Polym. Sci.,* **1991,** 16, 695.

(4) Wang, C. B.; Cooper, S. L., Morphology and Properties of Segmented Polyether Polyurethaneureas. *Macromolecules* **1983,** 16, 775.

(5) Ikkai, F.; Shibayama, M.; kashihara, H.; Nomura, S., SAXS and Dynamic Viscoelastic Studies on Segmented Polyurethaneurea Solutions. *Polymer* **1997,** 38, (4), 769.

(6) Lee, H. S.; Wang, Y. K.; Macknight, W. J.; Hsu, S. L., Spectroscopic Analysis of Phase-Separation Kinetics in Model Polyurethanes. *Macromolecules* **1988,** 21, 270.

(7) Paik Sung, C. S.; Smith, T. W., Properties of Segmented Polyether Poly(urethaneureas) Based on 2,4-Toluene Diisocyanate. 2. Infrared and Mechanical Studies. *Macromolecules* **1980,** 13, 117.

(8) Wu, L.; Li, D.; You, B.; Qian, F., Change in Mechanical Properties, Composition, and Structure of Hydrated Polyurethaneurea. *J. App. Polym. Sci.,* **2001,** 80, 252.

(9) Wu, L.; You, B.; Li, D.; Qian, F., Effect of Hydration on the Mechanical Properties, Composition and Molecular Weight of Polyurethaneureas. *Polym. Int.* **2000,** 49, 1609.

(10) Meredith, J. C.; Karim, A.; Amis, E. J., High-Throughput Measurement of Polymer Blend Phase Behavior. *Macromolecules* **2000,** 33, (16), 5760.

(11) Meredith, J. C.; Smith, A. P.; Karim, A.; Amis, E. J., Combinatorial Materials Science for Polymer Thin-Film Dewetting. *Macromolecules* **2000,** 33, (26), 9747.

(12) Gum, W. F., Wolfram, R., Ulrich, H., *Reaction Polymers: Polyurethanes, Epoxides, Unsaturated polyesters, Phenolics, Special Monomers, and Additives; Chemistry, Technology, Applications, Markets*. Hanser: **1992**.

(13) Oertel, G., *Polyurethane Handbook*. 2 ed.; Hasner Gardner Publications, Inc.: Cincinnati, **1993**.

(14) Ma, J.; Zhang, S.; Qi, Z., Synthesis and Characterization of Elastomeric Polyurethane/Clay Nanocomposites. *J. App. Polym. Sci.,* **2001,** 82, 1444.

(15) Garrett, J. T., Runt, J., Microphase Separation of Segmented Poly(urethane urea) Block Copolymers. *Macromolecules* **2000,** 33, 6353.

(16) Garrett, J. T.; Siedlecki, C. A.; Runt, J., Microdomain Morphology of Poly(urethane urea) Multiblock Copolymers. *Macromolecules* **2001,** 34, 7066.

(17) Ishihara, H., Kimura, I., Saito, K., Ono, H., Infrared Studies on Segmented Polyurethane-Urea Elastomers. *J. Macromol. Sci.-Phys.,* **1974,** B10(4), 591.

(18) Petrovic, Z. S.; Ilavsky, M.; Dusek, K.; Vidakovic, M.; Javni, I.; Banjanin, B., The Effect of Crosslinking on Properties of Polyurethane Elastomers. *J. App. Polym. Sci.,* **1991,** 42, 391.

(19) Chiou, B.-S.; Schoen, P. E., Effects of Crosslinking of Thermal and Mechanical Properties of Polyurethanes. *J. App. Polym. Sci.,* **2002,** 83, 212.

(20) Huang, J.; Zhang, L., Effects of NCO/OH Molar Ration on Structure and Properties of Graft-Interpenetrating Polymer Networks from Polyurethane and Nitrolignin. *Polymer* **2002,** 43, 2287.

(21) Petrovic, Z. S.; Javni, I.; Banhegyi, G., Mechanical and Dielectric Properties of Segmented Polyurethane Elastomer Containing Chemical Crosslinks in the Hard Segments. *J. Polym. Sci., Part B: Polym. Phys.* **1998,** 36, 237.

(22) Petrovic, Z. S.; Javni, I.; Divjakovic, V., Structure and Physical Properties of Segmented Polyurethane Elastomers Containing Chemical Crosslinks in the Hard Segments. *J. Polym. Sci., Part B: Polym. Phys.* **1998,** 36, 221.

(23) Paik Sung, C. S.; Schneider, N. S., Temperature Dependence of Hydrogen Bonding in Toluene Diisocyanate Based Polyurethanes. *Macromolecules* **1976,** 10, (2), 452.

(24) Senich, G. A.; Macknight, W. J., Fourier Transform Infrared Thermal Analysis of a Segmented Polyurethane. *Macromolecules* **1980,** 13, 106.

(25) Coleman, M. M.; Lee, K. H.; J., S. D.; Painter Paul, C., Hydrogen Bonding in Polymers. 4. Infrared Temperature Studies of a Simple Polyurethane. *Macromolecules* **1986,** 19, 2149.

(26) Grandy, D. B.; Hourston, D. J.; Price, D. M.; Reading, M.; Silva, G. G.; Song, M.; Sykes, P., Microthermal Characterization of Segmented Polyurethane Elastomers and a Polystyrene-Poly(methyl methacrylate) Polymer Blend Using Variable Temperature Pulsed Force Mode Atomic Force Microscopy. *Macromolecules* **2000,** 33, 9348.

(27) Lee, H. S.; Wang, Y. K.; Hsu, S. L., Spectroscopic Analysis of Phase Separation Behavior of Model Polyurethane. *Macromolecules* **1987,** 20, 2089.

(28) McLean, R. S.; Sauer, B. B., Tapping-Mode AFM Studies Using Phase Detection for Resolution of Nanophase in Segmented Polyurethanes and Other Block Copolymers. *Macromolecules* **1997,** 30, 8314.

(29) Miller, J. A.; Lin, S. B.; Hwang, K. K. S.; Wu, K. S.; Gibson, P. E.; Cooper, S. L., Properties of Polyether-Polyurethane Block copolymers: Effects of Hard Segment Length Distribution. *Macromolecules* **1985,** 18, 32.

(30) Musselman, S. G.; Santosusso, T. M.; Barnes, J. D.; Sperling, L. H., Domain Structures and Interphase Dimensions in Poly(urethaneurea) Elastomers Using DSC and SAXS. *J. Polym. Sci., Part B: Polym. Phys.* **1999,** 37, 2586.

(31) Ning, L., De-Wing, W., Sheng-Kang, Y., Cryatallinity and Hydrogen Bonding of Hard Segments in Segmented Poly(urethaneurea) Copolymers. *Polymer* **1996,** 37, (16), 3577.

(32) Osaki, K.; Kimura, S.; Nishizawa, K.; Kurata, M., SAXS Studies of Segmented Polyether Poly(urethaneurea) Elastomers. *Macromolecules* **1980,** 14, 456.

(33) Paik Sung, C. S.; Schneider, N. S., Infrared Studies of Hydrogen Bonding in Toluene Diisocyanate Based Polyurethanes. *Macromolecules* **1974,** 8, (1), 68.

(34) Seymour, R. W.; Estes, G. M.; Cooper, S. L., Infrared Studies of Segmented Polyurethane Elastomers. I. Hydrogen Bonding. *Macromolecules* **1970,** 3, (5), 579.

(35) Xiu, Y. Y.; Zhang, Z. P.; Wang, D. N.; Ying, S. K.; Li, J., Hydrogen Bonding and Crystallization Behaviour of Segmented Polyurethaneurea: Effects of Hard Segment Concentration. *Polymer* **1992,** 36, (6), 1335.

(36) Bonart, R.; Morbitzer, L.; Muller, E. H., X-ray Investigations Concerning the Physical Structure of Crosslinking in Urethane Elastomers. III. Common Structure Principles for Extension with Aliphatic Diamines and Diols. *J. Macromol. Sci.-Phys.,* **1974,** B9, (3), 447.

(37) Paik Sung, C. S.; Hu, C. B.; Wu, C. S., Properties of Segmented Poly(urethaneureas) Based on 2,4-Toluene Diisocyanate. **1**. Thermal Transitions, X-ray Studies, and Comparison with Segmented Poly(Urethanes). *Macromolecules* **1980,** 13, 111.

(38) Meredith, J. C.; Amis, E. J., LCST Phase Separation in Biodegradable Polymer Blends: Poly(D,L-Lactide) and Poly(ε-Caprolactone). *Macromol. Chem. Phys.* **2000,** 201, 733.

(39) Mark, J. E., Eisenberg, E., Graessley, W.W., Mandelkern, L., Koenig, J.L., The Rubber Elastic State. In *Physical Properties of Polymers*, American Chemical Society: Washington, **1984**; pp 1.

(40) Gedde, U. W., In *Polymer Physics*, Chapman & Hall: London, **1996**; pp 39-53.

(41) Eirich, F. R., *Science and Technology of Rubber*. Academic Press: New York, **1978**; p 419.

(42) Andrews, E. H., Crack Propagation in Strain-Crystallizing Elastomer. *J. Appl. Physics* **1961,** 32, (3), 542.

(43) Eirich, F. R., Failure Modes of Elastomers. *Engineering Fracture Mechanics* **1973,** 5, 555.

(44) Grosch, K. A., Harwood, J.A.C., Payne, A.R., Breaking Energy of Rubber. *Nature (London)* **1966,** 212, 497.

(45) Kojima, Y., Usuki, A., Kawasumi, M., Okada, A., Fukushima, Y., Mechanical Properties of Nylon 6-Clay Hybrid. *J. Mater. Res.* **1993,** 8, (5), 1185.

(46) Kojima, Y., Usuki, A., Kawasumi, M., Okada, A., Kurauchi, T., Kamigaito, O., Synthesis of Nylon 6-Clay Hybrid by Montmorillonite Intercalated with ε-Caprolactam. *J. Polym. Sci., Part A: Polym. Chem* **1993,** 31, 983.

(47) Usuki, A., Kojima, Y., Kawasumi, M., Okada, A., Fukushima, Y., Synthesis of Nylon 6-Clay Hybrid. *J. Mater. Res.* **1993,** 8, (5), 1179.

(48) Usuki, A., Kawasumi, M., Kojima, Y., Okada, A., Kurauchi, T., Swelling Behavior of Montmorillonite Cation Exchanged for ω-Amino Acids by ε-Caprolactam. *J. Mater. Res.* **1993,** 8, (5), 1174.

(49) Alexandre M. and Dubois, P., Polymer-Layered Silicate. *Mater. Sci. and Eng.* **2000,** 28, 1.

(50) LeBaron, P. C., Wang, Z., Pinnavaia, T.J., Polymer-Layered Silicate Nanocomposites: An Overview. *Applied Clay Science* **1999,** 15, 11.

CHAPTER 2

HIGH-THROUGHPUT MECHANICAL CHARACTERIZATION OF FREE-STANDING POLYMER FILMS

In this chapter, we review the design, construction, and operation of an instrument for high-throughput mechanical characterization (*HTMECH*) of polymer films. In particular, the *HTMECH* is applied here to free-standing polymer libraries with gradients in properties such as temperature and composition. Here, the goal is discovery of mechanical property relationships with polymer formulation and processing. However, *HTMECH* can also measure strain-rate libraries for uniform samples from near-static to meters-per-second (impact velocities). *HTMECH* measures force and deformation of film regions that undergo transverse biaxial loading by an instrumented thin contact tip. We demonstrate the salient features of mechanical models of the *HTMECH* assay and how they are employed to extract meaningful parameters from the raw data. The *HTMECH* instrument is compared and contrasted with conventional implementations of the dart impact and blister techniques.

2.1 INTRODUCTION

2.1.1 Motivation

The successful application of combinatorial and high-throughput methods (CHM) in the pharmaceutical and catalyst industry has made these techniques very attractive to materials researchers.[1] Compared to conventional 1-sample-1-measurement techniques, CHM provide a cost and time-saving alternative, especially during the discovery stages of a materials research endeavor. In addition, CHM are very useful for development and optimization of materials and processing parameters. The purpose of CHM is not to replace established measurement techniques, but rather to provide an efficient screening over large ranges of parameters. This is accomplished through a cycle that involves (1) experimental design, (2) preparation of libraries, (3) high-throughput measurement of desired properties, (4) analysis, and (5) optimization to select the next experimental design. CHM reduce the likelihood of overlooking unexpected behavior. It is recognized in this chapter that full-scale material development and scientific characterization require detailed investigation of carefully controlled systems, following the implementation of CHM.

In order to apply CHM to materials research, numerous methods have been developed for preparing libraries with either continuous gradients or discrete variations in composition (mixtures, reactions), thickness, and temperature (*T*, curing, annealing)).[2-6,7-18] With numerous library preparation techniques available, the important limitations in materials CHM appear to be in the screening and analysis stages. Particularly, there is a strong need to extend the suite of high-throughput measurements available. Measurements have been demonstrated in many cases using non-contact methods like

microscopy and spectroscopy. However, many materials design and research efforts require knowledge of mechanical responses. The necessity of physically contacting the surface of the library makes mechanical screening more challenging than the non-contact measurements.

Polymer mechanical properties are especially sensitive to processing variables such as temperature and rheological history, which strongly affect the nano- and microstructure. To address the need for high-throughput measurements capable of determining such processing-structure-mechanical property relationships, we reported previously a new apparatus for high-throughput mechanical characterization (*HTMECH*) of polymer libraries.[19] We have applied *HTMECH* to characterize structure-property relationships in polyurethaneurea *T*-gradient[20] and composition-gradient[21] libraries. Recently, others have introduced alternative methods of high-throughput screening of polymers, such as a strain-buckling technique for supported films,[22] parallel arrays of dynamic-mechanical measurements[7], and a rapid-serial high-throughput mechanical device.[22] The purpose of this review is to describe in detail the design and operational features of the *HTMECH* instrument.

Conventional (non-combinatorial) practice involves placing one-sample into a grip or mounting to perform each mechanical measurement. In contrast, parallel library samples suggest the need for miniaturized instrumentation that allows independent deformation and detection of mechanical response at each relevant library region. This may be performed in parallel or rapid-serial fashion, but the requirements for miniaturization, rapid measurements, and independence between measurement sites clearly go beyond commercial instrumentation or standardized assays.

Equally as important as screening speed is the integration of measurement with analysis methods. As the mechanical measurement technology presented here is novel, there is a need to develop custom analysis software that accounts for instrument-specific noise, potential errors, and signal responses.

2.1.2 Brief Review of Related Measurement Techniques

Mechanical assays have been developed for a wide range of materials classes, sample geometries, deformation modes, and strain rates. These have been motivated primarily by mechanical situations encountered in applications, e.g., tensile, compression, or peeling. As deformation and fracture mechanics theory has advanced, certain assays have been developed specifically for limiting geometries that are amenable to analysis, e.g., plane-strain and plane-stress. Some assays are geared to probe specific structure-property relationships, e.g., effect of crystallization on modulus.

The measurements commonly employed for mechanical characterization can be broken into three broad categories: (1) deformation, (2) fracture, and (3) cyclical. The deformation techniques are usually performed at a constant strain rate and include uniaxial and biaxial tension and three-point bending assays. These lead to the ability to calculate useful parameters, such as Young's modulus and yield strength. Under extreme strain, deformation leads to fracture and detection of tensile strength and % elongation at break. Fracture-specific assays are designed to measure parameters indicative of the ultimate strength of materials. Common methods employed for polymers include Izod and Charpy impact, peel tests, and falling-dart impact tests. Generally these methods lead to some measure of energy absorbed prior to failure. When performed as a function of temperature, composition (or other environmental variables), ductile-to-brittle

transitions can be observed. Like the deformation-focused assays, fracture assays like those mentioned previously are usually performed at a single value of strain rate. Finally, cyclical strain assays have been developed to ascertain the time- and strain-rate dependence of mechanical properties. Perhaps foremost among these for polymers is the dynamic mechanical analysis technique, in which a sample is repeatedly deformed and relaxed over a range of frequencies. Most of these assays have been standardized by The American Society for Testing and Materials (ASTM International)[23,24] and the International Organization for Standardization (ISO).[25] These organizations foster the voluntary development and publication of market-relevant materials standards and tests. These techniques have largely been developed for sampling one-at-a-time with relatively large samples (tens of centimeters), and are generally not compatible with the needs and goals of miniaturized high-throughput screening.

Polymer properties are commonly measured under tension or compression. We focus here on instrumentation for high-throughput mechanical screening via tensile deformation. Sample "regions" on common polymer library platforms are usually on the range of a few millimeters in diameter, and miniaturization of the loading geometry is essential. Since the combinatorial library samples are all contained on a single contiguous plate or continuous-gradient, it is difficult to imagine a convenient method for "gripping" each sample region at its edges, as is done for example in the common uniaxial tension test. In addition, the removal of a sample region by cutting it free from the library, in order to place it into a mechanical instrument, would be tedious and difficult to automate.

For these reasons, assays that involve the direct application of a load-measuring probe onto free-standing regions of a library appear more promising. The so-called "falling-dart" impact tests, [26-30] Fig. 2.1a, covered via ASTM and ISO standards,[31-36] are a good example. Originally, the assay involved rigid mounting of a thin sample or film in a circular clamp. A graduated series of progressively-heavier impact darts were dropped onto the center of the specimen until failure occurred. More recently, the method has been instrumented using a load sensor in the dart or in the mounting.[34, 36]

This class of assays is not limited to impact-mode with falling darts. The so-called *indentation* and *bulge* tests also involve the transverse, static loading of substrate-supported and free-standing films, respectively. Indentation methods typically use spherical probes or instrumented shafts to load the film centrally, Fig. 2.1b.[37-44] Bulge tests load the film uniformly on one side with hydrostatic pressure, Fig. 2.1c.[38, 45, 46] The ASTM and ISO specifications,[31-36] and thus commercial instruments, for falling-dart, indentation, and bulge tests utilize large samples (tens of cm) and contactors (several cm). Although these implementations were not originally intended for high-throughput investigation, they are easily adapted to that purpose, as we show in this review. For simplicity we have omitted discussion of the important field of micrometer and nanometer-scale indentation tests of substrate-supported films.[47-49] The focus here is on characterization of free-standing films, as indentation of substrate-supported films induces a complex stress state that is dominated by compression and shear, rather than tension.

Free standing film indentation experiments have inspired development of theoretical approaches for modeling data and extracting mechanical parameters.

(a) Falling-Dart Impact

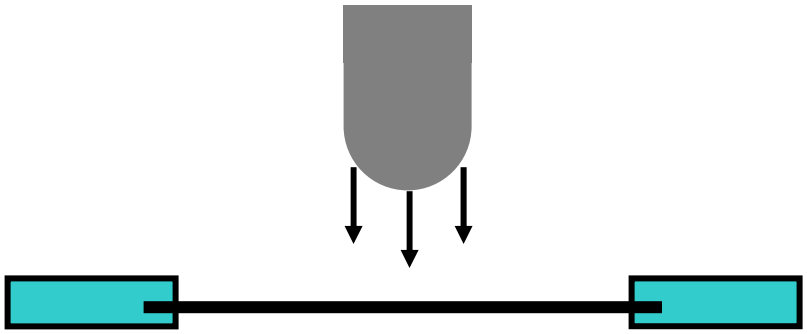

(b) Static Spherical Indenter (Blister Test)

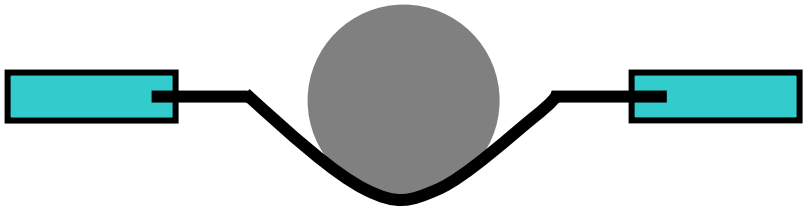

(c) Uniform Hydrostatic Pressure Bulge Test

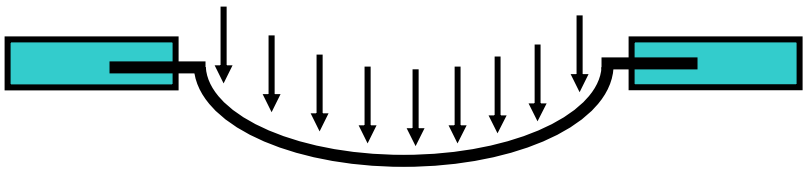

Figure 2.1: Schematics of various falling dart and indenter-type geometries and deformations.

Consider Fig. 2.2, which describes the general stresses encountered during indentation of a film rigidly clamped at its edges in a circular mount. The transverse loading of a film normal to its surface results in a biaxial deformation, which is more complex than the uniaxial deformation commonly employed for polymer characterization. In a biaxial film deformation, stresses can be tensile, bending, and shear, as in Fig. 2.2. There are two tensile components, radial (σ_R) and tangential (σ_T), and one bending component, σ_B. In addition, at significant elongations, contact between the tip and film can lead to a shear stress, σ_S. It must be recognized that in general each of these stresses is a function of radial (r) and angular position on the film, although symmetry usually eliminates the angular dependence. Because solution of the general problem involving all four stresses is non-trivial and only possible numerically, models of stress-deformation relationships generally fall into two classes: *membrane mechanics* and *plate mechanics*. Membranes are idealized, purely elastic materials that undergo pure tension as the indenter deforms the film ($\sigma_B = 0$). Plate theory treats the opposite extreme of stiff, rigid materials that undergo pure bending ($\sigma_R = \sigma_T = 0$). Models that incorporate significant shear effects must necessarily involve viscoelastic terms, and are often only solvable numerically. In addition, the incorporation of plasticity, fracture, and strain-induced orientations is usually accomplished only with numerical, e.g., finite element, approaches. [50-52] In interpreting data and in designing the instrument, it is important to identify the geometrical factors that can be adjusted to isolate the bending, tensile, and shear components. A number of papers have explored analytical and numerical solutions to the stress-strain relationships governing membrane mechanics,[37, 38, 43, 44, 50, 53, 54] and the

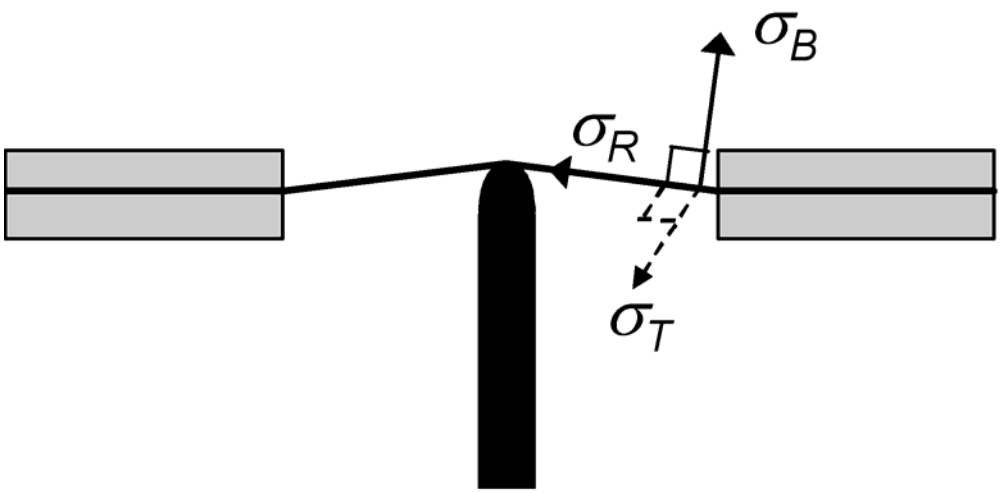

Figure 2.2: Generalized cross-sectional diagram of the "sandwiched" film and the three principle stresses possible as a function of applied strain.

transition between membrane and plate behavior.[54] One important result is that the ratio of the indenter radius to the hole radius has been identified as the key parameter that controls the isolation of tensile versus bending effects, as well as the onset of plasticity and yielding behavior.

The high-throughput mechanical characterization (*HTMECH*) instrument described herein follows the shaft-loaded indentation and falling-dart tests as a guiding model. *HTMECH* was designed specifically for rapid-serial testing of discrete or gradient combinatorial material libraries in which each sample spot is no more than a few millimeters in diameter. The goal is to collect load vs. deformation profiles from ~100 sample regions on a library within 1 hour. The significant differences as compared to conventional instruments and standards are (1) the miniaturization of the loading shaft to dimensions below 1 mm, (2) the rigid clamping of the entire library with a two-plate multi-hole sample holder that isolates neighboring measurement sites, (3) a reversal of the relative motions so that the sample approaches a fixed probe, and (4) the automation of the sample positioning and deformation apparatus.

2.2 DESIGN CONSIDERATIONS FROM THEORY AND MODELING

Green and Adkins[53] presented the general theory of large deformations of elastic membranes: thin materials that do not exhibit bending stresses σ_B (normal to plane of material) while loading. Thin elastomeric polymers are thought to come close to the ideal membrane model, where all of the stress is distributed in the plane of the material, with both radial and tangential components, $\sigma_R(r)$ and $\sigma_T(r)$. The deformation of axisymmetric membranes is treated by Yang and Feng,[44] who presented a numerical

solution of the geometry employed in this work, namely a circular membrane deformed by a spherical tip.[43] The governing partial differential equations describe the *equilibrium* stress distribution and profile of the deformed film, at a given indentation distance. It is important to emphasize that experimental conditions only approximate equilibrium in the case of slow strain rates, whereas large strain rates are likely to be far from equilibrium. Nevertheless, an examination of membrane theory sheds important physical insights onto the *HTMECH* apparatus design and interpretation of results.

To understand the measurement geometry employed in this work, it is desirable to know how the film profile, $w(r)$ (m), radial stress, $\sigma_R(r)$ (N/m^2), and tangential stress, $\sigma_T(r)$, depend upon the load force, F (N), film radial position, r (m), sample geometry, and material properties, e.g., elastic modulus, E. In the absence of significant flexural rigidity, Eq. 2.1 and 2.2 describe the relationship between these parameters and must generally be solved numerically or through infinite series.

$$\left(\frac{1}{r}\frac{df}{dr}\right)\frac{dw}{dr} = \frac{rP}{2} \tag{2.1}$$

$$\frac{d}{dr}(\nabla^2 f) + \frac{Eh}{2r}\left(\frac{dw}{dr}\right)^2 = 0 \tag{2.2}$$

In the expressions above, $f(r)$ is the stress function (units of Nm), P (N/m^2) is the load pressure ($F/\pi c^2$, where c is the probe-film contact radius), and h is the film thickness. Wan and Liao[42] presented an analytical solution in two limiting cases that are particularly relevant to the geometry employed here. The film profile is divided into a contact region

(where tip contacts film) and a noncontact region (extending from contact radius, $r = c$, to the mounting edge, $r = r_0$) (see Fig. 2.7). In the contact region, the solution is simplified because the film profile, $w_c(r)$ is constrained to follow the tip shape. To obtain an analytical solution in the non-contact region, the authors adopted two different assumptions about the film profile and stress distribution. In the conical approximation, it was assumed that the film profile, $w(r)$, is a simple linear function (linear profile in Fig. 2.7). In the uniform stress assumption, the stress is assumed to be distributed uniformly throughout the non-contact region, e.g., $f \neq f(r)$. It turns out that these two solutions offer approximate maximum and minimum bounds on what is observed experimentally. In addition, their solutions indicate the predicted dependence of load versus deflection, d, as a function of the ratio of the tip radius (R) to the hole radius (r_0), $\rho = R/r_0$. Of particular interest is that both approximations predict that as $\rho \rightarrow 0$ (the point-load limit) the load, $F \sim d^n = d^3$, which is a common characteristic of thin films.[42] As $\rho \rightarrow 1$, the gradient of F with respect to d, n, becomes larger than 3. As ρ increases, the rate of stress build-up in the sample decreases, and hence the resulting % elongations at break increase. Also, as ρ decreases, models predict that the level of stress concentration at the contact tip increases considerably.[50-52, 54] The stress concentration leads to higher loads being recorded and failure at an earlier % elongation. In fact, our own numerical calculations using ANSYS™, a commercial finite element software package, show a dramatic non-uniform stress distribution for $\rho = 0.05$, as compared to much more homogeneous stress distribution (with respect to radial position, r) for $\rho = 0.17$ and $\rho = 0.47$.

The models above assume purely elastic materials with no bending. In reality one wishes to understand how the onset of plastic deformation or presence of bending might

affect the load-deflection data. The experiments of Wan and Liao[42] indicate that when plastic yielding does occur, it begins at the contact point between tip and film, $r = c$, alluding to a stress that depends on r, with a maximum at $r = c$. The conical profile assumption (non-constant stress function) predicts that to keep the sample from yielding, $R \geq 9F/(2\pi h\sigma_y)$, where σ_y is the yield stress. Thus, for a constant yield strength, the onset of plastic deformation will be enhanced by smaller tip radius, larger loads, and thinner films. In addition, their experiments discuss the influence of tip radius on the stretching versus bending behavior of real films that have a nonzero bending component. For films that have significant flexural rigidity, or large thicknesses, the gradient of F versus d drops below $n = 3$, with $n = 1$ at pure bending. There is a corresponding maximum tip radius, R, for the film to undergo pure stretching. The minimum and maximum radii to avoid plasticity and bending, respectively, offer an important design criterion for the geometry of the indenter and mounting hole.

2.3 INSTRUMENT DESIGN

Figure 2.3 shows a schematic and Figure 2.4 presents a photographic image of the *HTMECH* apparatus for high-throughput screening of mechanical properties in 10 to 1000 μm thick polymer library films. The design of the apparatus allows measurement of force vs. deformation of up to 100 different points on a combinatorial library over a range of strain rates ($\dot{\gamma}$) from near-static (0.05 mm/s) to dynamic-impact (1000 mm/sec), within a short amount of time. Typically, the rate of measurement is less than 20 s per hole,

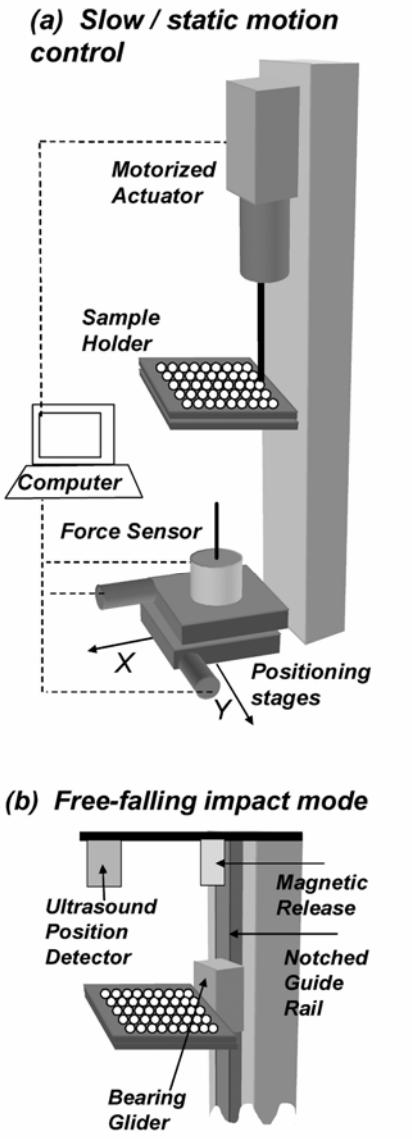

Figure 2.3: Schematics of the *HTMECH* apparatus (a) Static and slow mode, (b) free-falling impact mode.

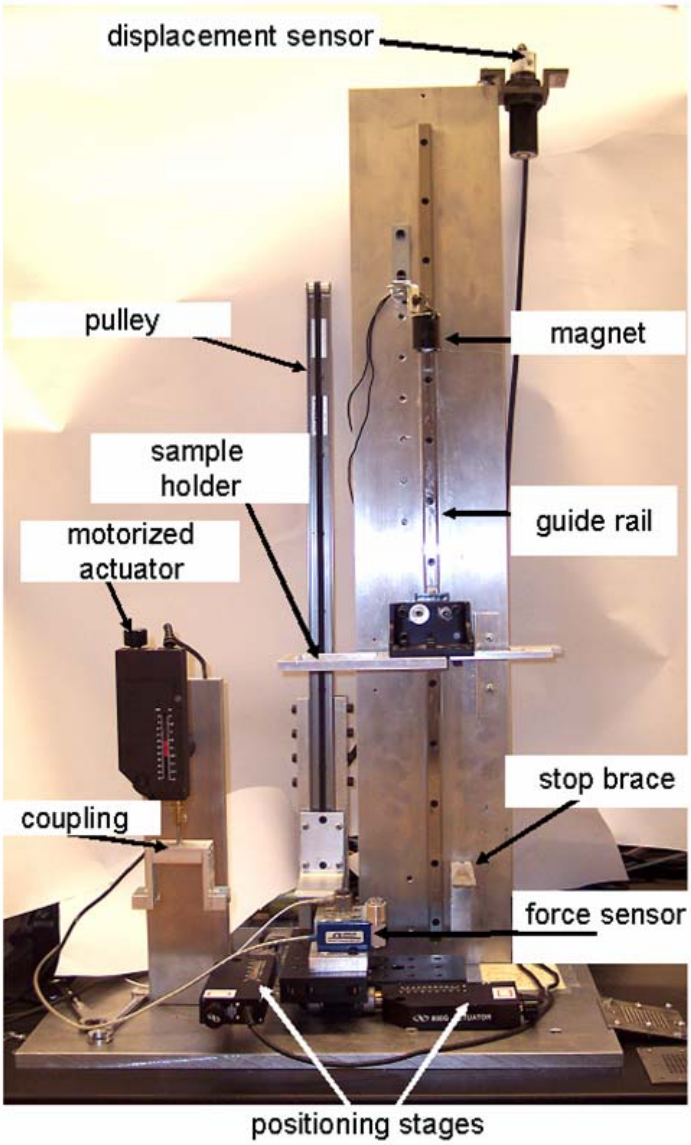

Figure 2.4: Digital image of the *HTMECH* apparatus.

requiring about 30 min to complete a 100-hole grid at γ= 1000 mm/s (impact mode). Most of this time is due to the movement of the positioning stages, which can be reduced dramatically by installing actuators capable of faster motion. The Newport actuators used here are capable of 2 mm/s maximum.

2.3.1 Sample Holder

The characterization of a polymer film with *HTMECH* starts with mounting the sample (polymer film) between two isolation-grid sample plates, detail shown in Fig 2.5. The sample plates are a pair of 3 inch-squared, 1/8 inch thick carbon-steel plates, perforated with 10 x 10 grid of holes. Carbon steel was used as this material was found to be easily machineable to a very flat surface, to allow uniform pressure between the plates and around each measurement hole. The holes have a diameter of 3 mm and the spacing between neighboring holes is 1 mm. Sample plates with different hole diameters were also fabricated to investigate variation of the ratio of the needle hole-to-sample hole radii. The sample plates are needed in order to (1) provide uniform pressure over the entire film during testing and (2) isolate the individual measurement sites, thereby preventing measurement at one site from interfering with measurements at neighboring sites. Several #6 through holes are drilled at the edges of the grid to allow mounting of the isolation grids in the sample holder, as shown in Figure 2.5a. The sample holder is a 4 in^2, half inch thick aluminum block with a square hole cut through the aluminum block to permit access to the grid holes by the indenter needle. The sample plates are then screwed into threaded holes on the sample holder using #6 machine screws.

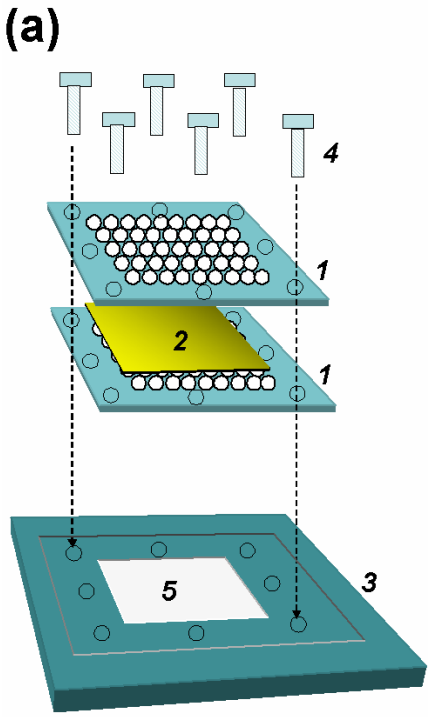

Figure 2.5: Schematics (a) and image (b) of the sample isolation grid and sample holder.

2.3.2 Instrumentation

Dynamic impact. Dynamic measurements were performed using a piezoelectric force sensor (Omega Engineering DLC101-10), which has a 10 lb load capacity. The DLC101-10 is a dynamic load cell with a frequency range (bandwidth) of 25 kHz, ideal for high-frequency force measurements. The sensor contains a thin piezoelectric crystal which generates an analog voltage signal when a dynamic force is applied. Due to the short discharge time constant of piezoelectric crystals, dynamic calibration of the load cell was performed prior to taking measurements,[29] as described in an earlier publication.[19] The calibration constant we obtained was within ± 2% of the valued provided by the manufacturer.

The dynamic setup, Fig. 2.3b and Fig. 2.4, involves a custom-made belt-driven pulley system, constructed from a simple DC motor, notched belt and gears (McMaster-Carr), and solid-state relays (Omega Engineering), used to raise and lower the sample holder for each impact measurement. A bearing glider (McMaster-Carr) attached to the sample holder, slides on a notched glide rail (McMaster-Carr) to allow a smooth and controlled motion of the sample as it falls. An electromagnet (McMaster-Carr) is used to hold the sample holder to initiate each impact measurement. An ultrasonic displacement sensor (Migatron RPS-401A-40) records the position of the sample with respect to time during the measurement. The position information is used to trigger the acquisition of force sensor data when the sample holder falls to within a certain range above the sensor. The displacement vs. time data is also used to determine the velocity just before impact, using a finite difference approximation. All sensor signals were measured using a 100 kHz analog data acquisition system (National Instruments PCI-MIO-16E-4).

Static, slow deformation. When static measurement is desired, the pulley is disabled and the electromagnet and ultrasound displacement sensor are switched off. The sample holder is detached from the guide rail and attached to a motorized DC-servo actuator (Newport® 850 G) using a coupling brace (see Figs. 2.3 and 2.4). The modified motor-sample holder setup is positioned over the x-y translation stage described above. A mini-beam load cell, (OMEGA® LCCEB-10), with a 10-pound load capacity is used to acquire static measurements. This sensor offers an accuracy of ± 2% and repeatability of ± 0.01% of full scale. The voltage output from the sensors contains noise from vibrations of the mechanical components and also from the electronics. The noise contribution in static measurements is higher because the prolonged direct film contact provides a mechanism for conducting vibrations from the rotating shaft of the motorized actuator. However, the magnitude of the noise is still very small compared to the magnitude of the signal obtained from the measurements. To maximize the signal to noise ratio, the output from the sensor is directly wired in to a signal conditioner, (OMEGA® DMD-465WB). This signal conditioner contains a precision differential instrumentation amplifier with filtered voltage output. The sensor also contains a highly regulated, low noise, adjustable sensor excitation source, which significantly reduces noise inherent in the power source. The amplified and filtered voltage output from the conditioner is directly connected to the same data acquisition system mentioned above. The sensor was calibrated with known weights using the procedure outlined by the manufacturer. A linear calibration curve was obtained and was used to convert the voltage measurements to force in Newtons.

2.3.3 Contact Tips

The indenter needles were spring temper wire (McMaster-Carr), custom-fabricated with a hemispherical cap shape (Figure 2.6). The needles, typically of length 25 mm, were embedded into 1/4x20 threaded screw caps (OMEGA) using an epoxy. The screw caps, in turn, could be screwed directly into the load sensors. Two indenters with diameters of 500 μm and 1.4 mm, were fabricated to allow different combinations of indenter radius and sample hole radius to understand the effect of the ratio of indenter to sample plate hole size on the measured properties. The advantage of using a hemispherical indenter is the absence of an imposed principal stress direction.[27] This means that for isotropic materials, the direction of crack propagation is random with respect to the contact tip.

2.3.4 Positioning Systems

Depending on the type of measurement desired, the appropriate sensor is attached to an x-y translation stage (Newport® 443 Series). The stage is coupled with precision DC-servo actuators (Newport® 850 G), feedback-controlled using the Newport ESP 6000 controller board. This allowed precise motion of the sensor from one impact site to another, prior to taking measurements. We found that noise picked up by the dynamic force sensor in particular was minimized when the sample was moved onto a stationary load cell, rather than pushing the indenter onto a fixed sample.

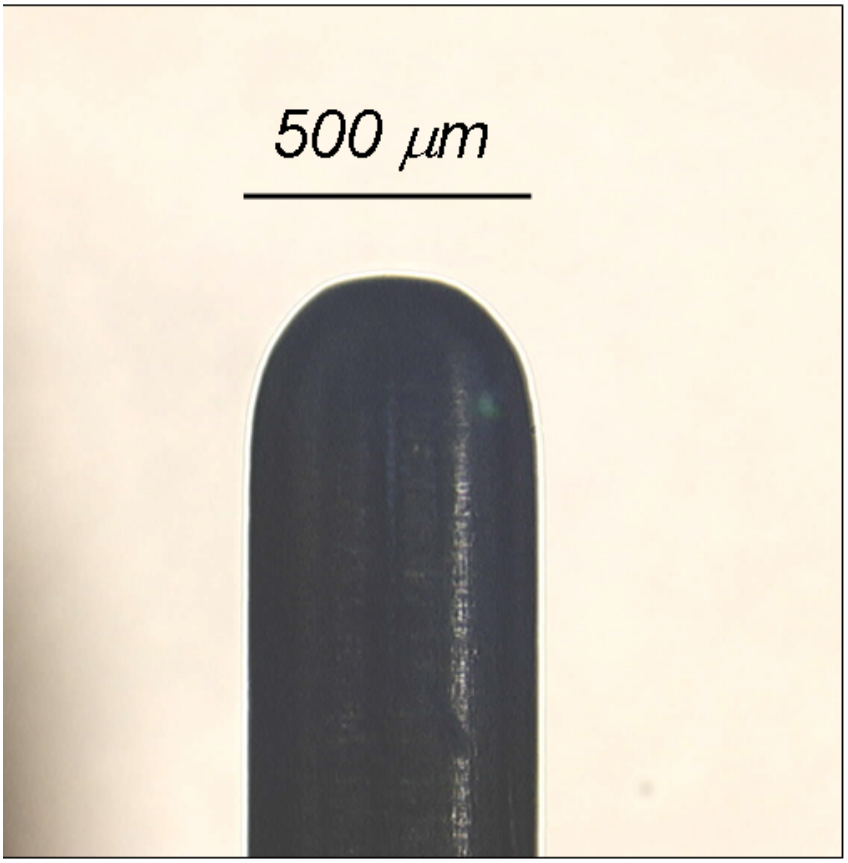

Figure 2.6: Contact tip image.

2.3.5 Measurement Sequence.

A custom LabView™ VI is used to coordinate measurement steps and data recording. In dynamic measurement mode, the electromagnet is switched on and the pulley raises the sample holder to attach the holder to the magnet. The sample holder is kept attached to the magnet and the pulley assembly lowered. The actuators connected to the x-y translation stage are used to move the sensor to the desired position for the first measurement. At this point, the electromagnet is switched off and the sample holder drops on the indenter which has been position precisely under one of the impact sites. As the indenter contacts the sample, the resulting force on the indenter is transferred to the sensor and the dynamic measurement is captured using the aforementioned data acquisition system at 50 kHz sampling rate. The force-time profile, along with the position of the test is saved to a text file for future analysis. This process is automatically repeated until the specified number of tests have been performed.

The procedure for automated slow or static measurement is similar to the procedure outlined above for the dynamic sensor. The indenter is initially centered at a reference hole in the sample plate using the actuators connected to the x-y translation stages. The initial height of the sample holder is adjusted using the actuator that is coupled with the holder so that the indenter can access all available impact sites without obstruction. At the start of the measurement, the x and y actuators move the sensor underneath the first impact site to be tested. After positioning the sensor in the desired location, the sample holder is lowered on to the tip of the indenter and the force is recorded. The process is repeated until the desired measurements have been completed. In static measurement mode, hysteresis and relaxation experiments can also be

performed. Relaxation experiment involve subjecting the film to a predetermined strain and measuring the resulting force-time profile for a very long time, until the materials completely relaxes, indicated by a leveling of the force-time profile. Hysteresis measurements are done by applying a force to the sample at a fixed rate up to a predetermined strain, followed by a removal of the force at the same rate. This type of measurement can be used to determine permanent set is materials.

2.4 DATA PROCESSING

A Matlab^{TM} code was developed to analyze the data files (forces) obtained from *HTMECH* experiments. The force data is converted to stress-strain data using knowledge of the strain rate and sample geometrical factors. Mechanical properties such yield strength, tensile strength, impact energy, and % elongation at break can be extracted and stored as a function of position on the library.

Figure 2.7a describes the geometry of the *HTMECH* apparatus at one particular measurement site, and Fig. 2.7b is a close-up schematic of the contact region between the film and the contact needle. Our apparatus utilizes needles and isolation grids that can explore a wide range of $\rho = R/r_0$ values from 0.05 to 0.5. We have chosen operational definitions of stress and strain that allow meaningful comparisons while maintaining as much as possible consistency with conventional definitions of stress and strain. The raw force data was converted to stress (σ) by dividing force by the area around the hole perimeter where the film is held: area = $2\pi r_0 h$, where h is the initial film thickness. The engineering strain (ε) was obtained by dividing the instantaneous radial deformation, $r(t)$, by the initial hole radius, r_0. The radial deformation was obtained by first converting

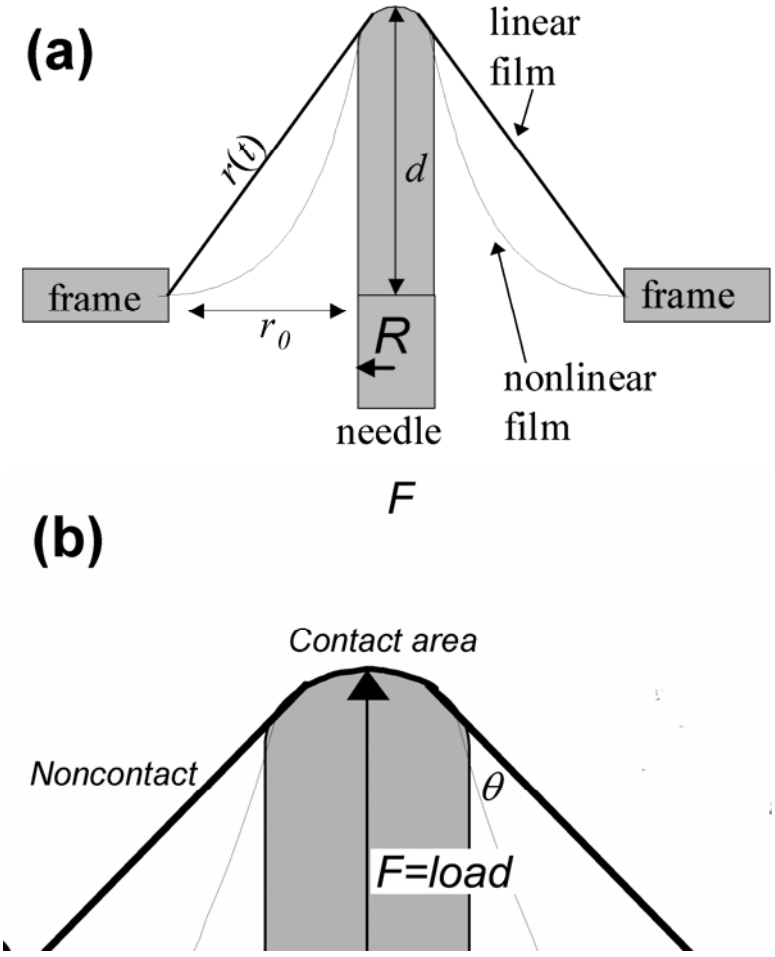

Figure 2.7: Generalized cross-sectional diagram of the "sandwiched" film under applied strain, (b) close-up of tip contact region.

time (t) into vertical needle penetration, $d = v_0 t$, where the strain rate v_0 changes by less than 1 % during impact.[19, 20] Assuming a linear film profile (see Figure 2.7), $r(t)$ is then found as the hypotenuse between the fixed hole radius, r_0, and d: $r(t) = (d^2 + r_0^2)^{1/2}$.[20] In the *HTMECH* apparatus, the force that is measured directly (F_Z) is the vertical (z-direction) component of the actual in-plane radial tensile force (F_R) developed in the film. The radial component is obtained from trigonometry as $F_R = F_Z / \cos(\theta)$, where $\cos(\theta) = d/(d^2 + r_0^2)^{1/2}$ and θ is the t-dependent angle between the film and the needle (Fig 2.7b). Measurement of the radial force from the measured vertical force leads to erroneously high values at low elongation, where the needle becomes nearly perpendicular to the film and $\cos(\theta) \approx 0$. When $\cos(\theta)$ is smaller than the measurement variance, artificially large stress calculations can occur, but this is confined to the first 10 to 20 % of strain.

It is important to note that the linear film radius, $r(t)$, assumed above does not always hold true. This assumption is true for purely elastic materials, as the linear film radius is the minimum value that $r(t)$ can obtain and leads to minimum elastic energy storage (Fig 2.7a). However, as plastic deformation or viscous flow begins to occur, it is expected and observed that the film profile becomes nonlinear with positive curvature (Fig 2.7a). This occurs because the true stress tangent to the film surface increases hyperbolically as $1 / r(t)$, since the film cross-sectional area is $2\pi r(t)h$. In order to lower free energy, the film deforms according to this variable stress if plastic deformation or viscoelastic relaxation is present. In *HTMECH*, the linear strain (ε) is therefore the minimum value obtainable (elastic only) and will be lower than the strain of a nonlinear film profile (plasticity or viscous behavior). However, in conventional uniaxial tests, the film always remains linear along the strain axis. A nonlinear film profile also leads to

smaller values of the angle θ than those predicted from a linear film profile. Hence, assuming a linear film profile induces an erroneously large stress measurement if the material actually has plastic or viscoelastic characteristics. We thus expect differences in the magnitude of stress and strain between conventional uniaxial tensile versus *HTMECH* measurements in samples that exhibit plastic deformation or viscous behavior. Fortunately, these errors in stress (overestimated) and strain (underestimated) will cancel in the calculation of modulus: $E = \sigma / \varepsilon = [F_Z * (d^2 + r_0^2)^{1/2} / (d2\pi r_0 h)] / [(d^2 + r_0^2)^{1/2} / r_0]$ $= [F_Z / 2\pi dh]$. The $[(d^2 + r_0^2)^{1/2}]$ term indicating the instantaneous deformed film radius cancels in the modulus determination, and moduli from the uniaxial and *HTMECH* (radial) instruments should be identical barring any other artifacts.

Figure 2.8 illustrates the sequence that is followed in our MATLAB™-based data analysis routine. Fig. 2.8a shows a typical raw data plot of force versus time from impacting a blend of 40 % by mass poly(styrene-b-butadiene) (KRATON™) with 60 % by mass polystyrene (Aldrich) at strain rate of about 800 mm/s. In this example, the sample rate was 50 kHz and the number of samples collected after the triggering of the dynamic sensor was 20,000. Hence, the entire range of Fig. 2.8a is 400 ms. The figure shows that numerous distinct "events" (spikes in the data) are recorded over a somewhat-noisy linear baseline. The linear baseline with a positive slope is an artifact of the piezoelectric sensor discharge, and is easily corrected by subtracting a line from the raw data. The baseline is estimated as a line formed between the first and last data-points. After baseline subtraction, and some focusing onto the actual impact event, the data appears as in Figure 2.8b. The actual impact event is always the first spike recorded by the sensor, after the triggering event (the falling sample holder triggers the load cell at a

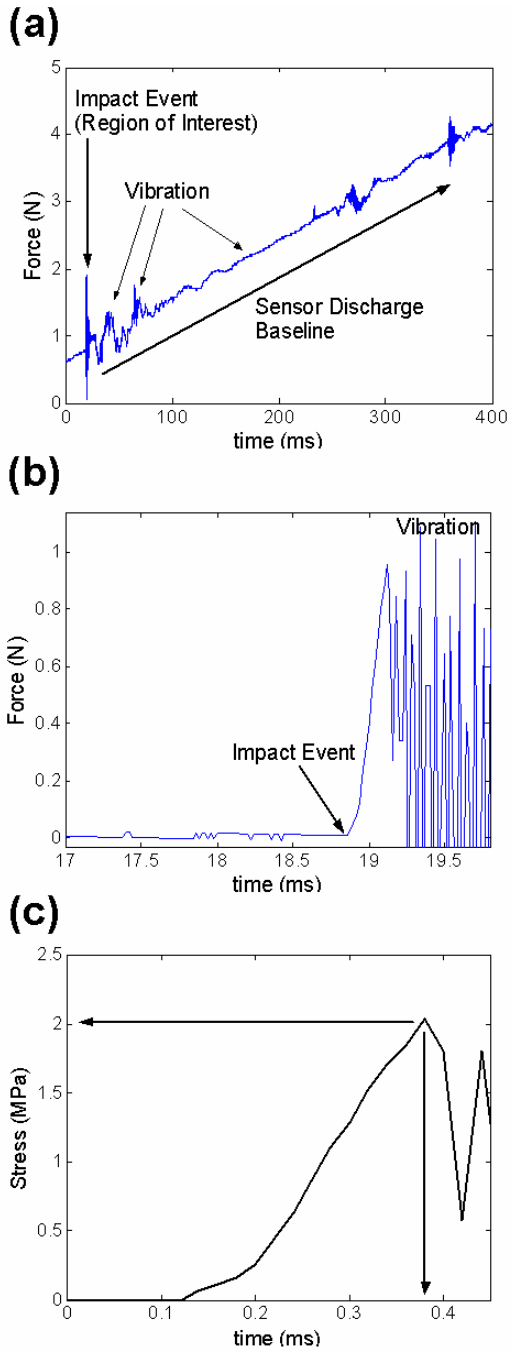

Figure 2.8: (a) Raw force versus time data for a typical impact of a polystyrene + poly(styrene-b-butadiene) blend film, 50 μm thickness (b) Data from (a) focused on impact region after baseline subtraction, (c) Data from (b) after noise leveling and region of interest selection, with identification of useful mechanical parameters.

certain height). Hence the impact event is easy to locate numerically. Fig. 2.8b illustrates the typical noise level encountered in an impact event. Usually, the noise level is determined by finding the peak-to-peak range of the signal prior to the impact event, using the MATLAB™ range function. Then, any fluctuation below the peak-to-peak noise level is automatically zeroed. The numerical routine then passes sequentially through the force data and locates the maxima (yield and failure points), and selects out only the data in the direct (+/- 10 data points) vicinity of the impact-to-failure event. Usually the entire event from impact to failure is finished in a few milliseconds. Of course, the static and slow data is treated in the same manner, although the time to failure is much longer, over the order of several seconds. Once the region-of-interest is selected, it is saved along with values of the yield and tensile strengths and the % elongation at break. Sometimes the impact energy is recorded also by taking the integral of force over time.

The statistical repeatability of the force-time (or stress-strain) curves has been demonstrated in previous publications, and those details are not repeated here.[4-6] Generally, the 95 % confidence intervals on stress measured at a given strain are +/- 1 MPa for films that have a tensile strength under 50 MPa. Figure 9a shows several force versus time profiles measured with *HTMECH* for various chemically-distinct polymers, and figure 9b shows the equivalent stress-strain profiles for the data represented in figure 9a. It is apparent that *HTMECH* is capable of sensitive detection of the mechanical responses of chemically-distinct materials. In particular, we point out the difference between purely elastic materials like PET and PBT, large elongation elastomers like polyetheramide, and the elastic-plastic response of polyamides. Comparison between

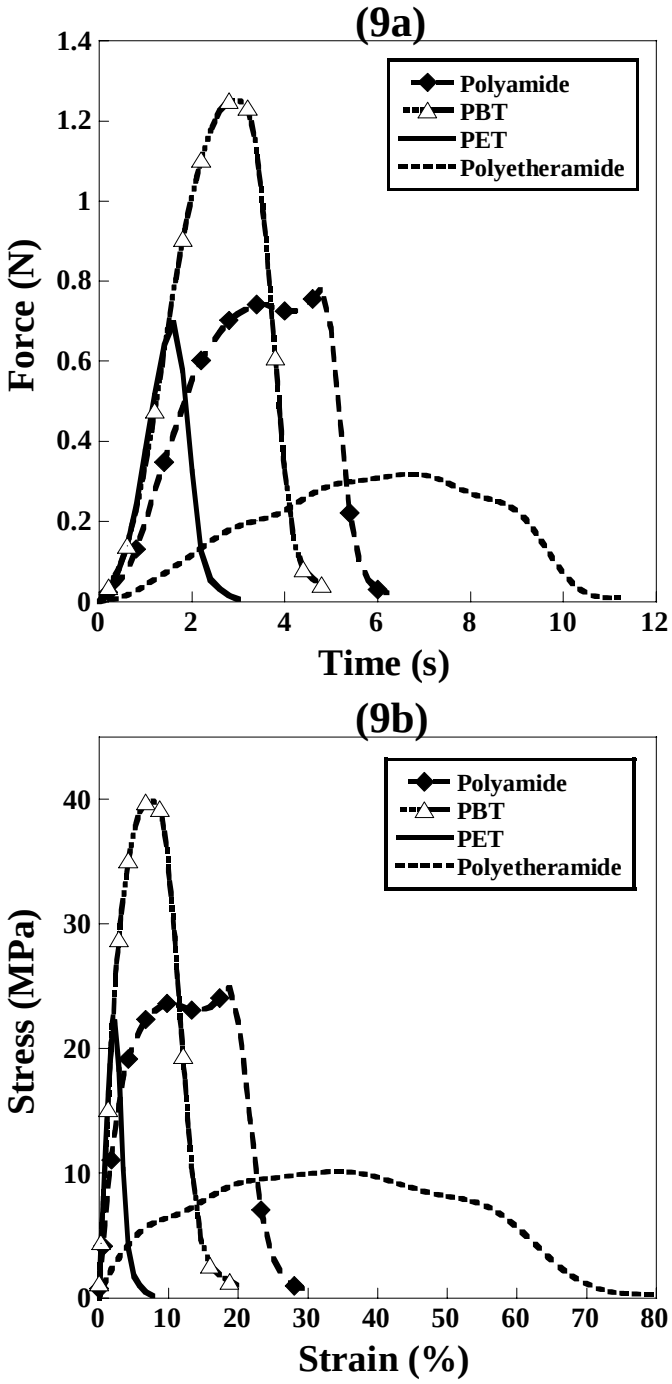

Figure 2.9: (a) Typical force versus time data from chemically distinct polymers, indicating the ability to detect mechanical differences between material classes; (b) corresponding stress-strain curves for figure (a). PET=poly(ethylene terepthalate), PBT=poly(butylene terepthalate). Polymers courtesy of ATOFINA Chemicals, Inc.

HTMECH and uniaxial (not shown) indicates that the same features are detected for each polymer class, although absolute values are different.

Previously, we demonstrated the correlation between elastic moduli measured for a series of five poly(urethane ureas) on both *HTMECH* (biaxial) and uniaxial (Instron 5842) instruments at 30 mm/s strain rate.[21] The difference in chemistry causes a variation in the observed elastic modulus at 100% elongation, and even results in a transition from pure elastomeric to plastic behavior. Nevertheless, a strong linear correlation is found between the *HTMECH* and uniaxial results, with a coefficient of $E_{HTMECH} = 1.35E_{UNIAXIAL}$. Remarkably, this correlation coefficient (1.375) is almost equal to the coefficient of 1.375 predicted by Wan and Liao[18] for the analytical solution to the membrane equations (1) and (2) in the point-load limit ($\rho \rightarrow 0$).

This instrument can also be used to characterize viscoelastic polymers. However, care must be taken when comparing the measurements obtained from this instrument with measurements from an Instron for viscoelastic polymers. As stated earlier, the load versus deflection curves is dependent on the ratio of the tip radius to the hole radius, ρ. For larger values of ρ, the amount of contact between the sample and the contact tip is larger, indicating that the contribution of shear to the overall stress is larger. This shear contribution gets even larger for viscoelastic polymers, if the polymer is stretched beyond its yield stress. Beyond the yield stress, permanent plastic deformation occurs. This could lead to a larger contact area between the contact tip and the material, increasing the shearing contribution to the overall stress in the film. Figure 2.10 shows the effect of ρ on the stress-stress behavior of poly methyl methacrylate (PMMA).

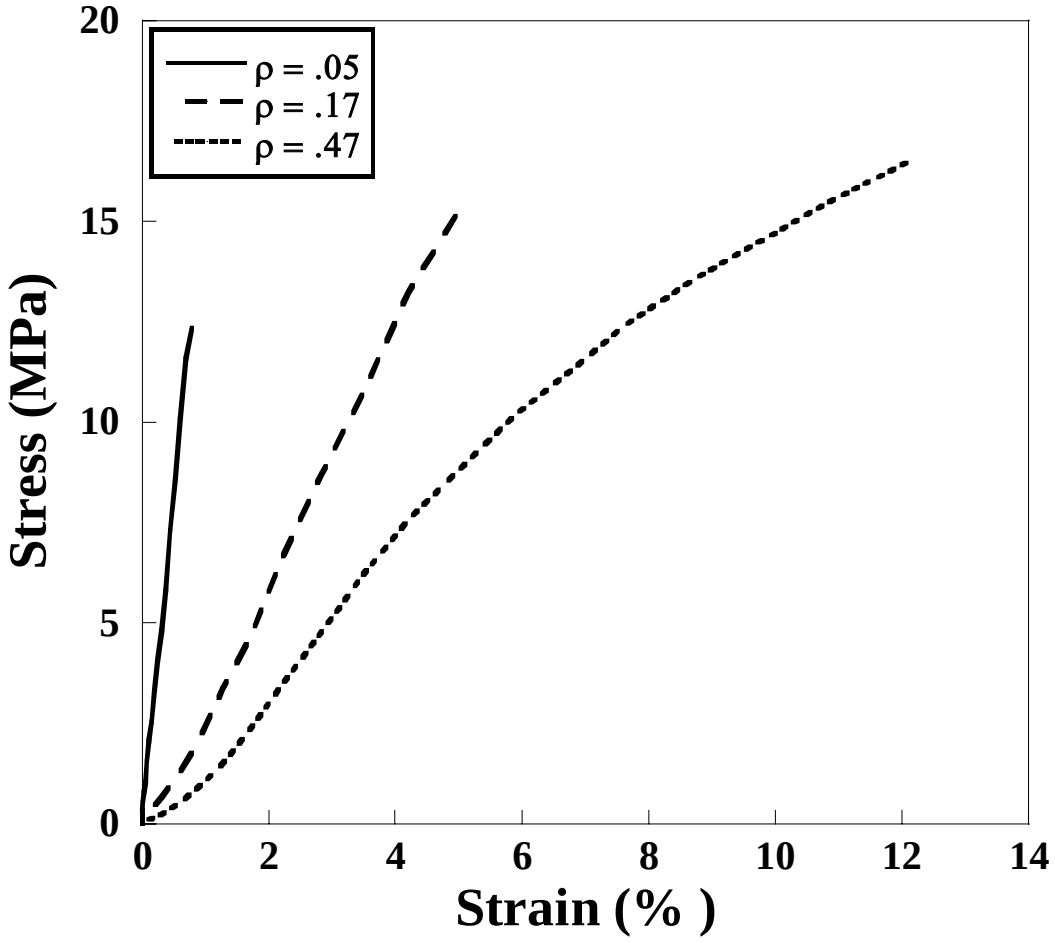

Figure 2.10: The effect of geometry on the stress-strain profile of PMMA. Profiles were obtained at different ρ (indenter radius/hole radius) using the *HTMECH*.

PMMA is model plastic material and is expected to show a linear stress-strain profile when subjected to small uniaxial tensile deformation. Figure 2.10 shows a strong dependence of both the tensile strength and elongation at break on ρ. Another significant observation in Figure 2.10 is the differences in the shape of the stress-strain profiles at different ρ values. The shapes of these profiles can be approximated by combining straight lines with different slopes. The profile corresponding to ρ = 0.05 can be approximated by a straight line with one slope, and the profiles corresponding to ρ = 0.17 and ρ = 0.47 can be approximated by combining straight lines with two and three different slopes respectively. Insight from the fracture mechanics of a shaft-loaded blister test suggests that these slopes account for the different stress contributing factors: (1) bending stress, (2) tensile stress), and (3) shear stress.[18,26,27] The change in slope in the shape of these profiles usually indicate a transitioning from one dominant stress contributor to another. For example, a change in slope is expected during deformation if the dominant stress changes from tensile to shear. This can be seen in Figure 2.10, for ρ = 0.47. The profile corresponding to ρ = 0.05 showed a linear stress-strain curve, typical of what is expected for PMMA at very small uniaxial deformation. However, at this geometry, only nine independent measurements can be made with the *HTMECH*. When ρ = 0.47, the indenter diameter is large, relative to the size of the hole. This provides a lot of contact area for the film, there by increasing the shearing contribution to the overall stress at very high elongations. The contribution of shear to the overall stress could be minimized by lubricating the indenter prior to deformation.

Except otherwise stated, all *HTMECH* measurements in the remainder of this thesis were taken at ρ = 0.17. At this geometry, shear is negligible and the bending

contribution to the overall stress is minimized as shown in Figure 2.10 (very small initial slope). Bending contributions to the overall stress could also be further minimized by using thinner films.[26] Compared to $\rho = 0.05$ where only nine measurement are possible, up to one hundred measurements are possible at $\rho = 0.17$, making this geometry suitable for high-throughput screening of free-standing polymer libraries and also for comparing the *HTMECH* with commercial instruments like the INSTRON®, which operates primarily in tension.

2.5 REFERENCES

(1) Jandeleit, B., Schaefer, D.J., Powers, T.S., Turner, H.W., Weinberg, W.H., Combinatorial Materials Science and Catalysis. *Agnew. Chem. Int. Ed.* **1999,** 36, 2494.

(2) Meredith, J. C.; Karim, A.; Amis, E. J., High-Throughput Measurement of Polymer Blend Phase Behavior. *Macromolecules* **2000,** 33, (16), 5760.

(3) Meredith, J. C.; Smith, A. P.; Karim, A.; Amis, E. J., Combinatorial Materials Science for Polymer Thin-Film Dewetting. *Macromolecules* **2000,** 33, (26), 9747.

(4) Tomlinson, M. R.; Genzer, J., Formation of Grafted Macromolecular Assemblies with a Gradual Variation of Molecular Weight on Solid Substrates. *Macromolecules* **2003,** 36, (10), 3449.

(5) Tomlinson, M. R.; Genzer, J., Formation of Surface-Grafted Copolymer Brushes with Continuous Composition Gradients. *Chem. Commun.* **2003**, 1350.

(6) Beers, K. L., Douglas, J.F., Amis, E.J., Karim, A., Combinatorial Measurements of Crystallization Growth Rate and Morphology in Thin Films of Isotactic Polystyrene. *Langmuir* **2003,** 19, 935.

(7) Hoogenboom, R., Meier, M.A.R., Schubert, U.S., Combinatorial Methods, Automated Synthesis and High-Throughput Screening in Polymer Research: Past and Present. *Macromol. Rapid Comm.* **2003,** 24, 15.

(8) Chapon, P., Mignaud, C., Gilda, L., Destarac, M., Automated Parallel Synthesis of MADIX (Co)Polymers. *Macromol. Rapid Comm.* **2003,** 24, 87.

(9) Zhang, H., Fijten, M.W.M., Hoogenboom, R., Reinierkens, R., Schubert, U.S., Application of Parallel Synthetic Approach in Atom-Transfer Radical Polymerization: Set-Up and Feasibility Demonstration. *Macromol. Rapid Comm.* **2003,** 24, 81.

(10) Brocchini, S.; James, K.; Tangpasuthadol, V.; Kohn, J., A Combinatorial Approach to Polymer Design. *J. Am. Chem. Soc.* **1997,** 119, 4553.

(11) Dickinson, T. A.; Walt, D. R.; White, J.; Kauer, J. S., Generating Sensor Diversity Through Combinatorial Polymer Synthesis. *Anal. Chem.* **1997,** 69, 3413.

(12) Hoogenboom, R.; Meier, M. A. R.; Schubert, U. S., Combinatorial Methods, Automated Synthesis and High-Throughput Screening in Polymer Research: Past and Present. *Macromol. Rapid Comm.* **2003,** 24, 15.

(13) Klein, J.; Lehmann, C. W.; Schmidt, H.-W.; Maier, W. F., Combinatorial material libraries on the microgram scale with an example of hydrothermal synthesis. *Angew. Chem. Int. Ed.* **1998,** 37, 3369.

(14) Maier, W. F.; Kirsten, G.; Orschel, M.; Weiss, P.-A.; Holzwarth, A.; Klein, J., Combinatorial Chemistry of Materials, Polymers, and Catalysts. *ACS Symposium Series* **2001,** 814, 1.

(15) Schmitz, C.; Thelakkat, M.; Schmidt, H. W., A Combinatorial Study of the Dependence of Organic LED Characteristics on Layer Thickness. *Adv. Mater.* **1999,** 11, (10), 821.

(16) Schulz, M.; Schedler, U.; Matuschewski, H.; Wenschuh, H., New continuous Polymeric Surfaces for SPOT Synthesis, Combinatorial Chemistry, Compound Libraries, and High-Throughput Applications. *Proceedings of SPIE* **2000,** 4200, 96.

(17) Terrett, N. K., *Combinatorial Chemistry*. Oxford: Oxford, **1998**.

(18) Xiang, X.-D.; Sun, X.; Briceno, G.; Lou, Y.; Wang, K.-A.; Chang, H.; Wallace-Freedman, W. G.; Chen, S.-W.; Schultz, P. G., A Combinatorial Approach to Materials Discovery. *Science* **1995,** 268, 1738.

(19) Sormana, J.-L., Meredith, J.C., High-Throughput Dynamic Impact Characterization of Polymer Films. *Mater. Res. Innov.* **2003,** 7, (5), 295.

(20) Sormana, J.-L., Meredith, J.C., High-Throughput Screening of Mechanical Properties on Temperature-Gradient Polyurethaneurea Libraries. *Macromol. Rapid Comm.* **2003**, 118.

(21) Sormana, J.-L.; Meredith, J. C., High-Throughput Discovery of Structure-Mechanical Property Relationships for Segmented Poly(urethane-urea)s. *Macromolecules* **2004,** 37, 2186.

(22) Mansky, P. High Throughput Mechanical Rapid Serial Property Testing Materials Libraries. US6736017, **2004**.

(23) D638-03, A., Standard Test Method for Tensile Properties of Plastics. In *Annual Book of ASTM Standards*, ASTM International: Philadelphia, **2003**; Vol. 08.01.

(24) D3420-95, A., Standard Test Method for Pendulum Impact Resistance of Plastic Film. In *Annual Book of ASTM Standards*, ASTM International: Philadelphia, **2002**; Vol. 08.02.

(25) 527-1, I., Plastics -- Determination of tensile properties -- Part 1: General Principles. In International Organization for Standardization: Geneva, **1993**.

(26) Brown, R. P., *Handbook of Plastics Test Methods*. George Goodwin Limited in association with the Plastics and Rubber Institute: London, **1981**.

(27) Jones, D. P., Leach, D.C., Moore, D.R, The Application of Instrumented Falling Weight Impact Techniques to the Study of Toughness in Thermoplastics. *Plastics, Rubber and Composites Processing and Applications* **1986,** 6, 67.

(28) Reed, P. E., Falling Weight Impact Testing and Design. *Plastics, Rubber and Composites Processing and Applications* **1992,** 17, 157.

(29) Toropov, A. I., Grosso, M., Dynamic Calibration of Impact Test Instruments. *J. Testing and Evaluation, JTEVA* **1998,** 26, (4), 315.

(30) Ireland, D. R., Procedures and Problems Associated with Reliable Control of the Instrumented Impact Test. In *Instrumented Impact Testing, ASTM STP 563*, American Society for Testing and Materials: Philadelphia, **1974**; pp 3.

(31) D1709-04, A., Standard Test Methods for Impact Resistance of Plastic Film by the Free-Falling DART Method. In *Annual Book of ASTM Standards*, ASTM International: Philadelphia, **2003**; Vol. 08.01.

(32) D4272-03, A., Standard Test Method for Total Energy Impact of Plastic Films By DART Drop. In *Annual Book of ASTM Standards*, ASTM International: Philadelphia, **2003**; Vol. 08.02.

(33) D5628-96, A., Standard Test Method for Impact Resistance of Flat, Rigid Plastic Specimens by Means of a FALLING DART. In *Annual Book of ASTM Standards*, ASTM International: Philadelphia, **2001**; Vol. 08.03.

(34) D3763, A., Standard Test Method for High Speed Puncture Properties of Plastics Using Load and Displacement Sensors. In *Annual Book of ASTM Standards*, American Society For Testing and Materials: Philadelphia, **1999**.

(35) 7765-1, I., Plastic Film and Sheeting-Determination of Impact Resistance by the Free FALLING DART Method-Part 1: Staircase Method. In International Organization for Standardization: Geneva, **1988**.

(36). 7765-2, I., Plastics Film and Sheeting-Determination of Impact Resistance by the Free FALLING DART Method-Part 2: Instrumented Puncture Test. In International Organization for Standardization: Geneva, **1988**.

(37) Begley, M. R.; Mackin, T. J., Spherical Indentation of Freestanding Circular Films in the Membrane Regime. *J Mech Phys Solids* **2004,** 52, 2005.

(38) Komaragiri, U.; Begley, M.; Simmonds, J., The Mechanical Response to Freestanding Circular Elastic Films Under Point and Pressure Loads. *J. Appl. Mech.* **2004**, in press.

(39) Liu, K. K., Ju, B. F., A Novel Technique for Mechanical Characterization of Thin Elastomeric Membrane. *J. Phys. D. Appl. Phys.* **2001,** 34, (15), 91.

(40) Scott, O. N.; Begley, M. R.; Komaragiri, U.; Mackin, T. J., Indentation of Freestanding Circular Elastomer Films Using Spherical Indenters. *Acta Materialia* **2004,** 52, 4877.

(41) Vernon, P.; Mackin, T.; Begley, M., Fatigue Testing of Polymer Membranes. *Polym. Compos.* **2004**, (in press).

(42) Wan, K.-T., Liao, Kin, Measuring Mechanical Properties of Thin Flexible Films by a Shaft-Loaded Blister Test. *Thin Solid Films* **1999,** 352, 167.

(43) Yang, W. H., Hsu, K.H., Indentation of a Circular Membrane. *J. Appl. Mech.* **1971,** 38, 227.

(44) Yang, W. H.; Feng, W. W., On Axisymmetric Deformations of Nonlinear Membranes. *J. App. Mechanics* **1970,** 34, 1002.

(45) Kalkman, A. J.; Verbruggen, A. H.; Janssen, G. C. A. M.; Groen, F. H., A Novel Bulge-Testing Setup for Rectangular Free-Standing Thin Films. *Rev. Sci. Instrum.* **2000,** 70, (10), 4026.

(46) Small, M. K., Nix, W.D., Analysis of the Accuracy of the Bulge Test in Determining the Mechanical Properties of Thin Films. *J. Mater. Res.* **1992,** 7, (6), 1553.

(47) Oliver, W. C.; Pharr, G. M., Measurement of Hardness and Elastic Modulus by Instrumented Indentation: Advances in Understanding and Refinements to Methodology. *J. Mater. Res.* **2004,** 19, (1), 3.

(48) VanLandingham, M. R., Review of Instrumented Indentation. *J. RES. NIST* **200,** 108, (4), 249.

(49) Bhushan, B.; Li, X. D., Nanomechanical Characterisation of Solid Surfaces and Thin Films. *International Materials Reviews* **2003,** 48, 125.

(50) Wan, K.-T.; Guo, S.; Dillard, D. A., A Theoretical and Numerical Study of a Thin Clamped Circular Film Under an External Load in the Presence of a Tensile Residual stress. *Thin Solid Films* **2003,** 425, 150.

(51) Yang, W. H.; Hsu, K. H., Indentation of a Circular Membrane. *J. Appl. Mech.* **1971**, 227.

(52) Wan, K.-T.; Liao, K., Measuring Mechanical Properties of Thin Flexible Films by a Shaft-Loaded Blister Test. *Thin Solid Films* **1999,** 352, 167-172.

(53) Green, A. E., Adkins, J. E., *Large Elastic Deformations*. Oxford University Press: Oxford, **1960**.

(54) Wan, K.-T., Fracture mechanics of a shaft-loaded blister test - Transition from a bending plate to a stretching membrane. *J. Adhesion* **1999,** 70, 209.

CHAPTER 3

HIGH-THROUGHPUT DYNAMIC IMPACT CHARACTERIZATION OF POLYMER FILMS

An instrumented falling weight impact apparatus has been designed and constructed for high-throughput characterization of polymer films in the 5 μm to 100 μm thickness range. The primary intended use of the instrument is rapid and accurate characterization of the dynamic impact response of multiple (~100) positions on a combinatorial library film. This will allow future exploration of the dependence of mechanical response on polymer composition, thickness, and annealing temperature using combinatorial synthesis and characterization methods. This paper describes the instrument and presents validation measurements using polyethylene films of uniform thickness (25 μm) and poly(urethaneurea) elastomers of thicknesses from 10 μm to 30 μm. Measurements on the polyethylene film demonstrate the reproducibility and lack of interaction effects for multiple measurements on the same film. Poly(urethaneurea) elastomer impact measurements were used to indicate the instrument sensitivity to controlled variations in polymer chemistry and structure. In particular, from force-deformation profiles, the results indicate an optimum curing temperature and the expected trend in mechanical response with respect to polyurethaneurea diamine curative composition.

3.1 INTRODUCTION

The use of polymers in structural applications, packaging, coatings, biomaterials, microelectronics, and nanotechnology drives the need for continuous advances in their synthesis and characterization. However, the complex thermodynamic and rheological behavior of polymers and the large parameter space involved in polymer processing challenges the conventional paradigm of 1-sample-1-measurement synthesis and characterization. Combinatorial methods (CM) offer an excellent experimental paradigm for performing high-throughput measurements. The combinatorial method consists of: (1) experimental design, (2) preparation of sample libraries with a large number of thicknesses and annealing temperatures, (3) high-throughput measurements of relevant properties, and (4) analysis.[1] Originally developed for pharmaceutical research, combinatorial methods have been applied successfully to discover and characterize a wide variety of inorganic and organic materials.[1-4] The benefits of high-throughput methods include reduced variance and increased repeatability, efficient hypothesis testing, and reduced risk of overlooking unexpected behavior. Meredith et al.[2,3] have developed combinatorial methods for the characterization of polymers, based upon sample libraries with gradients in composition, thickness and process temperature. This approach has led to successful combinatorial characterization of phase behavior in polymer blends,[3] thin-film diblock copolymer segregation,[4] and thin film dewetting.[2] These previous combinatorial studies relied upon microscopy and spectroscopy as high-throughput screening tools. However, many experiments and applications require mechanical characterization as well. For this reason, the purpose of this paper is to

introduce a high-throughput instrumented impact measurement apparatus that can be used for characterization of gradient combinatorial libraries.

Mechanical properties are used to characterize polymers because they are sensitive indicators of changes in chemistry, structure, and phase behavior. In addition, mechanical properties such as modulus, ultimate strength, failure mechanism, and deformation at failure are useful in setting engineering limitations in load bearing applications. Because impact measurements are rapid and occur at high strain rate, they seem ideally suited for implementation in a high-throughput mode for combinatorial characterization. A variety of impact instruments, e.g., Charpy and Izod, have been developed and are available commercially.[5,6,7] The difference between impact tests lies in the induced stress state and the failure mode, which are influenced by the impact geometry, specimen shape, strain rate and temperature. In addition, to eliminate the energy of crack initiation from measurements, samples are sometimes notched. Instrumented impact instruments utilize a dynamic force sensor to measure the time-dependent force during impact. A popular example is the falling weight impact apparatus,[8-14] in which a weighted hemispherical tup is dropped onto a thin sheet or film of rigidly mounted polymer. Instrumentation can help elucidate the failure mode (brittle or ductile), modulus, elongation to break, and energy stored under a given set of test conditions. Without instrumentation, a single impact energy at failure is obtained, which may not provide the information needed to make the chemical modifications that will result in a material with desired properties.

However, instrumented impact tests are not without limitations. Because the measured force versus deformation, and all derived properties such as impact energy,

depend upon the impact geometry, temperature, strain-rate, and presence of notches, it is very difficult to compare results from one type of impact test to another. In addition, because the dynamic mechanical response of polymers under stress depends on the strain rate, it is often necessary to obtain impact tests over a large range of strain rates or temperatures in order to observe transitions between failure modes, e.g., ductile to brittle. However, the purpose of the present work is to develop a high-throughput, yet accurate method to identify the dependence of mechanical response on the chemistry, thickness, and annealing temperature differences within a self-contained combinatorial library. As with all combinatorial measurements, the objective is to identify important trends or material responses prior to performing detailed characterization with conventional instrumentation.

In this paper we present a miniaturized instrumented falling weight impact apparatus designed for high-throughput characterization of polymers. The instrument operates at a range of strain rates and can also collect force-deformation measurements at near static conditions. After describing the apparatus, validation measurements are presented to demonstrate the utility of the instrument for future characterization of combinatorial film libraries. In particular we present characterization of the instrument repeatability, dependence of measured impact properties on sample film thickness, and the sensitivity of the measured force-deformation to chemical and structural changes in polymers. Two model test systems, thermoplastic polyethylene and an elastomeric poly(urethaneurea) are used to perform these demonstration and validation measurements.

3.2 EXPERIMENTAL

3.2.1 Experimental Setup

The high-throughput impact experiment is shown in Figure 3.1. Because the combinatorial libraries developed previously are films with lateral (in-plane) variations in chemistry and processing temperature, we adopt a geometry in which an impact tip contacts the sample normal to the combinatorial library film. This results in a biaxial tensile deformation, similar to larger, nonhigh-throughput falling weight instruments.[8-14] Samples are enclosed between two stainless steel plates, perforated by a 10x10 grid of holes with a diameter of 3 mm and a distance of 1 mm between neighboring holes. The plates provide uniform pressure on the sample, prevent slippage, and act to isolate the 100 individual impact sites during testing. The sample plates are mounted onto a ball-bearing guide rail. The total mass of the sample plates and its holder is 1.03 kg. An ultrasonic displacement sensor (Migatron RPS-401A-40) is used to measure the velocity of the sample during the impact tests. Samples are released from a fixed height and allowed to drop onto a hemispherical contact tip that is positioned precisely under one of the 100 impact positions using an *x, y* translation stage (Newport). Force-time measurements were collected using a Labview® data acquisition card. Data collection started when the sample is about 5 mm away from the contact tip. This corresponds to a sample velocity of 0.89 m/s The advantage of using a hemispherical contact tip is the absence of an imposed principal stress direction.[9] This means that for isotropic materials, the direction of crack propagation is random with respect to the contact tip. Commercial falling weight impact instruments often use large impact tups, e.g., 12 to 25 mm diameter,[8-14] that are not appropriate for the miniaturized combinatorial libraries. For

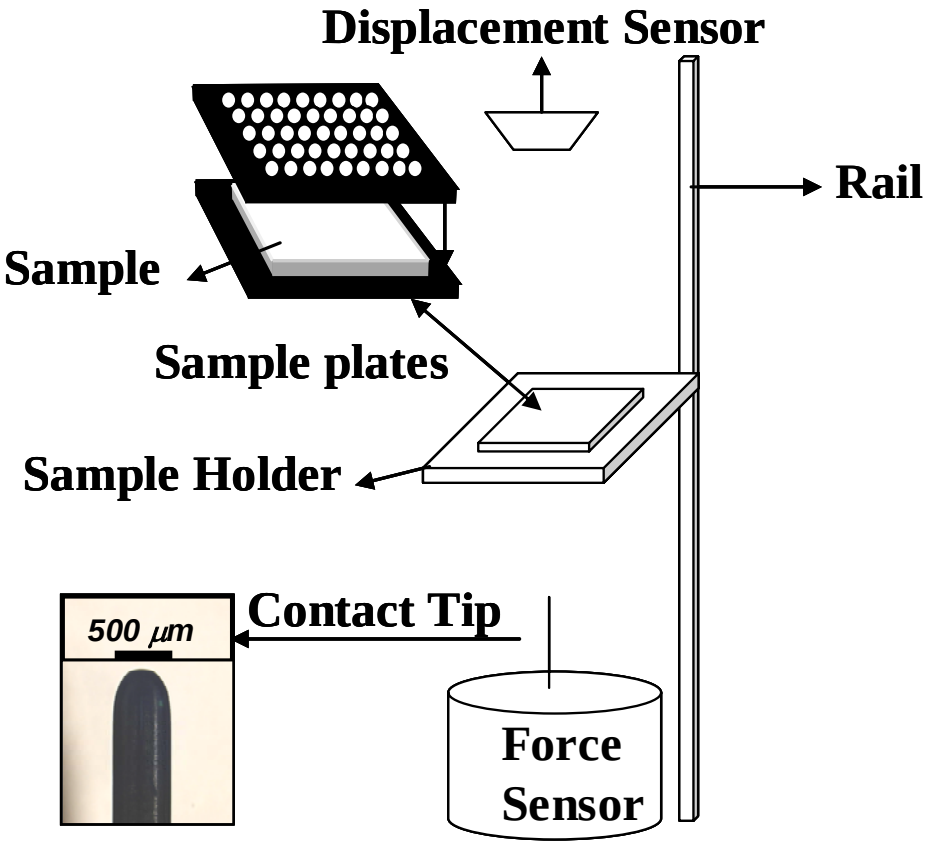

Figure 3.1: Experimental setup of the high-throughput impact apparatus.

example, a typical library film has dimensions of 25 x 25 mm. Thus, we used hemispherical contact tips with a 500μm diameter, fabricated from spring temper steel wire. A microscope image of a typical impact tip is included in Figure 3.1. These tips are embedded in a steel cap that is screwed onto a piezoelectric force sensor (Omega DLC101-10), which records the force on the tip during tests. All measurements were recorded at room temperature, 24 ^{o}C.

3.2.2 Data Analysis

Instrumented impact tests provide force-time or force-deflection data, which is subsequently used to obtain information on the initial impact slope, maximum impact force, deformation at failure and impact energy of a material. The impact energy is as the integrated area under the force-time impact curve. Many polymers follow a Hookean behavior at the early stages of deformation, characterized by a linear relationship between force and deformation. The proportionality constant is a measure of the strain-rate-dependent elastic modulus, a sensitive function of material chemistry and structure. Raw data from the measurements are in force, $F(t)$, versus time, t. This data can be converted to force versus displacement, $x(t)$, by converting time to distance using the Newtonian expression $x(t) = v_i t + 0.5F(t)t^2/m$, where v_i is the impact velocity and m is the sample mass. Data obtained from impact tests usually contains a combination of the true mechanical response of the material and artifacts such as inertial loads, slope discontinuities and harmonic oscillations.[8-14] The inertial load results from the deceleration of the sample as it initially contacts the impact tip. An example can be seen in the small amplitude bumps in the first 2 ms of Figure 3.8. A large inertial load may prevent accurate collection of the true mechanical response. Harmonic oscillations result

from vibration of the contact tip and other instrument components at their natural frequencies during impact (see Figure 3.3). Slope discontinuities are often attributed to crack initiation (see Figure 3.3). In our results, the amplitude of the inertial loads, slope change and oscillations are small relative to the overall signal.

The conversion of force-time or force-deflection data to impact energy involves the application of Newtonian mechanics and thermodynamics to the sample and contact tip. In the case of the falling weight impact test described in Figure 3.1, the specimen is dropped from a fixed height onto the contact tip, and the force on the contact tip is recorded with time. Eq. 3.1 below is the impulse-momentum equation and Eq. 3.2 is a kinetic energy balance for the impact event.

$$\int_{t_i}^{t_f} F(t)dt = m(v_f - v_i) \tag{3.1}$$

$$\Delta E_K = E_{K,f} - E_{K,i} = \frac{1}{2}m(v_f{}^2 - v_i{}^2) \tag{3.2}$$

In these equations F, t, m, E, v_i, and v_f represent the force, time, mass of specimen, kinetic energy, initial and final (at failure) velocity, respectively. It is important to note that the drag force and energy loss due to friction in the rail are neglected in Eqs. (3.1) and (3.2). Typically, for specimens investigated here, the velocity loss between initial impact and failure, is within 1% of the total sample kinetic energy. Hence, the change in sample velocity during impact can be neglected, e.g., $v_i \approx v_f$. With this simplification,

combination of Eqs. (3.1) and (3.2) gives an equation that can be used to measure the energy storage capability of the sample during impact.

$$\Delta E_K = v_i \int_{t_i}^{t_f} F(t)dt \tag{3.3}$$

The output from most piezoelectric force sensors is either in voltage or ampere. Calibration of the sensor with known loads is required before analysis can be performed. Because of the short discharge time constant of piezoelectric crystals, dynamic calibration is recommended.[11] A linear relationship between the signal and the actual force is usually obtained and the calibration constant is the slope, *C*, of the line $F(t) = CV(t)$, where $V(t)$ is voltage.[11] We calibrated the force sensor by dropping elastomeric balls of known mass on the screw cap from a fixed height and recording the voltage-time data. The energy transferred to the ball was calculated from the initial and final rebound height of the ball, found from a video recording of the impact event. This energy, ΔE_K, and the expression $F(t) = CV(t)$ was substituted into Eq. 2.3 to obtain a nearly perfect linear relationship between ΔE_K and the integral of $V(t)$. The correlation constant was r^2 = (mean square error between line and data)/(data variance) = 0.9998. The calibration constant was C = 9.191 N/V, which agrees within 2 % with that of the manufacturer, 9.054 N/V.

3.2.3 Materials and Procedure

Polyethylene films of uniform thickness (25 μm) and poly(urethaneurea) elastomer films (thickness = 10 to 30 μm) were used in this study. Poly(urethaneurea) elastomers were prepared by mixing a toluene diisocyanate-poly(tetramethylene glycol)

prepolymer (Air Products and Chemicals, Airthane® PET-85A) and a trimethylene glycol di-*p*-aminobenzene (Air Products and Chemicals, VERSALINK® 740-M) curative (chain extender) to a total concentration of 30 mass % in tetrahydrofuran (VWR, ACS Grade). The prepolymer and curative were mixed in a series of ratios between 80 mole % and 150 mole % of the stoichiometric amount of curative needed to react with all the isocyanate groups. The mixtures were coated on a Piranha-etched (70% H_2SO_4: 9% H_2O_2, 21% H_2O @ 80 ^oC for 1.5 h) silicon wafer. These mixtures were cured in a vacuum oven for 6 h at temperatures of either 80 ^oC, 90 ^oC, or 100 ^oC to give poly(urethaneurea) films. The conversion of isocyanate and the presence of urea linkages were confirmed with FTIR spectroscopy. Thickness was determined by visible-near infrared interferometry (Stellar Net EPP2000).

The elastomer films were removed from the silicon wafers and placed between the sample plates for impact analysis. The films were impacted at multiple hole positions and the respective force-time data was recorded. The impact velocity, unless otherwise specified, was measured to be 0.89 m/s.

3.3 RESULTS AND DISCUSSION

3.3.1 Thickness Dependence.

Impact responses of materials are usually dependent on sample thickness and this dependence is not necessarily linear. Therefore, the correlation between measured impact response and thickness was established. Figure 3.2 shows the maximum force and the impact energy as a function of thickness for poly(urethaneurea) films prepared at

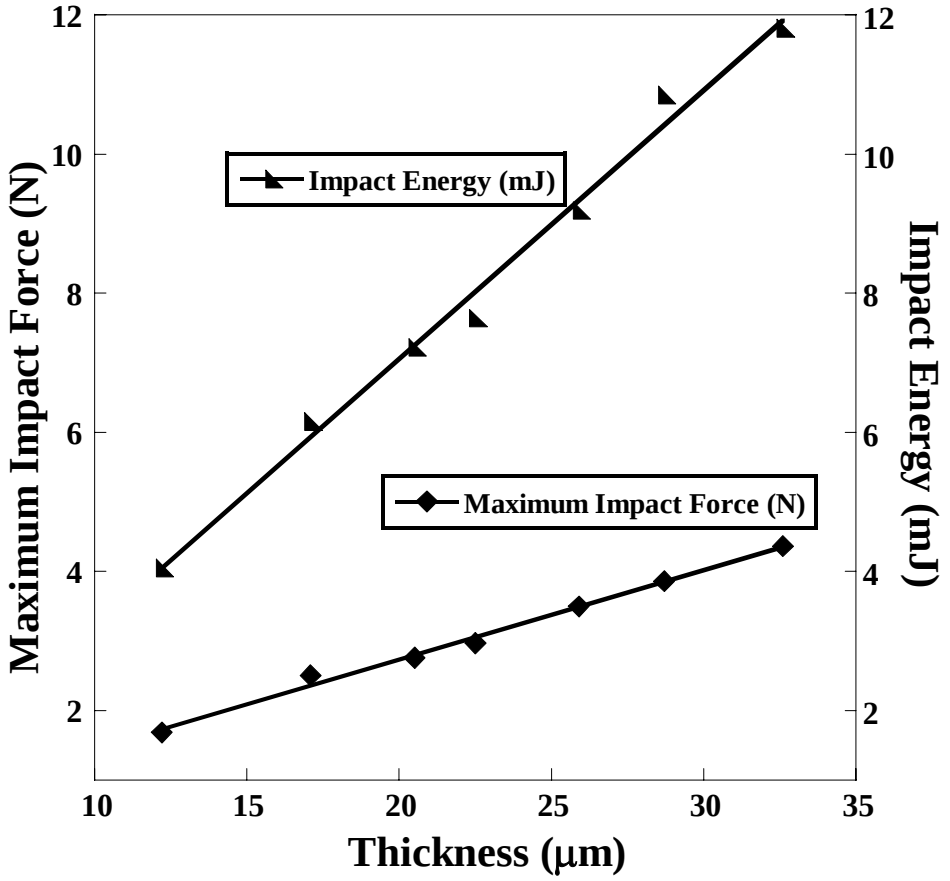

Figure 3.2: Dependence of maximum Impact Force (N) and Impact Energy (J) on film thickness (μm) for poly(urethaneurea) elastomers cured at 95 mole % curative stoichiometry and 80 ^{o}C.

95 % curative stoichiometry and 80 ^{o}C. The data are reported in Table 3.1. The

Table 3.1: Impact data for polyurethaneurea elastomers as a function of thickness, 95 mole % curative stoichiometry, 80 ^{o}C cure temperature, 6 h cure.

Thickness (μm)	Maximum Force (N)	Impact Energy (mJ)	Energy/Thickness (J/m)
12.2	1.68	4.05	330
17.1	2.50	6.15	360
20.5	2.76	7.22	352
22.5	2.97	7.64	339
25.9	3.50	9.19	354
28.7	3.86	10.85	378
32.6	4.36	11.81	362

measurements indicate a linear dependence of impact energy and maximum impact force with thickness, with correlation constants (r^2) of 0.9953 and 0.9967, respectively. The time (or displacement) at failure is independent of thickness. Normalization of impact energy with thickness indicates that all the samples have the same impact energy per thickness, as shown in Table 3.1. The average impact energy per thickness was 177 J/m with a 95 % confidence interval about this mean of 5.72.

Figure 3.3 shows the raw force-deformation profiles used to generate Figure 3.2, indicating a Hookean elastic relationship, $F(t) = Kx(t)$, for the poly(urethaneurea) elastomers over the entire range of measurement. Here, K is initial slope of the force-deflection curve, or "spring constant" that is time and strain-rate dependent. Note also

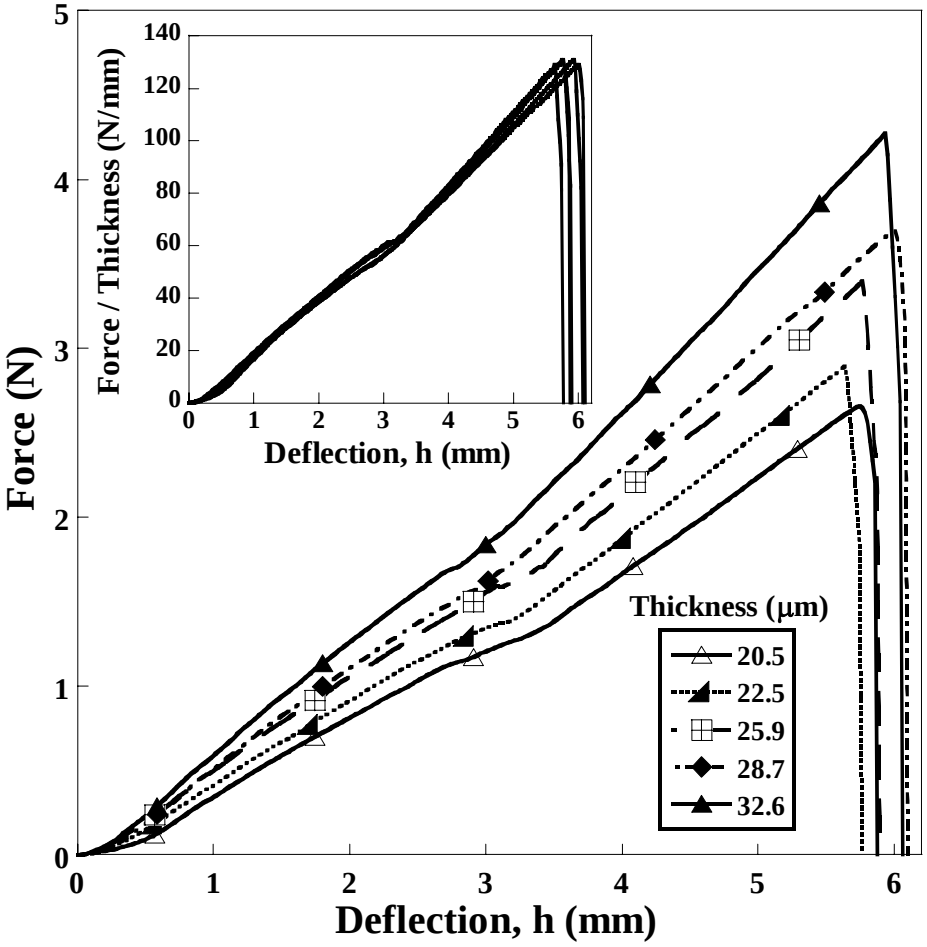

Figure 3.3: Force-deformation curves for poly(urethaneurea) elastomers with different thicknesses cured at 95 % curative stoichiometry and 80 ^{o}C.

that there are slight slope discontinuities and harmonic oscillation artifacts, as discussed above. However, the increase in sample thickness leads to a nearly perfect linear increase in *K*, as shown in Table 2. The dependence of *K* may be understood by modeling the

Table 3.2: Initial Slope, *K* of poly(urethaneurea) as a function of film thickness, 95 mole % curative stoichiometry, 80°C cure temperature, 6h cure.

Sample Thickness(μm)	**"Initial Slope, *K* (N/μm)**
20.5	455.44
22.5	501.13
25.9	557.91
28.7	589.16
32.6	644.96

elastomer as a collection of Voigt (parallel spring and dashpot) elements.[15] The combined viscoelastic response can be computed in a manner analogous to computing the effective capacitance and resistance of a collection of capacitors (energy storage) and resistors (energy dissipation) in an electrical circuit. The effect of increasing the thickness is to add more chains (Voigt elements) in parallel, and the effective initial slope or "spring constant" for a collection of parallel Voigt elements, *K*, is the sum of the individual initial slopes, $K = \Sigma k_i = nk = hk'$. Here, we have made the simplification that the Voigt elements are identical and *n* is the number of elements needed to represent the elastic response at a given thickness, *h* is thickness, and *k'* is an intrinsic material "spring constant" per unit thickness.[15] With this interpretation, *k'* is found to 15.24 N/μm for the data in Table 2, with $r^2 = 0.9883$. Note, however that this "spring constant" is strain-rate

dependent and is only valid at the impact rate of this experiment. Since the elongation at break is constant, the linear dependence of the observed *K* on thickness appears to be responsible for the observed linear dependence of maximum impact force and energy at failure in Figure 3.2.

3.3.2 Validation of Measurement Repeatability and Independence of Test Sites.

Because the sample films are continuous, but are impacted at multiple points, there is a concern that impact at one site will affect measurements at the surrounding sites. Such neighboring impact site interference would be expected to affect severely the reproducibility of results. To investigate interference between neighboring measurements and illustrate the reproducibility of the instrument, force-time curves were obtained by impacting a uniform 25 μm polyethylene film at multiple hole positions. The 25 force-time curves shown in Figure 3.4 indicate the typical reproducibility. The average impact energy and 95% confidence interval are 17.11 $\pm$ 0.36 J/m, and the average maximum impact force and 95% confidence interval are 2.05 ± 0.11 N. These results provide strong indication that uniform pressure was applied on each hole in the sample grid, preventing slippage of the film during impact. We conclude that stress induced in the film at one grid hole did not affect the measurements obtained at neighboring holes, e.g., due to potential stress hardening or plastic deformation that could occur if measurement sites were not isolated.

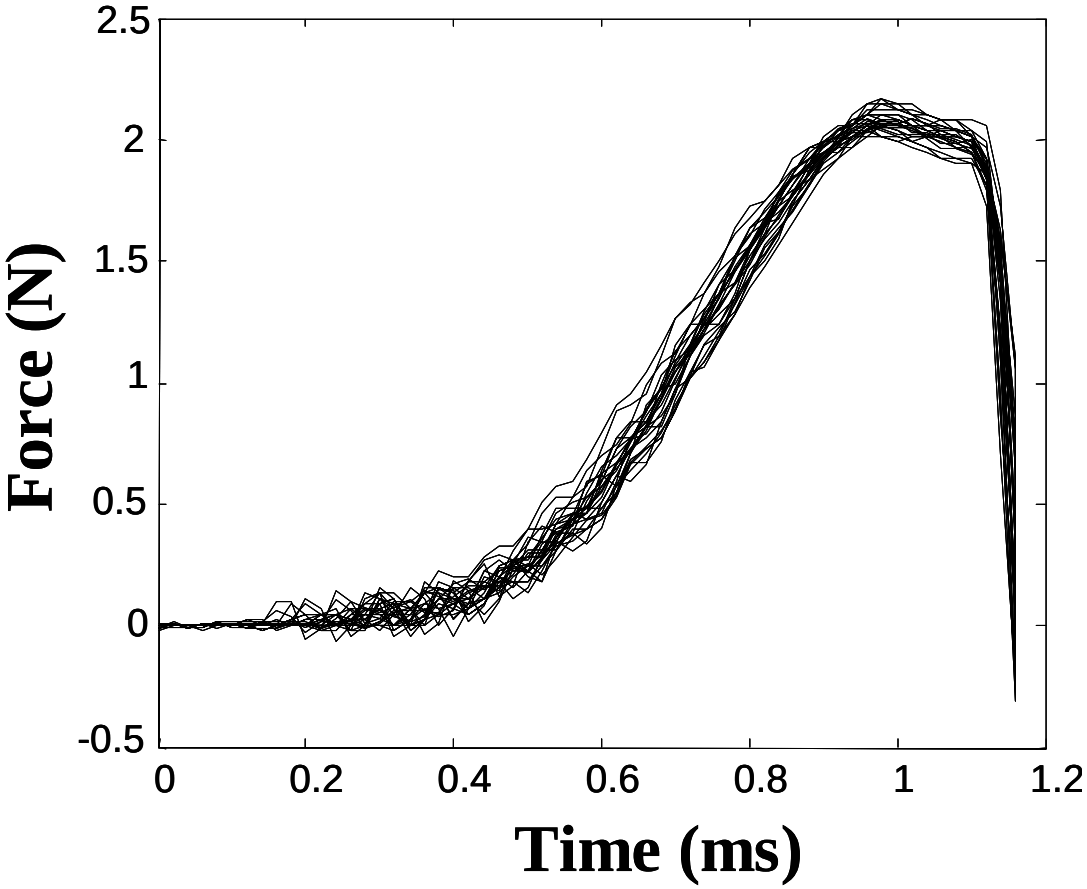

Figure 3.4: Comparison of 25 impact curves from a 5x5 grid of neighboring impact points on a thermoplastic polyethylene 25 μm films.

3.3.3 Sensitivity to Chemistry and Structure

Figure 3.5 shows the sensitivity of the impact test to the chemical and structural differences between thermoplastic versus elastomeric materials. The elastomeric (physically crosslinked) polyurethaneurea shows a linear elastic deformation before brittle failure occurs. On the other hand, the thermoplastic polyethylene appears to undergo an obvious yielding, represented by the maximum in the force profile followed by a period of plastic deformation before failure. Force-deformation curves of this type are typical of those observed for thermoplastics that undergo ductile failure.

Polyurethaneurea elastomers represent an ideal system for characterization of the sensitivity to changes in chemistry and structure within the same class of material. This is because the mechanical properties depend sensitively on the degree of microphase separation and hydrogen bonding, which in turn are controlled by the cure temperature and the concentration of hard (urea) and soft (polyether) segments.[16-18] In Figures 3.6 and 3.7, we show the sensitivity of the impact test to variations in the processing temperature and hard segment concentration (mole % of stoichiometric amount of chain extender) of polyurethaneureas. Changing the ratio of prepolymer to curative can alter the amount of physical cross-linking in poly(urethaneureas). In Figure 3.6, an increase in curative stoichiometry from 85 mole % to 95 % and 150 % leads to a dramatic decrease in the deformation and maximum force at failure. The change in impact response between 85 % to 95 % stoichiometry is probably due to the increased conversion of isocyanate to urea in the 95 % sample. This increased conversion to urea would lead to

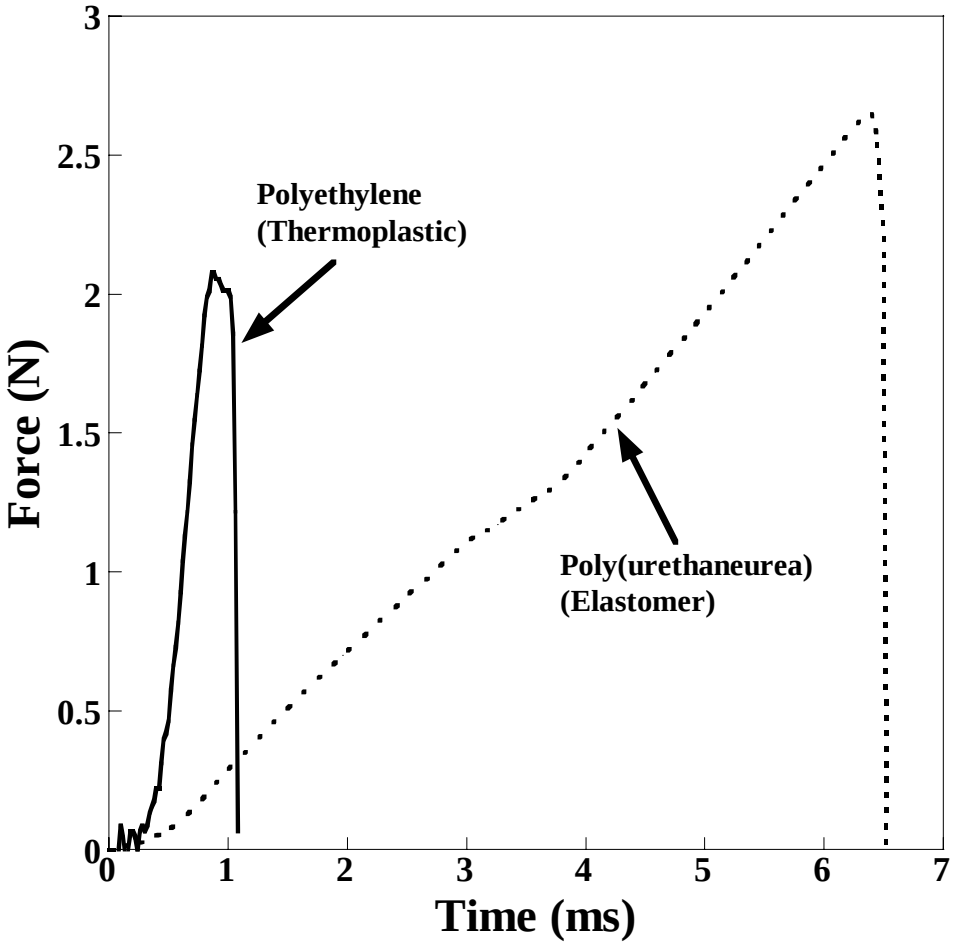

Figure 3.5: Comparison of impact curves for thermoplastic polyethylene vs. elastomeric poly(urethaneurea) cured at 95 % stoichiometry and 80 ^{o}C.

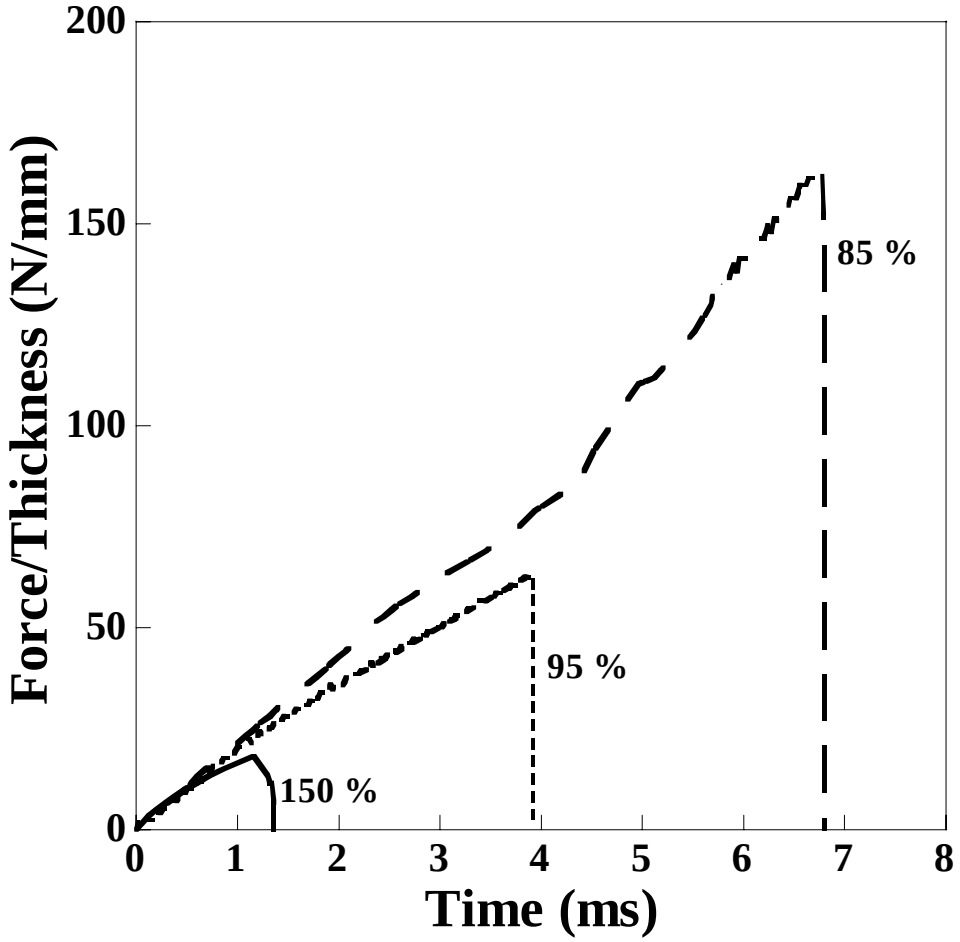

Figure 3.6: Impact curves for poly(urethaneurea) at a series of curative stoichiometries cured at 80 ^{o}C.

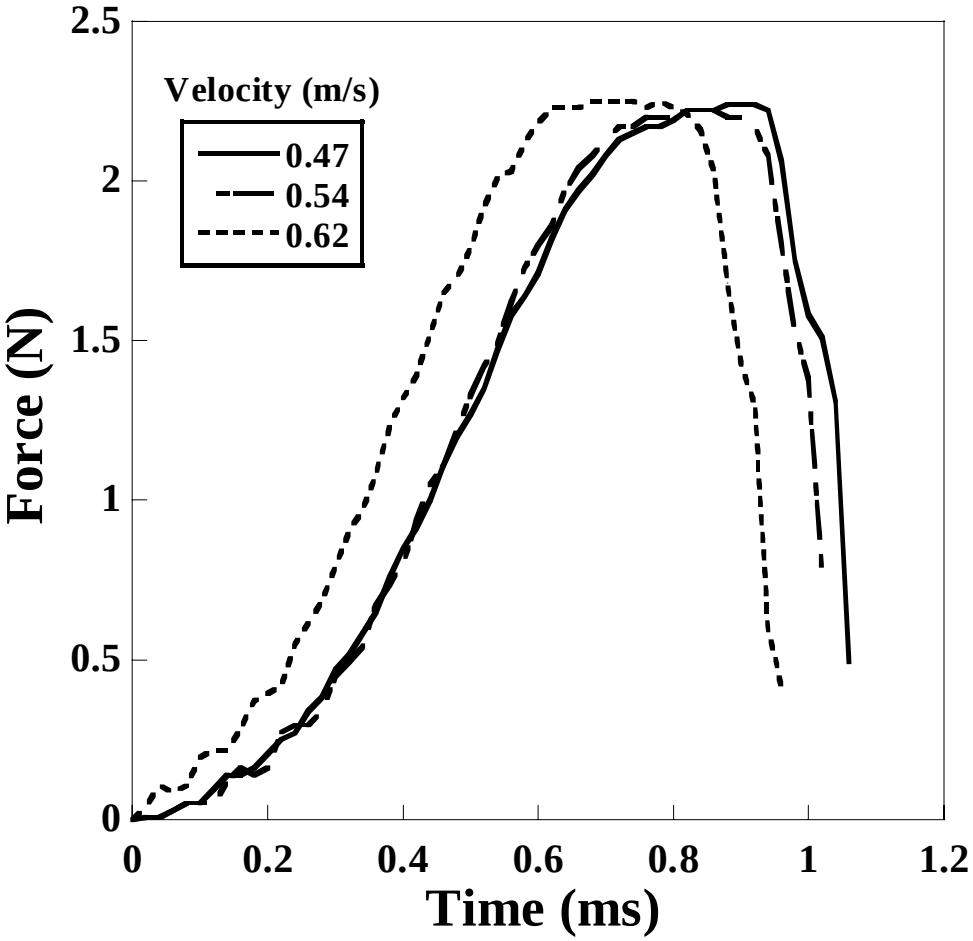

Figure 3.7: Impact curves for poly(urethaneurea) cured at different temperatures for a 95% stoichiometry.

more opportunity for hydrogen bonds to form within the hard urea domains and an increased degree of microphase separation. Hence the 95 % domains may have become more brittle and susceptible to crack propagation than in the 85 % stoichiometry case. Excess curative stoichiometry (150 %) leads to excess unreacted diamine, which may act to decrease the initial slope through plasticization, since a yield point is apparent in the 150 % impact profile. In addition the excess curative may prevent the formation of a continuous network, since diamine curative that is reacted on one end only will not form a complete diurea linkage, weakening the hard domain. Both of these factors (plasticization and incomplete network formation) lead to the dramatically decreased elongation at break observed at 150 % stoichiometry in Figure 3.6. These conclusions are supported by previous X-Ray scattering, DSC, and FTIR spectroscopic studies of the effects of curative composition on hydrogen bonding and hard-domain structure in poly(urethaneureas).[16-18]

In Figure 3.7, an annealing temperature of 90 ^{o}C was observed to give elastomers with a maximum deformation and force per thickness at failure. The primary influence of temperature is to determine the rate of reaction to form urea versus phase separation of hard and soft domains. Since the phase separation is driven primarily by the formation of hydrogen bonds between N-H and urea carbonyls in the hard domains. At low temperatures, there may not be enough thermal energy available to break unfavorable H-bonds, preventing the more favorable hard domain bonds to form. As temperature increases the rate of H-bond formation and breaking can be expected to become similar, allowing the system to equilibrate into a preferred low energy, phase-separated structure.[16] The optimal phase-separated microstructure containing the highest number of

favorable hard-domain hydrogen bonds is expected to yield the most durable materials. At higher temperatures, there may be too much thermal energy, which could break too many H-bonds and prevent the formation of more favorable structures. In addition, chemical crosslinking, e.g., biuret formation, at higher temperatures could "freeze" the elastomer into a more brittle structure.[19] These considerations likely explain the occurrence of an optimum temperature in Figure 3.7. A full proof of these mechanisms, however, will require extensive thermal, spectroscopic, and structural studies that are the subject of current work using combinatorial libraries.

3.3.4 Rate Dependence

Figures 3.8 and 3.9 are included to indicate briefly the ability to measure strain-rate dependent mechanical responses, using the polyethylene films as a model system. In figure 3.9, the area under the curve decreases with increase in strain rate. The areas under the curves of figure 3.9 were calculated to be 1.50 and 1.15 N.sec, corresponding to V =.25 mm/s and V= 1 mm/s. At lower impact velocities, the polymer chains have more time to relax and absorb more energy. This is indicated by the broader width of the impact curve at 0.25 mm/s compared to the curve at 1 mm/s.

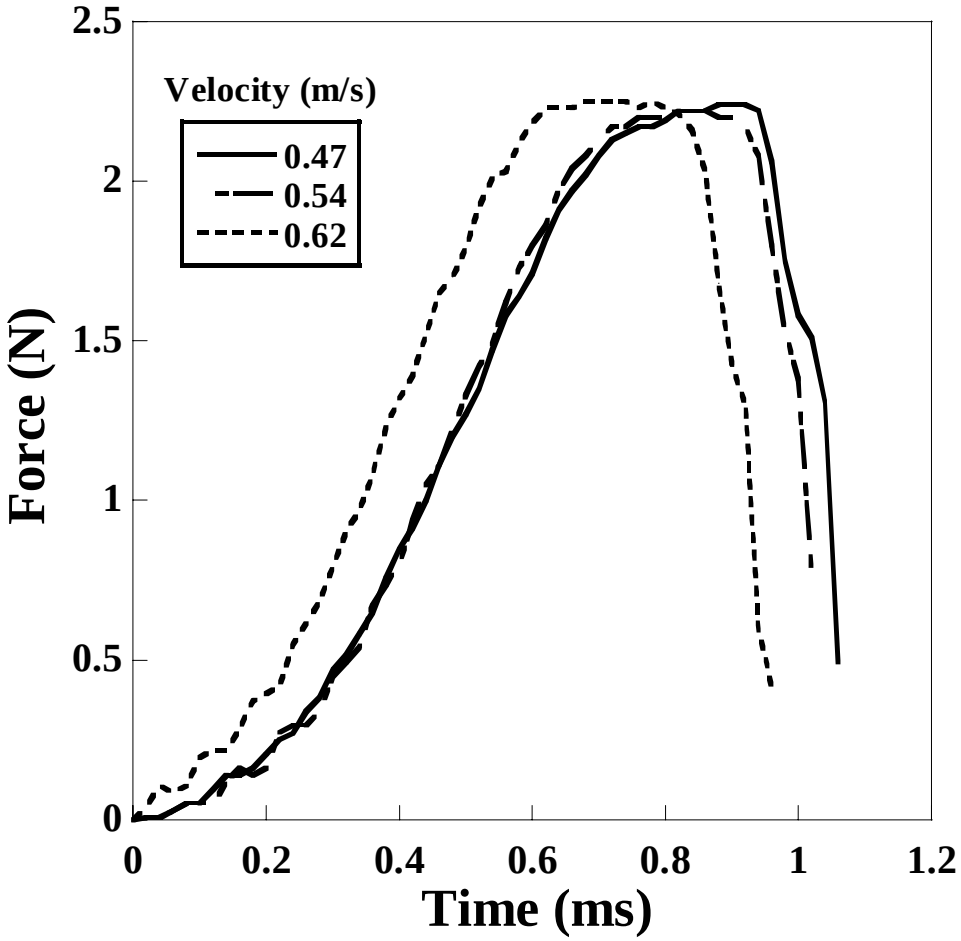

Figure 3.8: Dynamic impact force-time curves for polyethylene film at different strain rates.

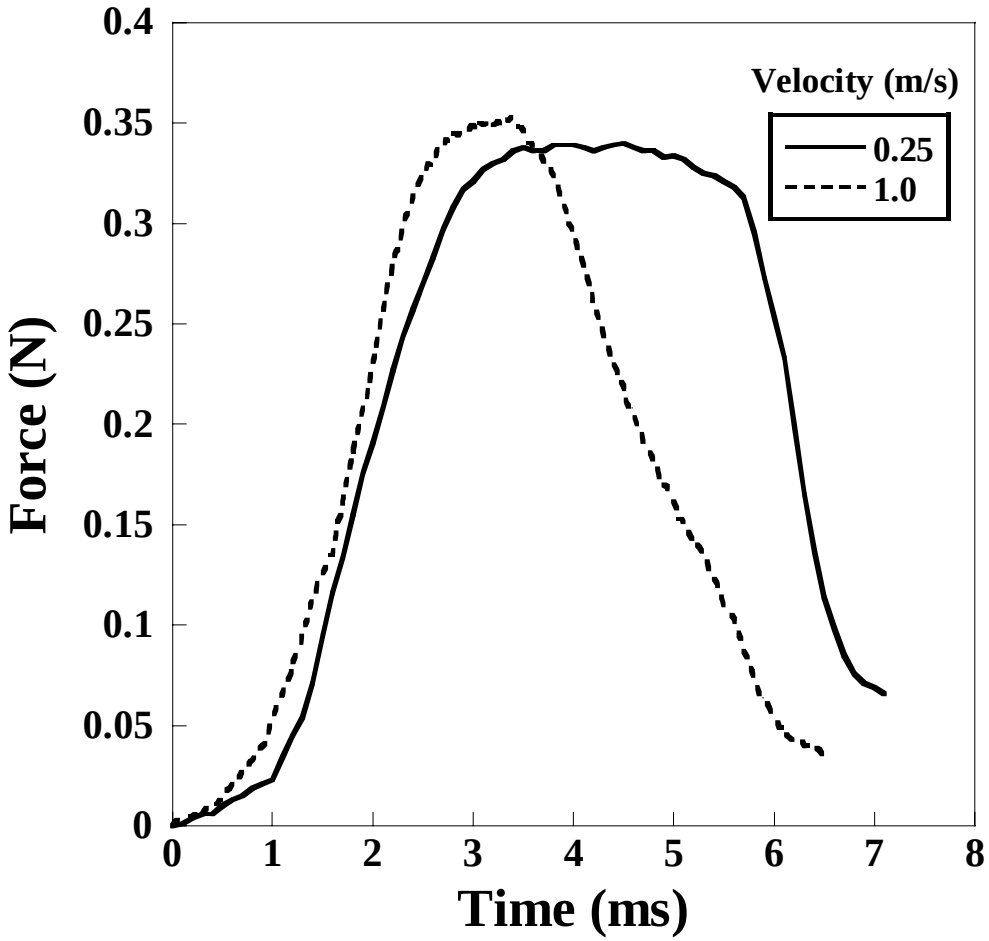

Figure 3.9: Near static force-time curves for polyethylene film at different strain rates.

3.4 CONCLUSIONS

An instrumented falling weight impact apparatus has been designed and constructed for high-throughput characterization of polymer films in the 5 μm to 100 μm thickness range. This instrument is will allow rapid and accurate characterization of the dynamic impact response of multiple positions on combinatorial library films previously developed by the authors.[1-4] We verified the reproducibility and lack of neighbor-neighbor interaction effects for multiple measurements on the same film. In addition, the observed initial slope, maximum impact force and impact energy depend linearly with thickness, as illustrated with a model elastomer. Hence, these properties should be normalized with thickness in order to compare chemistry and structural changes of films at different thicknesses. In contrast, the elongation at failure was found to be thickness independent. Poly(urethaneurea) elastomer impact measurements indicate that the instrument is sensitive to variations in elastomer chemistry and structure. In particular, from force-deformation profiles, the results indicate an optimum curing temperature and the expected trend in mechanical response with respect to polyurethaneurea diamine curative composition.

3.5 REFERENCES

(1) Jandeleit, B., Schaefer, D.J., Powers, T.S., Turner, H.W., Weinberg, W.H., Combinatorial Materials Science and Catalysis. *Agnew. Chem. Int. Ed.* **1999,** 36, 2494.

(2) Meredith, J. C.; Karim, A.; Amis, E. J., High-Throughput Measurement of Polymer Blend Phase Behavior. *Macromolecules* **2000,** 33, (16), 5760.

(3) Meredith, J. C.; Smith, A. P.; Karim, A.; Amis, E. J., Combinatorial Materials Science for Polymer Thin-Film Dewetting. *Macromolecules* **2000,** 33, (26), 9747.

(4) Smith, A. P.; Douglas, J. F.; Meredith, J. C.; Amis, E. J.; Karim, A., Combinatorial Study of Surface Pattern Formation in Thin Block Copolymer Films. *Phys. Rev. Lett.* **2001,** 87, (1), 15503.

(5) Kakarala, S. N., Rochem, J. L, In: Kessler, S. L., Adams, G. C., Driscoll, S. B ., Ireland, D. R., *Instrumented Impact Testing of Plastics and Composite Materials, ASTM STP 936,* **1987** American Society of Testing and Materials, Philadelphia, p 24.

(6) Hemingway, A. J., Channell, A.D., Clutton, E.Q, Instrumented Charpy Impact Testing of Polyethylene. *Plastics, Rubber and Composites Processing and Applications* **1992,** 17, 147.

(7) Bucknall, C. B., The Relevance of Impact Testing in the Materials Science of Polymers. *Plastics, Rubber and Composites Processing and Applications* **1992,** 17, 141.

(8) Brown, R. P., *Handbook of Plastics Test Methods*. George Goodwin Limited in association with the Plastics and Rubber Institute: London, **1981**.

(9) Jones, D. P., Leach, D.C., Moore, D.R, The Application of Instrumented Falling Weight Impact Techniques to the Study of Toughness in Thermoplastics. *Plastics, Rubber and Composites Processing and Applications* **1986,** 6, 67.

(10) Ireland, D. R., Procedures and Problems Associated with Reliable Control of the Instrumented Impact Test. In *Instrumented Impact Testing, ASTM STP 563*, American Society for Testing and Materials: Philadelphia, **1974**; pp 3.

(11) Toropov, A. I., Grosso, M., Dynamic Calibration of Impact Test Instruments. *J. Testing and Evaluation, JTEVA* **1998,** 26, (4), 315.

(12) Standard Test Method for High Speed Puncture Properties of Plastics Using Load and Displacement Sensors. In *Annual Book of ASTM Standards*, American Society For Testing and Materials: Philadelphia, **1999**; Designation: D 3763.

(13) Reed, P. E., Falling Weight Impact Testing and Design. *Plastics, Rubber and Composites Processing and Applications* **1992,** 17, 157.

(14) Velasco, J. I., Martinez, A.B., Application of Instrumented Falling Dart Impact to the Mechanical Characterization of Thermoplastic Foams. *J. Materials Science* **1999,** 34, 431.

(15) Ferry, J. D., *Viscoelastic Properties of Polymers*. John Wiley & Sons: New York, **1980**.

(16) Oertel, G., *Polyurethane Handbook*. 2 ed.; Hasner Gardner Publications, Inc.: Cincinnati, **1993**.

(17) Beck, R. A.; Truss, R. W., The Effect of Stoichiometry on Fracture Toughness of a Polyurethane-urea Elastomer. *Polymer* **1999,** 40, 307.

(18) Wang, C. B.; Cooper, S. L., Morphology and Properties of Segmented Polyether Polyurethaneureas. *Macromolecules* **1983,** 16, 775.

(19) Petrovic, Z. S.; Javni, I.; Banhegyi, G., Mechanical and Dielectric Properties of Segmented Polyurethane Elastomer Containing Chemical Crosslinks in the Hard Segments. *J. Polym. Sci., Part B: Polym. Phys.* **1998,** 36, 237.

CHAPTER 4

HIGH-THROUGHPUT DISCOVERY OF STRUCTURE-MECHANICAL PROPERTY RELATIONSHIPS FOR SEGMENTED POLY(URETHANE-UREA)S

A novel high-throughput method was used to determine the effect of chain extender composition on the mechanical properties of segmented polyurethaneureas. Combinatorial libraries with continuous gradients in chain extender composition ($60 < \phi < 160$ mole % stoichiometry), cure temperature ($70 < T < 110$ ºC), or both, were synthesized. Stress versus strain data were obtained at numerous library positions (corresponding to different ϕ and T values) using a unique high-throughput mechanical characterization (*HTMECH*) apparatus developed by the authors. These mechanical measurements were related to the morphology, hydrogen bonding, and degree of phase separation using AFM, FTIR and DSC. Optimum strength and % elongation were observed at a chain extender composition of $\phi = 85$ mole %, corresponding also with the finest phase-separated morphology, indicated by an even dispersion of uniform hard domains (dimensions 110 - 130 nm). DSC measurements indicated increased mixing of soft and hard segments when ϕ exceeded 85 %, which was correlated to decreased urea-urea hydrogen bonding (from FTIR). SEM analysis of the library fracture surfaces

suggested a transition from brittle to ductile failure with increased ϕ, in agreement with the increased soft-hard segment mixing and disruption of the hydrogen-bonded network. These results validate the *HTMECH* approach as an accurate and effective screening tool for developing structure-mechanical property relationships in combinatorial polymer libraries.

4.1 INTRODUCTION

The successful application of combinatorial and high-throughput methods (CHM) in the pharmaceutical industry has made these techniques very attractive to materials researchers. Compared to conventional 1-sample-1-measurement techniques, CHM provides a cost and time-saving alternative, especially during the discovery stages of a materials research endeavor. In polymer materials research, the purpose of CHM is not to replace established measurement techniques, but rather to enhance the use of detailed measurement techniques by providing an efficient screening to select the most relevant regimes of parameter space to explore. This is accomplished by exploring a large variable space with high-throughput screens of desired properties on a single library, reducing variance and the likelihood of overlooking unexpected behavior.

In order to apply CHM to polymer research, methods have been developed for preparing high-throughput polymer libraries with continuous gradients in composition, thickness, surface energy, and annealing temperature (T).[1-5] These libraries have been used to characterize polymer blend phase separation,[1] thin-film dewetting,[2,6] block copolymer surface pattern formation,[7] crystallization growth rate,[5] cell adhesion and

function on polymer surfaces,[8] and mechanical properties of polymer films.[9-11] In addition, discrete sample libraries that explore variations in composition and chemical structure have been developed.[12-14] With numerous library preparation techniques available (gradient and discrete), the limitation in polymer CHM appears to be in the screening and characterization stage. There is a strong need to extend the suite of high-throughput screens available for polymers. For example, polymeric materials are especially sensitive to processing variables such as temperature and rheological history, which strongly affect the nano- and microstructures. These microstructures have a tremendous effect on mechanical, thermal, optical, and permeability properties. Polyurethanes and polyurethaneureas are good examples of this sensitive relationship between processing, structure, and mechanical properties.

Segmented polyurethaneureas are elastomers that belong to the group of materials generally referred to as "polyurethanes". Compared to traditional polyurethanes, segmented polyurethaneureas have superior elasticity and strength[15] due to improved phase segregation and a three-dimensional bidentate urea-urea hydrogen-bonding network found in the hard domain.[16,17] Due to the myriad block chemistries and microstructures possible, SPUU elastomers have a wide range of applications, including biomaterials, textiles, foams, coatings, adhesives and other consumer products. Despite the industrial importance of SPUUs, there is still limited literature addressing the effect of chain extender stoichiometry on mechanical properties of polyurethaneureas,[18] in particular in combination with varying the cure *T*. One problem is the large number of combinations of soft and hard segment chemistry, isocyanate chemistry, chain extender composition, and cure *T* values. Large numbers of combinations are difficult to screen

with conventional sample preparation techniques, particularly given the sensitivity of isocyanates to water contamination and small errors in the mixing of compositions.

To understand this complexity, consider that the mechanical properties of SPUUs are dependent on the degree of phase separation between hard and soft segments. Generally, a finer morphology results in higher elongation at break and tensile strength.[16] The degree of phase-separation in polyurethanes is dependent primarily on cure temperature and chain extender composition, and has been monitored using FTIR, DSC, X-ray diffraction and AFM.[15-17,19-26] Although the literature is limited for SPUUs, extensive investigation of polyurethanes has shown that the morphology and mechanical properties are affected strongly by the molar ratio of isocyanate to chain extender,[27-36] insight which is expected to apply to SPUUs as well.[37] Changing the ratio of isocyanate to chain extender can alter the amount of hydrogen bonding by causing a relative excess or depletion of N-H hydrogen donors.[18] A stoichiometric excess of isocyanate or the use of tri- or higher functional chain extenders can lead to biuret (urea groups) and allophanate (urethane groups) chemical crosslinks.

To address the need for high-throughput screens capable of determining such processing-structure-mechanical property relationships, we reported previously a new apparatus for high-throughput mechanical characterization (*HTMECH*) of polymer libraries.[9] We applied *HTMECH* to characterize structure-property relationships in polyurethaneurea *T*-gradient libraries.[10] In the present paper, we use *HTMECH* to develop structure-property relationships for segmented polyurethaneurea (SPUU) libraries with a *gradient in chain extender composition (ϕ)*. There are several key questions we seek to answer in this study. First, we desire to demonstrate that the

combinatorial library synthesis technique mentioned above can be used to *synthesize polymers* (in this case *a block copolymer*) in situ on ϕ-gradient libraries. Previously, these libraries were used only to blend polymers and other additives. Below, we describe the preparation of ϕ-gradient combinatorial SPUU library films, which are subsequently annealed over an orthogonal *T*-gradient to examine the combined effects of varying *both the curing T and chain extender composition*. The libraries are characterized (screened) with high-throughput spectroscopic, microscopic and mechanical measurements at points representing different chain extender ϕ and cure *T*. Second, we seek to discover if relatively simple spectroscopic screens, e.g., FTIR, can be used to indicate structures that predict optimal mechanical properties. Stress-strain profiles are related to the materials microstructure using FTIR, AFM and DSC, and we show that the urea-urea H-bonding fraction determined from FTIR is a good predictor of trends observed with tensile strength. Finally, we will present a rigorous comparison between *HTMECH* and conventional uniaxial tensile tests to determine the reliability of *HTMECH* relative to existing methods for mechanical measurements.

4.2 EXPERIMENTAL SECTION

4.2.1 Materials and Library Synthesis

Segmented polyurethaneurea libraries were synthesized by first preparing two solutions: (1) toluene diisocyanate(tetramethylene glycol) prepolymer (Air Products and Chemicals, AIRTHANE® PET-85A, M_W =2500, NCO functionality = 2.0, mass % NCO = 3.3 %) and (2) trimethylene glycol di-*p*-aminobenzene chain extender (Air Products and Chemicals, VERSALINK® 740-M), to a total concentration of 30 mass % in

tetrahydrofuran (VWR, ACS Grade). A composition-gradient film library was prepared by using a technique described in detail elsewhere.[1,38,39] A clean vial was initially loaded with 1 cm^3 of the prepolymer and chain extender solutions mixed at 60 mole % of the stoichiometric amount of chain extender. The solution was stirred vigorously and the infusion pump, the withdrawal pump and the automated sample syringe were activated simultaneously to: (1) infuse 0.203 cm^3 of the 30 % by mass chain extender solution into the vial at 0.135 cm^3/min, (2) withdraw 0.4 cm^3 of the solution from the vial at 0.3 cm^3/min, and (3) extract continuously the mixed solution in the vial. After a sampling period of 40 seconds, the sampling syringe contained 70 μL of solution with a linear gradient in chain extender stoichiometric amount (60 to 157 mole %) along the length of the syringe needle. Although gradient library films were prepared from 60 to 157 mole % curative, the characterization was performed over a narrower range, 80 to 150 %, to avoid the edges that might contain residual stresses or other artifacts. The content of the syringe needle was deposited as a 25 mm long stripe on a silicon wafer (Silicon Inc.) within 16 seconds. The gradient stripe was placed quickly under a 40 mm wide stationary knife edge (350 μm above the substrate at a 5^o angle), and was coated quickly as a film for a distance of 30 mm by moving the substrate under the blade at 25 mm/s, orthogonal to the composition gradient direction. Multiple composition gradient films were prepared in the same manner with thicknesses between 20 μm and 35 μm. The library was cured by placing a composition gradient film on a linear temperature gradient stage,[1,38,39] under -1 atm vacuum, for 6 h. The lower and upper endpoint temperatures of the heating stage were set to 75 ^oC and 110 ^oC respectively. Some of the composition gradient libraries were cured at a uniform temperature (90 ^oC) in a vacuum oven for 6 h.

4.2.2 Characterization

Spectroscopy. The thickness at different positions on the films, corresponding to different combinations of chain extender stoichiometry and cure temperature, was measured by visible-near infrared interferometry (Stellar Net EPP 2000). Interferograms collected from wavelengths of 400 nm to 900 nm were fitted numerically to a thin film optics model using Film Wizard software (SCI). Refractive index and optical adsorption were measured as a function of wavelength with variable-angle spectroscopic ellipsometry (V-VASE, J.A. Woollam Co). FT-IR absorption spectra were recorded at room temperature and a resolution of 4 cm^{-1} using a Bruker IRscope II connected to a Bruker IFS 66/V spectrometer. The IR microscope was equipped with an *x-y* translation stage which facilitates rapid screening of the polymer libraries. The sample area was purged with dry air to prevent the appearance of atmospheric water bands in the spectra. The polyurethaneurea films were mounted on a sapphire substrate, and spectra were recorded at different positions on the gradient film libraries. The spectra were corrected for thickness differences and a peak separation and analysis software package (Peakfit® 4.11, Jandel Scientific) was used to resolve the bands in the carbonyl region (ν = 1630-1740 cm^{-1}) to obtain the relative ratios of the peak areas, assuming Gaussian peak shapes.

Microscopy. AFM images of the films were taken in the non-contact (tapping) mode at different positions using a Thermomicroscopes® SPM Explorer. An *x-y* translation stage was attached to the microscope, which allows relatively high-throughput screening of the libraries. The images were acquired under ambient conditions with SFM (Thermomicroscopes # 1650) silicon probes, having a resonant frequency of 292-331 Hz and a spring constant of 24-41 N/m. The length, width and thickness of the probe are

126 μm, 27-28 μm and 10-15 μm respectively. The setpoint amplitude used in feedback control was adjusted to 50-70% of the tip's free amplitude of oscillation. The AFM was operated on a vibration isolation table.

Mechanical Tests. Libraries were deformed at various T, ϕ positions using the *HTMECH* apparatus, shown schematically in Figure 4.1. Details on the development of this apparatus can be found elsewhere.[9,10] These previous papers also discuss experiments that illustrate the excellent reproducibility of force versus deformation data and mechanical parameters extracted from this data. Generally there is less than a 5 % variability in forces between various points measured on a uniform composition library. Also, no artificial correlations have been observed for neighboring measurements on the library. Stress versus strain profiles were obtained at two strain rates: an impact rate of 0.9 m/s and a slow rate of 30 mm/min (0.5 mm/s). All mechanical tests were performed under ambient conditions. After indentation, the films were coated with a thin layer of gold and SEM images of the fracture surfaces were taken using a Hitachi 3500H SEM. In order to compare mechanical measurements from *HTMECH* (radial geometry) to the conventional uniaxial tensile tests, five samples of uniform chain extender composition of 85, 100, 116, 132 and 150 mole % were cured in a vacuum oven at 90 ^{o}C for 6h. These samples were characterized mechanically using both the *HTMECH* apparatus and a commercial uniaxial tensile apparatus (Instron 5842) at a strain rate of 30 mm/min. DSC measurements of these uniform samples were carried out on a Seiko DSC220C differential scanning calorimeter over the temperature range of -90 ^{o}C to 90 ^{o}C, at a heating rate of 5 ^{o}C/min. The degree of chemical crosslinking was estimated by placing

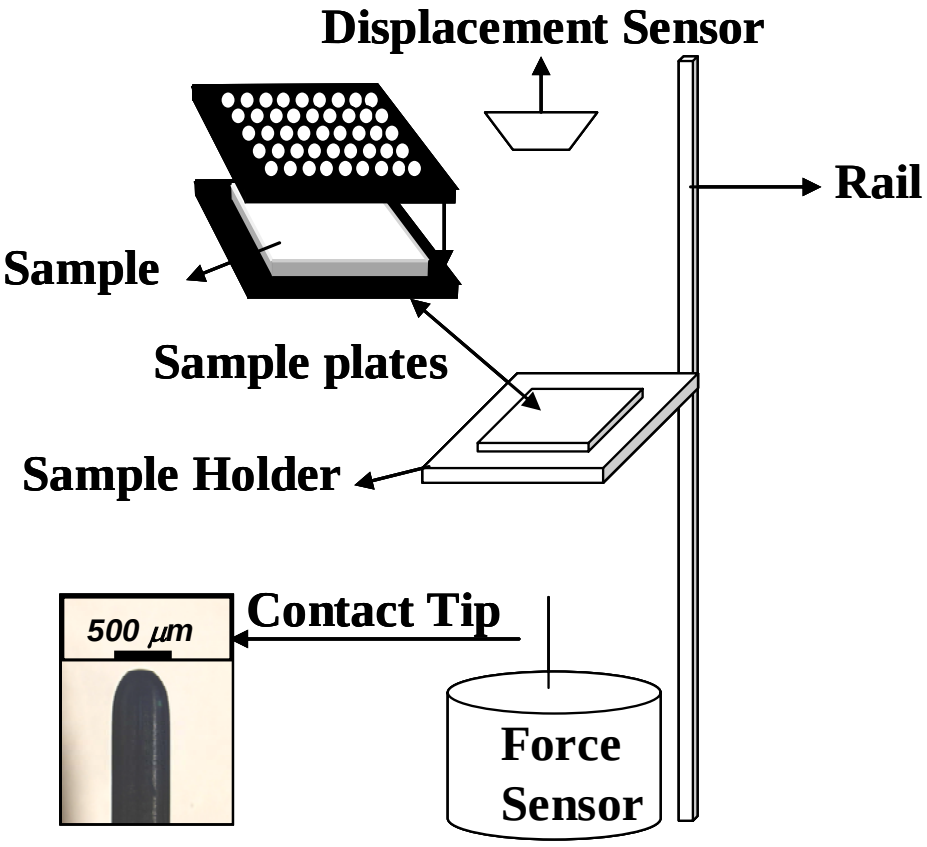

Figure 4.1: Schematic representation of the high-throughput mechanical characterization apparatus.

30 mg to 50 mg of the five samples in separate glass vials containing 5 cm^3 N-N-dimethyl-formamide (DMF) for a week, followed by gravimetric determination of the nonsoluble fraction.

Figure 4.2 shows a cross-section of the deformation geometry in the *HTMECH* apparatus. The load on the needle, e.g., the force that is measured, F_Z, is the vertical component of the actual in-plane radial tensile force (F_r) developed in the film. In Fig 4.2, the film profile is represented in two ways: (1) the actual profile that can have some degree of nonlinearity and (2) a linear approximation or conical film profile shape. The geometrical parameters include d, the indentation distance; r, the radial position measured from the center of the needle, $w(r)$, the film profile shape; R, the needle radius (R = 500 μm); l, the extended length of the film in the linear approximation; r_0, the hole radius (r_0 = 3 mm), and θ, the tangent angle between the film and the needle at their point of contact, $r = c$.

Green and Adkins[40] presented the general theory of large deformations of elastic membranes: thin materials that do not exhibit bending stresses (normal to plane of material) under a load. Thin elastomeric polymers are thought to come close to the ideal membrane model, where all of the stress is distributed in the plane of the material, with both radial and tangential components, $\sigma_r(r)$ and $\sigma_t(r)$. The deformation of axisymmetric membranes (Fig. 4.2) is treated by Yang and Feng,[42] who presented a numerical solution of the geometry employed in this work, namely a circular membrane deformed by a spherical tip, shown recently to correlate well with experimental measurements.[44] It is important to emphasize that experimental conditions only approximate equilibrium in the case of slow strain rates, whereas large strain rates are likely to be far from equilibrium.

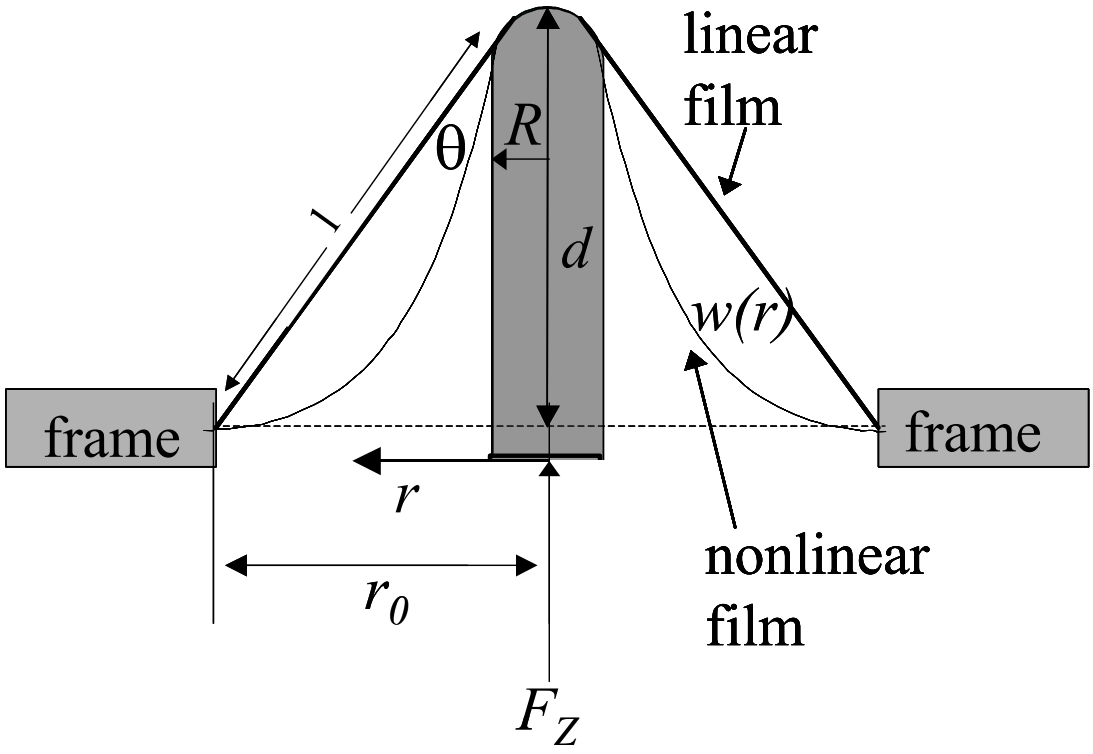

Figure 4.2: Schematic representation of film deformation geometry.

Nevertheless, an examination of membrane theory sheds important physical insights onto the *HTMECH* apparatus design and interpretation of results.

To understand the measurement geometry employed in this work, it is desirable to know how the film profile, $w(r)$, and stresses, $\sigma_r(r)$ and $\sigma_t(r)$, depend upon the load, F_Z, sample geometry, and material properties. In the absence of significant flexural rigidity, Eq. 4.1 and 4.2 describe the relationship between these parameters and must generally be solved numerically or through infinite series.

$$\sigma_r \frac{dw}{dr} = \frac{rF_Z}{2} \tag{4.1}$$

$$\frac{d}{dr}(\nabla^2 f) + \frac{Eh}{2r}\left(\frac{dw}{dr}\right)^2 = 0 \tag{4.2}$$

In the expressions above, $f(r)$ is the stress function, from which $\sigma_r = (1/r)(df/dr)$ and $\sigma_t = d^2f/dr^2$. Wan and Liao[43] presented an analytical solution in two limiting cases that are particularly relevant to the geometry employed here. The film profile is divided into a contact region (where tip contacts film) and a noncontact region (extending from contact radius, $r = c$, to the mounting edge, $r = r_0$). In the contact region, the solution is simplified because the film profile is constrained to follow the tip shape. To obtain an analytical solution in the non-contact region, the authors adopted two different assumptions about the film profile and stress distribution. In the conical approximation, it is assumed that the film profile is a simple linear function (see Fig. 4.2). In the uniform stress assumption, the stress is assumed to be distributed uniformly throughout the non-contact region, e.g., $f \neq f(r)$. It turns out that these two solutions offer approximate

maximum and minimum bounds on what is observed experimentally. In addition, their solutions predict the dependence of load, F_Z, versus indentation, d, as a function of the ratio of the tip radius to the hole radius, R/r_0. Of particular interest is that both approximations predict that as $R/r_0 \rightarrow 0$ (the point-load limit) the load scales with indentation as, $F_Z \sim d^n = d^3$, which is a common characteristic of thin films.[43] As $R/r_0 \rightarrow 1$, n becomes larger than 3.

The models above assume purely elastic materials with no bending (z-component of film stress). In reality one wishes to understand how the onset of plastic deformation or presence of bending might affect the load-indentation data. The experiments of Wan and Liao[43] indicate that when plastic yielding does occur, it begins at the contact point between tip and film, $r = c$, and decreases as $r \rightarrow r_0$, with a maximum at c. The conical profile assumption (non-constant stress function) predicts that to keep the sample from yielding, $R \geq 9F_Z/(2\pi h\sigma_y)$, where σ_y is the yield stress. Thus, for a constant yield strength, the onset of plastic deformation will be enhanced by smaller tip radius, larger loads, and thinner films. To avoid plastic yielding, which is not a design necessity of ours, the yield stress must stay above $\sigma_y = 95F_Z$ (MPa), corresponding to a maximum of 430 MPa at our highest observed loads. SPUUs generally stay outside of this σ_y range due to their highly elastomeric nature. However, deviations from elastomeric behavior are observed for some library compositions in which the elastomeric network is compromised. In these cases, plastic yielding can occur if σ_y becomes significantly small, which actually is a convenient indicator of elastomer network quality. In addition, their experiments discuss the influence of tip radius on the stretching versus bending behavior of real films that have a nonzero bending component. There is a corresponding

maximum tip radius, R, for the film to undergo pure stretching. Our apparatus has R/r_0 = 0.5/3.0 = 1/6, and to avoid bending stresses our tip radius, R = 0.5 mm, is always well-below the maximum $R = 400F_Z$ (mm), where F_Z is the load in N. To calculate this parameter, we estimate the flexural rigidity of common polyurethanereas as $D = E_Y h^3/12(1-\nu^2) \approx 10^{-8}$ J, where E_Y (elastic modulus at 100% strain) ≈ 3 MPa, and ν (Poisson's Ratio) = 0.5.[43] For films that have significant flexural rigidity, or large thickness, the gradient of F_Z versus d is predicted to fall below n = 3, with n = 1 at pure bending.

A primary objective of this work is to compare results for mechanical measurements from both uniaxial and biaxial instruments, rather than to make detailed comparisons to theory. Hence, we choose operational definitions of stress and strain that allow a meaningful comparison to the uniaxial data. The raw force versus time data was converted to an "operational" stress (σ) by dividing force by the area around the hole perimeter where the film is held: area = $2\pi r_0 h$, where h is the initial film thickness. For simplicity, we assume a linear profile, and note that in most cases the film profile conformed closely to a conical geometry. The engineering strain (ε) was obtained by dividing the instantaneous linear radial deformation, $l = l(t)$, by the initial hole radius, r_0. The radial deformation was obtained by first converting time (t) into vertical needle indentation, $d = v_0 t$, where the strain rate v_0 changes by less than 1 % during impact.[9, 10] The linear deformation is found as the hypotenuse between the fixed hole radius, r_0, and d: $l = (d^2 + r_0^2)^{1/2}$.[10] The radial component of the force is obtained from trigonometry as $F_R = F_Z / \cos(\theta)$, where $\cos(\theta) = d/(d^2 + r_0^2)^{1/2}$ (Fig 4.2). Measurement of the radial force from the measured vertical force can lead to problems at low elongation, where the

needle becomes nearly perpendicular to the film and $\cos(\theta) \approx 0$, but this is confined to the first 10 to 20 % of strain. In addition, when the actual film profile deviates significantly from linear, the true θ value will be less than the linear approximation, leading to an overestimation of σ and underestimation of ε. Fortunately, these errors will cancel in the calculation of an "*effective" secant* modulus: $E = d\sigma / d\varepsilon = [F_Z * (d^2 + r_0^2)^{1/2} / (d2\pi r_0 h)] / [(d^2 + r_0^2)^{1/2} / r_0] = [F_Z / 2\pi dh]$. The $[(d^2 + r_0^2)^{1/2}]$ term indicating the instantaneous deformed film radius cancels in the modulus determination, and this operational modulus ($d\sigma / d\varepsilon$) from the uniaxial and *HTMECH* (radial) instruments should be identical barring any other artifacts. We note that the secant modulus is not Young's modulus.

Differences in mechanical response in uniaxial versus radial strain may occur due to geometry-dependent stress nonlinearity and nonaffine deformation in elastomer networks. Radial deformation is a special case (the equibiaxial strain case) of the more general biaxial deformation. Recent studies on crosslinked and entangled PDMS elastomers show that biaxial deformations are more sensitive to these nonlinear and nonaffine effects than uniaxial strains.[45] First of all, it is well-known that affine elastomer deformations exhibit significant nonlinear stress versus strain profiles, even when single chains are assumed to be linearly elastic (Gaussian). In an affine deformation, network connection sites are displaced homogeneously in proportion to the bulk sample dimensions. At moderate strains, network connectivity allows heterogeneous rearrangements that can reduce the stored stress below what would be predicted for an affine deformation. As a result, elastomers show nonaffine deformations whose magnitude is dependent on the loading geometry. We can expect differences in the modulus between the uniaxial (1 loaded dimension) and radial (2 loaded dimensions)

test geometries to arise due to the nonlinear stress response and the nonaffine deformations. In addition, the strain-induced crystallization common for SPUU elastomers (usually at strains exceeding ≈ 300 %) is also dependent on the strain geometry. These predictions will be examined below in a comparison of results from the radial *HTMECH* apparatus versus conventional uniaxial deformation.

One may also be concerned with the effect of the composition gradient on the measured properties. We have compared gradient library results to results from uniform films for the compositions explored here, and have found no significant deviations in the trends observed. To our knowledge no theory has been developed that predicts the effect of a gradient in modulus, for example, on the deformation. Such a development would be beyond the scope of the present paper. In other high-throughput measurements, e.g., microscopy, it was noted that the steepness of the gradient plays a critical role in determining if the gradient artificially influences results.[7] Intuition leads one to suspect that an asymmetrical film profile would result and the force on one side of the needle would be less than the other. If the gradient were significantly steep, this could lead to bending of the needle, an artifact that was not observed in our experiments.

4.3 RESULTS AND DISCUSSION

The chain extender composition at different positions on the composition gradient library was calculated using the mass balance equation developed elsewhere.[1] These predicted compositions (based upon coating conditions) agree very well with data obtained from FTIR (see Fig. 4.3) using a calibration curve (not shown) of known chain extender compositions based upon the absorption area of two carbonyl peaks centered

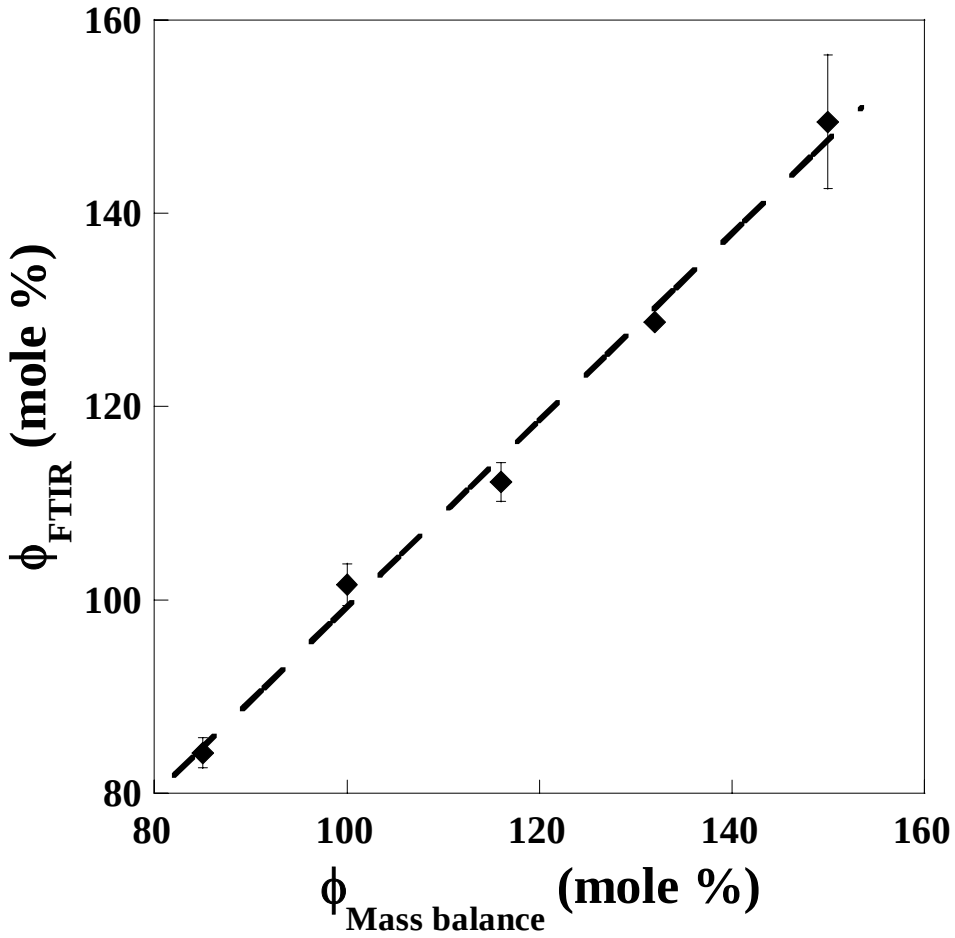

Figure 4.3: Verification of chain extender composition in gradient library using FTIR.

around 1707 and 1730 cm^{-1}. This check indicates the degree of control over composition that is typical of the ϕ-gradient coating procedure. Twenty-five FTIR spectra were taken from a 2D *T*, ϕ- gradient library, corresponding to different combinations of cure *T* and chain extender composition ϕ. The fraction of total urethane, urea-urea, and total urea hydrogen bonding was estimated using appropriate ratios of H-bonded and free carbonyl peaks, as reported by others.[24] Particularly important in determining mechanical properties is the bidentate urea-urea hydrogen bonding, which is believed to form a three-dimensional network that improves hard and soft phase segregation relative to non-urea polyurethanes.[16, 17]

Figure 4.4 shows FTIR spectra in the N-H stretch region taken at different ϕ positions on a ϕ-gradient library cured at 90 ^{o}C. The two peaks in the spectra are identified as free N-H (ν = 3363 cm^{-1}) and hydrogen bonded N-H (ν = 3292 cm^{-1}). There is a relative increase in the free N-H absorption with increasing ϕ, shown by a calculation of the peak areas. This relative increase in free N-H absorption occurs due to excess chain extender for which hydrogen bond acceptors become increasingly scarce at chain extender stoichiometry above 100 mole %. This excess free N-H becomes important later in interpreting mechanical and structural measurements.

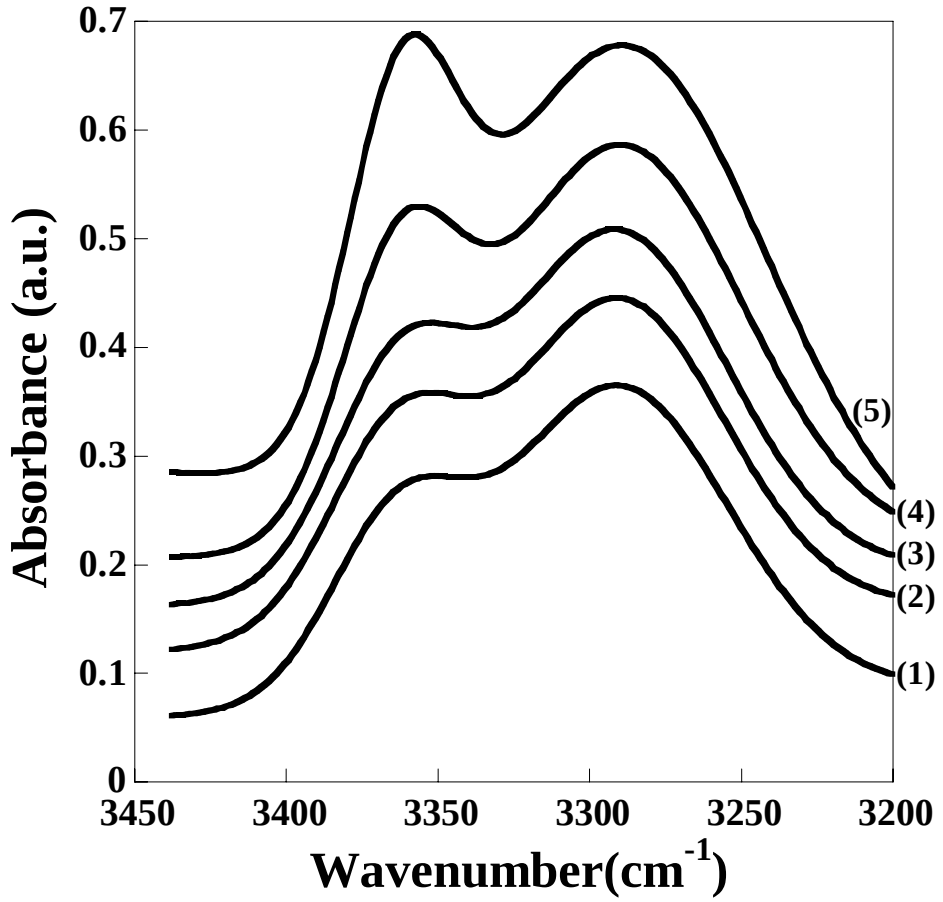

Figure 4.4: FT-IR spectra in the amine region for a composition gradient polyurethaneurea library at different chain extender stoichiometric ratios; cured at 90 ^{o}C for 6h; bottom to top: (1) 85 mole %, (2) 100 mole %, (3) 116 mole %, (4) 132 mole %, (5) 150 mole %. Spectra are arbitrarily offset.

Figure 4.5 is a representative FTIR spectrum in the carbonyl region taken from the ϕ-gradient library at ϕ = 85 mole %, cured at 90 ^{o}C, along with the individually fitted peaks from the deconvolution procedure. The peaks in the spectrum are identified in Table 1. The urea peaks were used to estimate the urea-urea hydrogen bonding and the total urea hydrogen bonding using the approach developed by Ning *et al*.[24], and the results are displayed in Figure 4.6.

Table 4.1: Absorption band assignments in the carbonyl region for polyurethaneurea.[15-17,23]

Wavenumber (cm^{-1})	Assignment
1730	Free urethane carbonyl
1716	Disordered, hydrogen-bonded urethane carbonyl
1709	Ordered, hydrogen bonded urethane carbonyl
1695	Free urea carbonyl
1651	Disordered, hydrogen bonded urea carbonyl
1642	Ordered, hydrogen bonded urea carbonyl

Figure 4.6a shows the dependence of urea-urea hydrogen bonding on T and ϕ for the twenty-five library spectra, and suggests that optimal mechanical strength will be observed in elastomers prepared at a ϕ = 85 - 116 mole % stoichiometry and T = 84 - 89 ^{o}C. Figure 4.6b shows that the maximum *total* urea hydrogen bonding occurs at cure T > 94 ^{o}C. Although more total urea hydrogen bonds are formed at higher temperature, the important bidentate urea-urea hydrogen bonding responsible for hard-segment formation are maximized at T = 84 - 89 ^{o}C. In the previously published cure temperature study, we

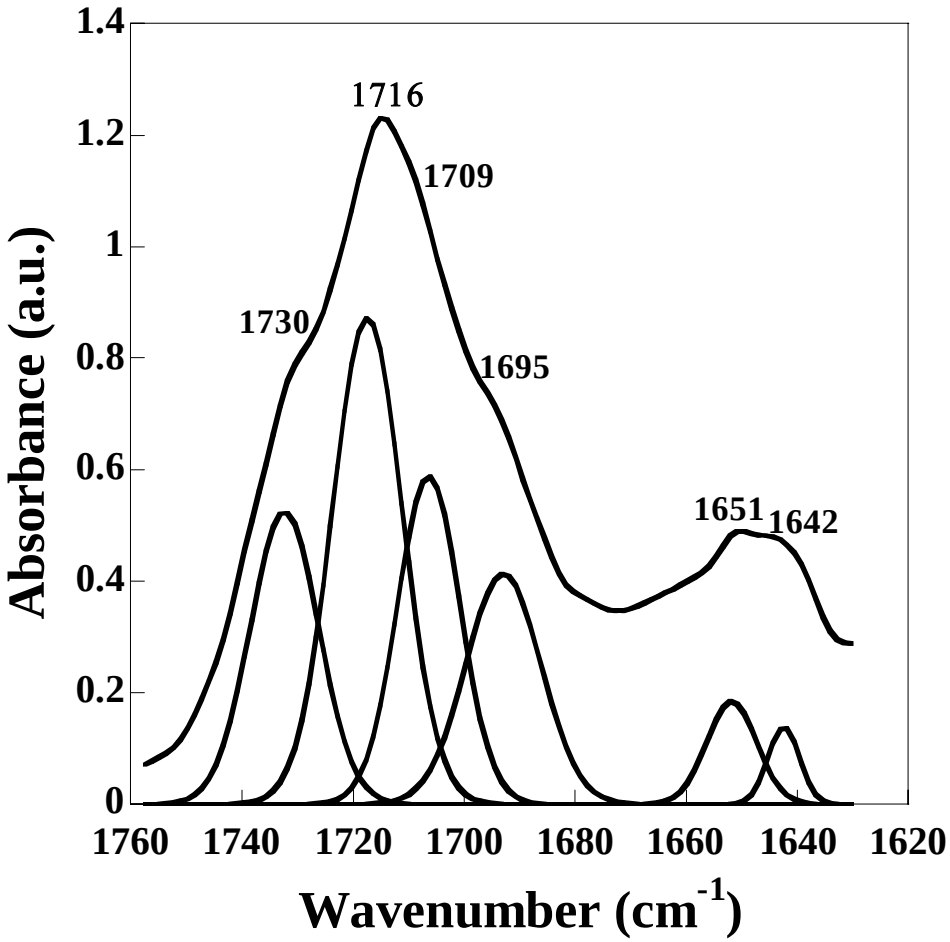

Figure 4.5: A representative spectrum in the carbonyl region for the composition gradient polyurethaneurea library at chain extender composition of 85 mole % cured at 90 ^{o}C for 6h.

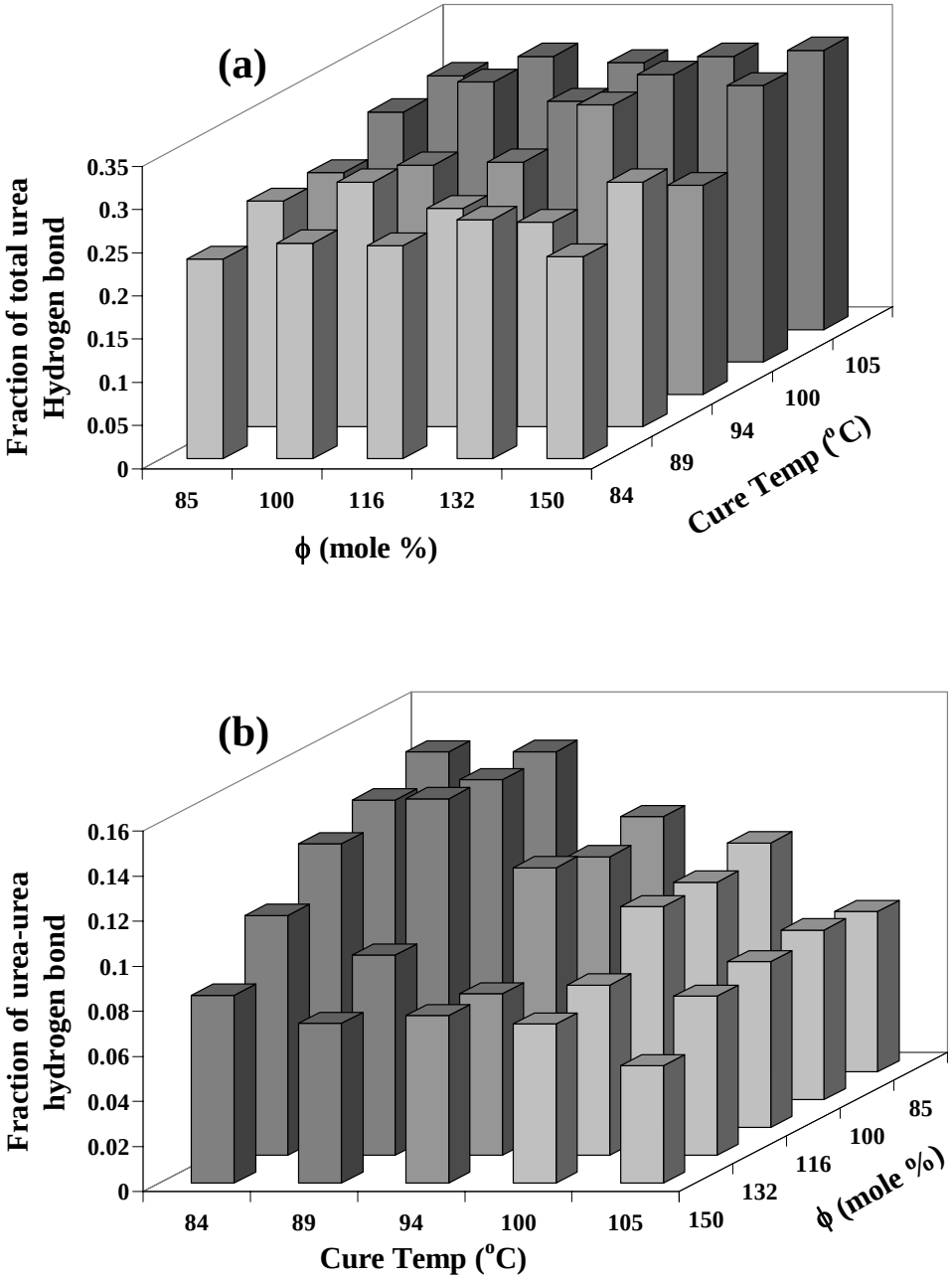

Figure 4.6: The dependence of urea hydrogen bonding on cure temperature and chain extender composition for polyurethaneurea library with orthogonal gradients in chain extender composition and cure temperature; cured for 6 h. (a) urea-urea hydrogen bonding, (b) total urea hydrogen bonding.

found that at ϕ = 95 mole %, optimum mechanical properties (elongation at break and impact strength) were observed at a cure temperature of 94 ^{o}C.[10] Based upon these FTIR screens, the remainder of this report will focus on results obtained from characterizing ϕ-gradient libraries cured at 90 ^{o}C, since the primary focus of this paper is to understand the utilization of ϕ–gradient high-throughput characterization. No discernable difference was observed in the dependence of ϕ and cure T on the total *urethane* hydrogen bonding.

Glass transition temperature (T_g) is used often to indicate the degree of phase separation in polyurethanes and polyurethaneureas. Figure 4.7 shows DSC traces (second heating run) of five polyurethaneurea samples, prepared at the same concentrations as those explored in the libraries. The soft segment T_g and other thermal characteristics are summarized in Table 2. DSC measurement for the pure soft-segment prepolymer (not included) showed a crystallization temperature at about -15 ^{o}C and a melting temperature of about 23 ^{o}C. The crystallization temperature (T_c) and melting temperature (T_m) are taken as the as the maximum and minimum of the peaks respectively. As shown in Table 2, there is an increase in soft segment T_g with an increase in chain extender composition. This increase in T_g suggests that phase mixing is enhanced when chain extender composition is increased, with more hard segments dissolving in the soft domains. Soft-segment crystallization exotherms were observed for samples with ϕ = 116, 132 and 150 mole %, with T_c decreasing with increasing ϕ as shown in Table 2, but crystallization exotherms were not observed at ϕ = 85 and 100 mole %. At these two lower chain extender compositions, the hard domains form strong physical crosslinks that probably hinder the molecular motion needed for strong soft-

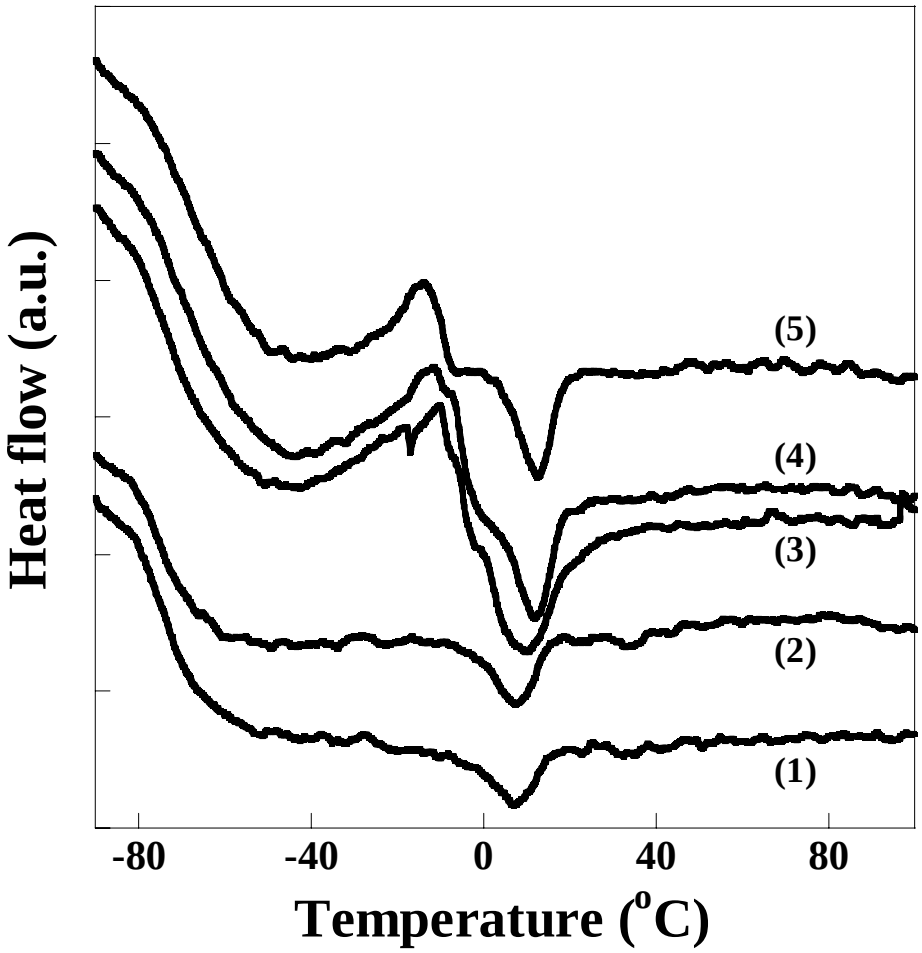

Figure 4.7: DSC curves (second heating) for uniform composition samples at different chain extender compositions; cured at 90 °C for 6h; bottom to top: (1) 85 mole %, (2) 100 mole %, (3) 116 mole %, (4) 132 mole %, (5) 150 mole %. Curves are arbitrarily offset.

Table 4.2: DSC data obtained from Figure 4.7.

Chain extender Composition (mole %)	$T_{Crystallization}$ (^oC)	$T_{Melting}$ (^oC)	Soft segment T_g (^oC)
85	_____	8.4	-73.5
100	_____	8.9	-72.4
116	-9.4	10.6	-70.9
132	-10.8	12.8	-67.1
150	-12.9	13.7	-65.7

segment crystallization. T_m increases with an increase in ϕ (Table 2), which correlates with the decrease in T_c. This suggests that at higher ϕ, less energy is needed to orient the soft segments for crystallization because of reduced hard and soft domain network connectivity, resulting in purer crystals that melt at higher temperatures. These observations correlate with the reduced urea-urea hard-segment H-bonding as ϕ is increased, and may lead to more thermoplastic or viscous behavior at high chain extender loadings.

Non-contact mode AFM has been used successfully to characterize the surfaces of a wide variety of phase-separated polymeric materials.[21,22,46-48] In non-contact AFM, different phases are detected by shifts in either the amplitude or phase of the oscillating tip, due to van der Waals interactions between the cantilever tip and the sample.[46,47] For SPUUs with rigid hard domains and flexible soft domains, contrast between the two phases results from the differences in the local stiffness of the two domains. The high modulus hard domains appear as light areas (+ phase shift), and the low modulus soft segments appear as dark areas (- phase shift).[21,22,37, 46-48] Fig. 4.8 shows moderate force[47] AFM non-contact phase images taken at different positions on the surface of a SPUU

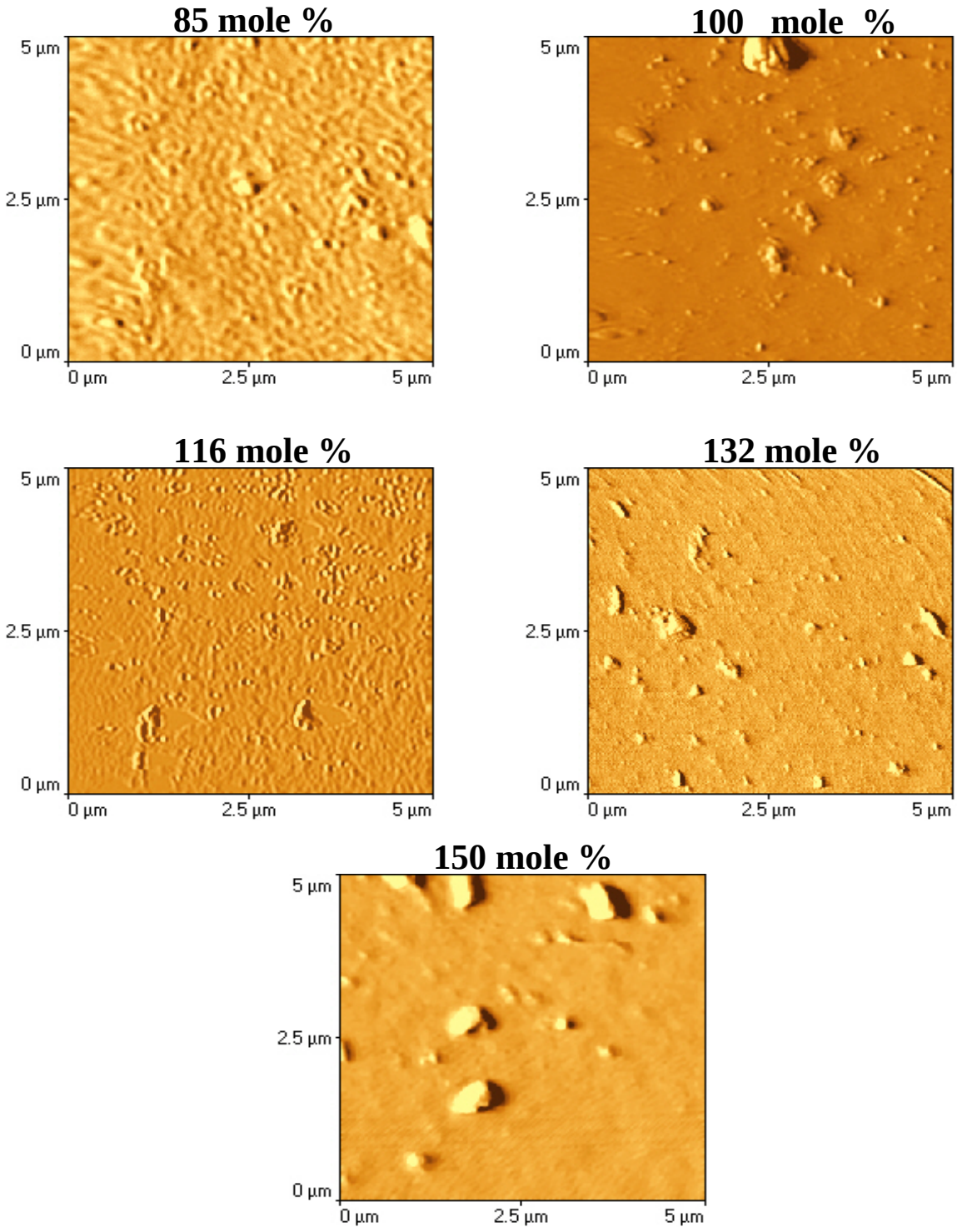

Figure 4.8: Noncontact mode AFM phase images at different chain extender compositions taken from a single composition gradient poly(urethane-urea) library; cured at 90 ^{o}C for 6h.

ϕ-gradient library. The image at 85 mole % shows the highest crosslink density with hard domains (diameter ~ 110 - 130 nm) evenly dispersed in the soft matrix. As the chain extender composition increases, the crosslink density decreases (fewer hard domains with larger interdomain spacing), and aggregation of hard domains is also observed. Reduced crosslink density and large hard domains tend to weaken the elastomeric (energy storage) capacity of the network, and will eventually result in a loss of elastomeric character (thermoplastic or viscous behavior).

With the notable exception of the elastomer prepared at 85 mole %, all of the other compositions were completely dissolved in DMF after several hours. This suggests that the elastomers prepared at $\phi \geq 100$ mole % chain extender stoichiometry are void of *chemical* cross-links. These results are reasonable since crosslinking via biuret or allophanate formation is expected only when excess isocyanate is present, e.g., $\phi < 100$ %. The chemically crosslinked 85 mole % elastomer was removed from the vial, carefully blotted to remove excess solvent, and weighed. The swell ratio (mass of swollen elastomer/initial mass of elastomer) was calculated to be 1.13. The magnitude of this ratio indicates that only a small fraction of hard domain is chemically crosslinked, and the majority of the hard domain results from physical crosslinking (hydrogen bonding) between hard segments.

Figure 4.9 shows stress (σ) versus strain (ε) data from five different positions on a ϕ-gradient library at an impact-magnitude strain rate of $v_0 = 0.9$ m/s using the *HTMECH* apparatus. Elongation at break, stress at break, and impact energy (area under curve) all decrease with increasing chain extender composition. The same trends were observed on

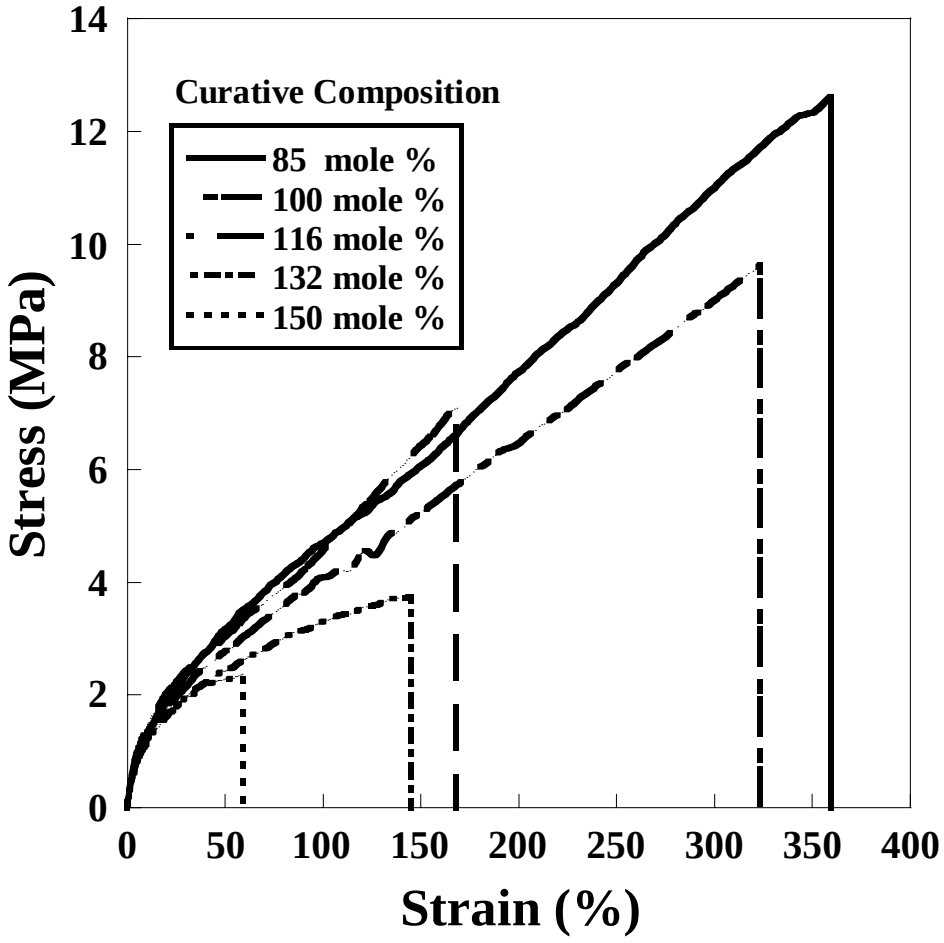

Figure 4.9: Stress-strain curves for a composition gradient polyurethaneurea library at different chain extender stoichiometric ratios. Library was cured at 90 ^{o}C for 6h; curves were obtained at an impact velocity of 0.89 m/s.

multiple (3x) composition gradient films and also from impacting *uniform* composition and cure *T* films. Figure 4.10 shows the σ vs. ε curves obtained at a *low strain rate* of 30 mm/s using both the *HTMECH* apparatus and a commercial uniaxial tensile instrument (Instron). The stress plotted in Figure 4.9 is based on the raw force measurement that indicates only the *z*-component (vertical), whereas for comparison, the corrected in-plane radial stress is plotted in Figure 4.10. Similar trends are observed from both instruments: the elongation at break and the maximum stress at failure decrease with increasing chain extender composition, also observed in the high velocity impact in Fig 4.9. Figures 4.10a and 10b show the σ vs. ε curves corresponding to 85 and 100 mole % chain extender, respectively, for both instruments. These two curves show three distinct regions characteristic of strain-crystallizing elastomers: an initial elastic rise, a plateau region, and a region with an upturn in slope due presumably to strain-induced crystallization.[43] These curves also show a nearly perfect overlay for both instruments between 50 - 300 % strain. Also, the percent elongation for both instruments agrees very well within the errors of mechanical measurements.

The curves at 116, 132 and 150 mole % chain extender (Figures 4.10c-4.10e) do not posses an upturn in slope after the plateau. Instead, the material fails within the plateau regime, suggesting that the excess chain extender causes a *decrease* in the capacity to store elastic energy. At higher chain extender composition, the material is probably acquiring plastic or viscoelastic character, as suggested by FTIR, DSC, and AFM data presented above. As these energy release mechanisms increase, the stored stress will decrease, as indicated in both Figs 4.9 and 4.10 and captured with both radial and uniaxial approaches. Although the shapes are similar, the stress versus strain from

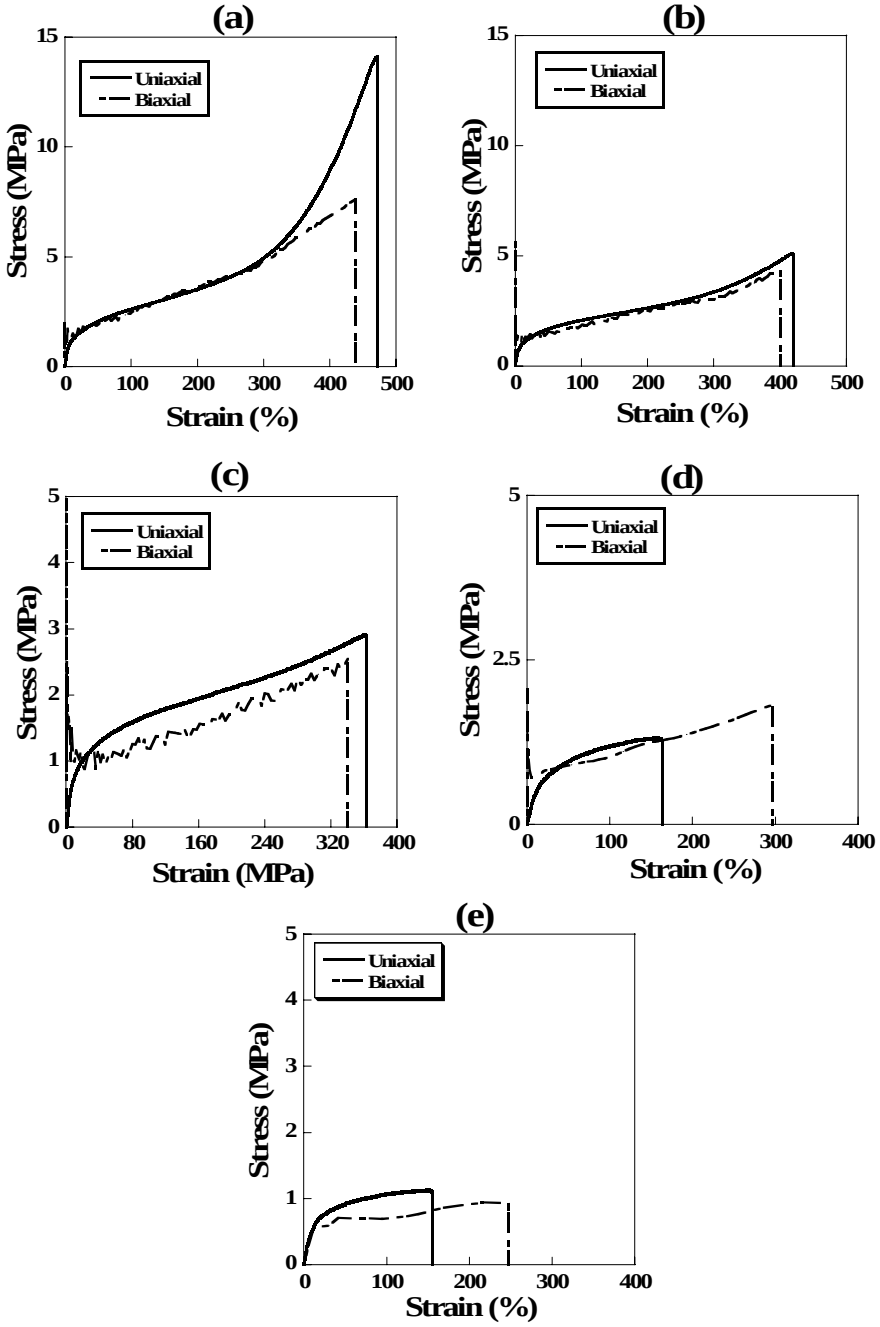

Figure 4.10 Stress-strain curves for uniform composition samples at different chain extender compositions; cured at 90 ^{o}C for 6h; curves were obtained from the *HTMECH* apparatus at v_0 = 30 mm/min and uniaxial loading using an Instron 5842 at v_0 = 30 mm/min; (a) 85 mole %, (b) 100 mole %, (c) 116 mole %, (d) 132 mole %, (e) 150 mole %.

HTMECH and conventional uniaxial do not agree quantitatively for the higher chain extender concentrations. In particular, at 132 % and 150 %, the % elongation at break is significantly higher in the radial geometry. Previous experiments comparing equibiaxial to uniaxial deformation of elastomers have observed the same phenomena.[49] The radial geometry may permit more plastic deformation or viscous dissipation prior to failure and plans are underway to examine this hypothesis.

The mechanical trends observed in Figs 4.9 and 4.10 correspond well with the structural information obtained from AFM, DSC, and FTIR library screening. In addition, Figure 4.8 showed that the hard domain density decreases and the interdomain spacing increases with increasing ϕ. Figure 4.6 showed that bidentate urea-urea hydrogen bonding diminished as ϕ increased cure temperatures. The excess H-bonded urea carbonyls are most likely H-bonding with urethane groups in the soft domains or urethanes that are mixed into the hard domains. These data, along with DSC measurements discussed above, indicate interdomain mixing and a structure that loses elastomeric character with increasing extender composition. At $\phi \geq 116$ %, chains may be "pulling out" of the network at sufficiently large deformations due to these network imperfections.

SEM images of the impacted surfaces were analyzed to gain an insight into the failure mechanisms at different chain extender compositions. Figure 4.11 shows that in going from 85 to 150 mole % chain extender, a transition from a rough surface with many fragments to a smoother surface with few fragments occurs. This trend follows the general relationship between fracture surface roughness and tear strength of elastomers, where rougher surfaces have higher tear strengths.[50,51] At 132 and 150 mole %, the

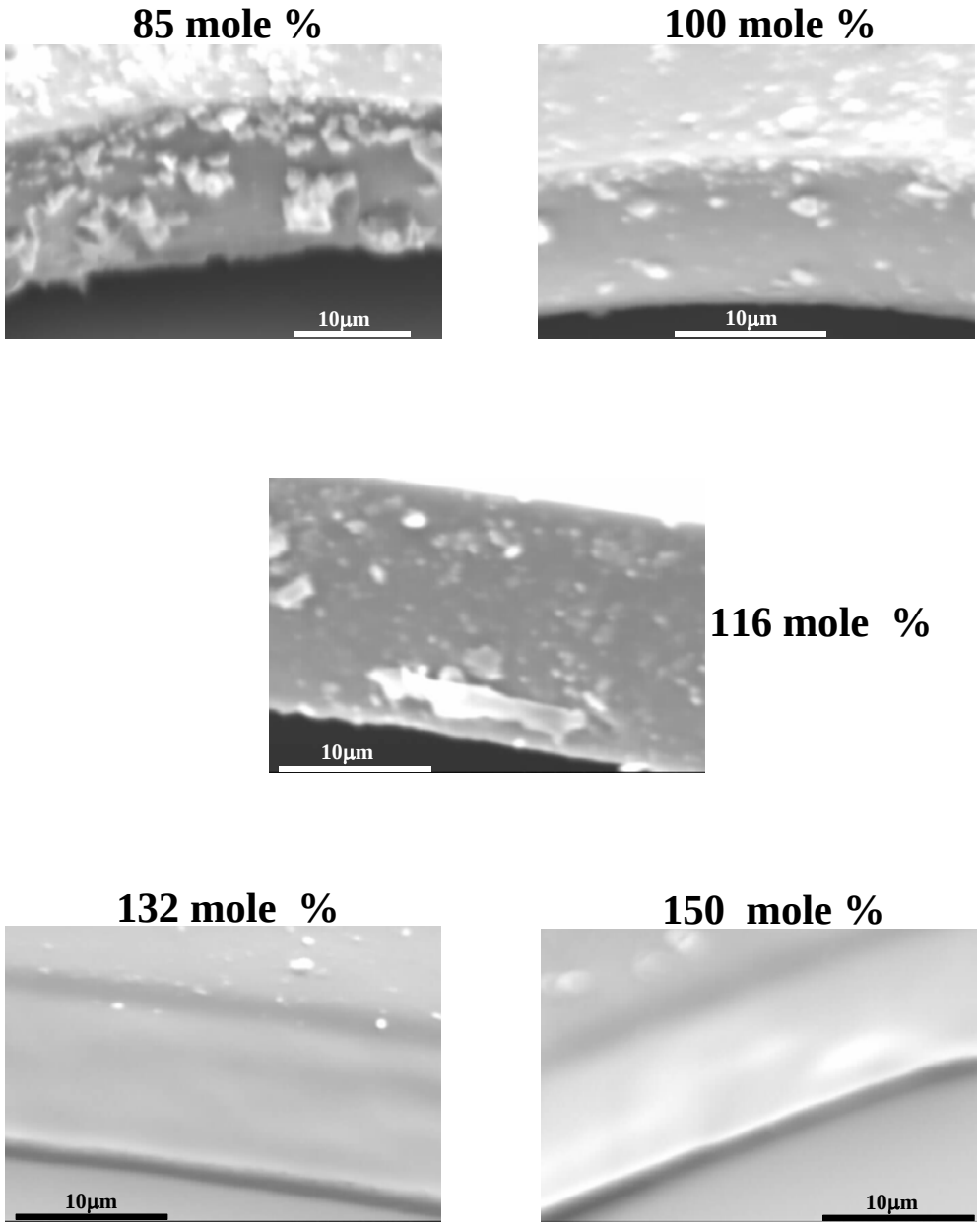

Figure 4.11: SEM images of the impact surfaces of the composition gradient library film described in Figure 4.9.

fractured surfaces were smooth and the stress versus strain data (see Figures 4.9 and 4.10) showed no indication of the strain-hardening typical of elastomers. With the structural data in Figs 4.6 – 4.8, these observations are strong evidence of a transition from purely elastomeric behavior towards a material with thermoplastic or viscous dissipation behavior.

Finally, we present a comparison of the *"effective"* secant modulus obtained from *HTMECH* with that obtained from a commercial uniaxial instrument (Instron 5842), shown in Fig 4.12. The secant modulus at 100% strain was calculated and compared for five different chain extender compositions, shown in Fig 4.10. A very good linear correlation was observed between the *HTMECH* (radial) and conventional (uniaxial) tensile measurements. The radial secant modulus obtained from *HTMECH* differs by about 40 % from the uniaxial modulus, but *only at the highest moduli* corresponding to the most highly elastic materials. The materials with high chain extender excess (lower modulus) show almost perfect agreement between the radial and uniaxial moduli, which may be due to a fortuitous cancellation in the nonlinear film profile errors (see Experimental). We tentatively attribute the differences in secant modulus for the nearly pure elastomeric materials (85 % and 100 % chain extender) to differences in the loading geometry that affect the onset and magnitude of both the nonlinear stress versus strain and nonaffine deformations. The nonlinear nature of stress developed in network deformation is known to depend on the loading geometry.[43] In addition, the onset of nonaffine deformation, thought to occur in the plateau region, allows molecular rearrangement of the network crosslinks that reduce the total stored elastic energy.[43] In

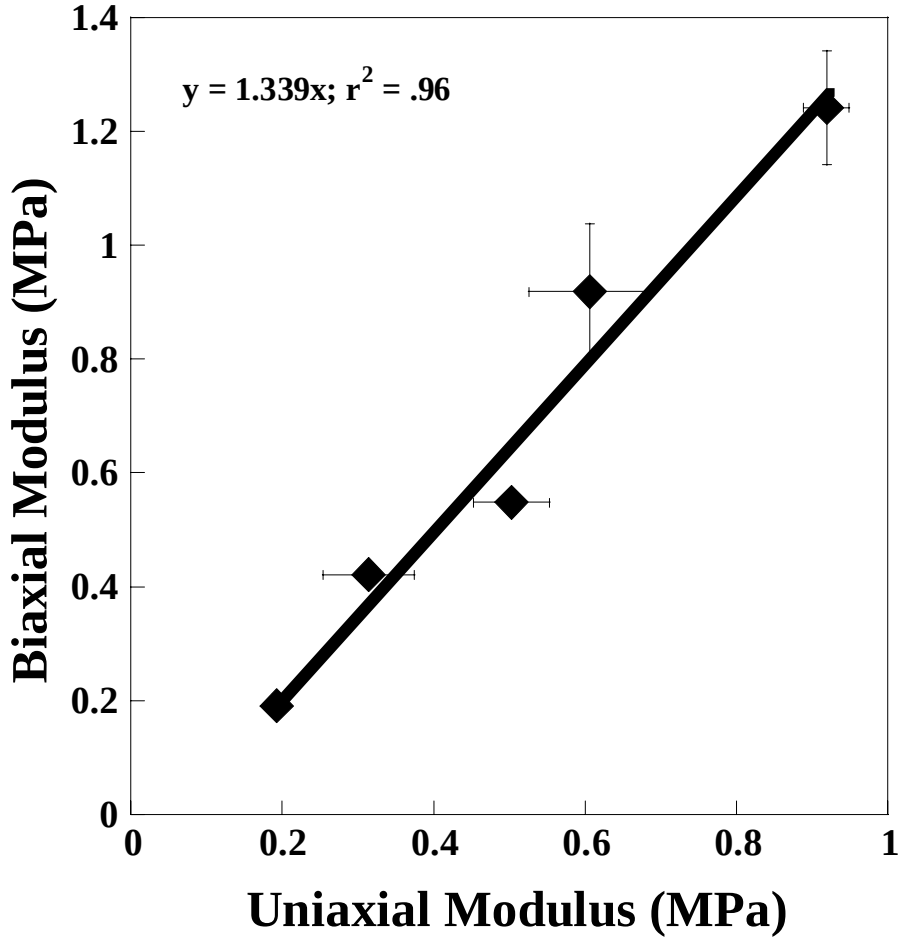

Figure 4.12: Comparison of the modulus at 100 % strain using the stress-strain curves presented in Figure 4.10.

the uniaxial test two dimensions are free to adjust in response to the loading, whereas only one dimension is free of loading in the radial test.

4.4 CONCLUSIONS

The effect of chain extender composition on the mechanical properties of segmented polyurethaneurea was investigated using composition gradient libraries coupled with a high throughput mechanical characterization apparatus, *HTMECH*, developed recently by the authors. Stress-strain curves from the composition gradient libraries showed an optimum in mechanical properties at the lowest chain extender composition examined, 85 mole %, which also agreed with measurements on uniform samples. At this stoichiometric ratio, the elastomer contained some chemical crosslinking, minimizing deformation of physically-crosslinked hard domains and creating a stronger interfacial bond with the soft domain. Spectroscopic and microscopic measurements on the library suggest that at chain extender stoichiometry greater than 116 mole %, excess hard segments are dispersed in the soft domain and urea-urea H-bonding is diminished, increasing the degree of phase mixing. Phase mixing tends to reduce the energy storage (elastomeric) character and can result in viscous or plastic energy dissipation processes. In this regard, rather simple FTIR screens of urea-urea hydrogen bonding fractions are a reliable indicator of the trends observed in tensile strength and % elongation. A comparison of the mechanical results obtained from HTMECH (radial) versus a commercial uniaxial instrument demonstrates a strong correlation between the Young's modulus and trends in the tensile strength and % elongation. These

measurements serve to illustrate the utility of HTMECH as a convenient and accurate screening tool for mechanical properties in gradient polymer films.

4.5 REFERENCES

(1) Meredith, J. C.; Karim, A.; Amis, E. J., High-Throughput Measurement of Polymer Blend Phase Behavior. *Macromolecules* **2000,** 33, (16), 5760.

(2) Meredith, J. C.; Smith, A. P.; Karim, A.; Amis, E. J., Combinatorial Materials Science for Polymer Thin-Film Dewetting. *Macromolecules* **2000,** 33, (26), 9747.

(3) Tomlinson, M. R.; Genzer, J., Formation of Grafted Macromolecular Assemblies with a Gradual Variation of Molecular Weight on Solid Substrates. *Macromolecules* **2003,** 36, (10), 3449.

(4) Tomlinson, M. R.; Genzer, J., Formation of Surface-Grafted Copolymer Brushes with Continuous Composition Gradients. *Chem. Commun.* **2003**, 1350.

(5) Beers, K. L., Douglas, J.F., Amis, E.J., Karim, A., Combinatorial Measurements of Crystallization Growth Rate and Morphology in Thin Films of Isotactic Polystyrene. *Langmuir* **2003,** 19, 935.

(6) Ashley, K. M., Meredith, J.C., Amis, J., Raghavan, D., Karim, A., Combinatorial Investigation of Dewetting: Polystyrene Thin Films on Gradient Hydrophilic Surfaces. *Polymer* **2003,** 44, 769.

(7) Smith, A. P.; Douglas, J. F.; Meredith, J. C.; Amis, E. J.; Karim, A., High-Throughput Characterization of Pattern Formation in Symmetric Diblock Copolymer Films. *J. Polym. Sci., Part B: Polym. Phys.* **2001,** 39, 2141.

(8) Meredith, J. C., Sormana, J.-L., Keselowsky, B., Garcia, A.J., Tona, A., Karim, A., Amis, E.J., Combinatorial Characterization of Cell Interactions with Polymer Surfaces. *J. Biomed. Matter. Res.* **2003,** 66, 483.

(9) Sormana, J.-L., Meredith, J.C., High-Throughput Dynamic Impact Characterization of Polymer Films. *Mater. Res. Innov.* **2003,** 7, (5), 295.

(10) Sormana, J.-L., Meredith, J.C., High-Throughput Screening of Mechanical Properties on Temperature-Gradient Polyurethaneurea Libraries. *Macromol. Rapid Comm.* **2003**, 118.

(11) Stafford C.M., H., C., Karim, A., Amis, E.J., Measuring the Modulus of Polymer Films by Strain-Induced Buckling Instabilities. *Abstracts of Papers of the American Chemical Society* **2002,** 220-Poly Part 2, 224.

(12) Hoogenboom, R., Meier, M.A.R., Schubert, U.S., Combinatorial Methods, Automated Synthesis and High-Throughput Screening in Polymer Research: Past and Present. *Macromol. Rapid Comm.* **2003,** 24, 15.

(13) Chapon, P., Mignaud, C., Gilda, L., Destarac, M., Automated Parallel Synthesis of MADIX (Co)Polymers. *Macromol. Rapid Comm.* **2003,** 24, 87.

(14) Zhang, H., Fijten, M.W.M., Hoogenboom, R., Reinierkens, R., Schubert, U.S., Application of Parallel Synthetic Approach in Atom-Transfer Radical Polymerization: Set-Up and Feasibility Demonstration. *Macromol. Rapid Comm.* **2003,** 24, 81.

(15) Paik Sung, C. S.; Hu, C. B.; Wu, C. S., Properties of Segmented Poly(urethaneureas) Based on 2,4-Toluene Diisocyanate. **1**. Thermal Transitions, X-ray Studies, and Comparison with Segmented Poly(Urethanes). *Macromolecules* **1980,** 13, 111.

(16) Paik Sung, C. S.; Smith, T. W., Properties of Segmented Polyether Poly(urethaneureas) Based on 2,4-Toluene Diisocyanate. 2. Infrared and Mechanical Studies. *Macromolecules* **1980,** 13, 117.

(17) Wang, C. B.; Cooper, S. L., Morphology and Properties of Segmented Polyether Polyurethaneureas. *Macromolecules* **1983,** 16, 775.

(18) Beck, R. A.; Truss, R. W., The Effect of Stoichiometry on Fracture Toughness of a Polyurethane-urea Elastomer. *Polymer* **1999,** 40, 307.

(19) Wu, L.; Li, D.; You, B.; Qian, F., Change in Mechanical Properties, Composition, and Structure of Hydrated Polyurethaneurea. *J. App. Polym. Sci.,* **2001,** 80, 252.

(20) Wu, L.; You, B.; Li, D.; Qian, F., Effect of Hydration on the Mechanical Properties, Composition and Molecular Weight of Polyurethaneureas. *Polym. Int.* **2000,** 49, 1609.

(21) Garrett, J. T., Runt, J., Microphase Separation of Segmented Poly(urethane urea) Block Copolymers. *Macromolecules* **2000,** 33, 6353.

(22) Garrett, J. T.; Siedlecki, C. A.; Runt, J., Microdomain Morphology of Poly(urethane urea) Multiblock Copolymers. *Macromolecules* **2001,** 34, 7066.

(23) Ishihara, H., Kimura, I., Saito, K., Ono, H., Infrared Studies on Segmented Polyurethane-Urea Elastomers. *J. Macromol. Sci.-Phys.,* **1974,** B10(4), 591.

(24) Ning, L., De-Wing, W., Sheng-Kang, Y., Crystallinity and Hydrogen Bonding of Hard Segments in Segmented Poly(urethaneurea) Copolymers. *Polymer* **1996,** 37, (16), 3577.

(25) Musselman, S. G.; Santosusso, T. M.; Barnes, J. D.; Sperling, L. H., Domain Structures and Interphase Dimensions in Poly(urethaneurea) Elastomers Using DSC and SAXS. *J. Polym. Sci., Part B: Polym. Phys.* **1999,** 37, 2586.

(26) Osaki, K.; Kimura, S.; Nishizawa, K.; Kurata, M., SAXS Studies of Segmented Polyether Poly(urethaneurea) Elastomers. *Macromolecules* **1980,** 14, 456.

(27) Chiou, B.-S.; Schoen, P. E., Effects of Crosslinking of Thermal and Mechanical Properties of Polyurethanes. *J. App. Polym. Sci.,* **2002,** 83, 212.

(28) Haska, S. B., Bayramli, E., Pekel, F., Ozkar, S., Mechanical Properties of HTPB-IPDI-based Elastomers. *J. App. Polym. Sci.,* **1997,** 64, 2347.

(29) Spirkova, M., Matejka, L., Hlavata, D., Meissner, B., Pytela, J., Polybutadiene-Based Polyurethanes with Controlled Properties: Preparation and Characterization. *J. App. Polym. Sci.,* **2000,** 77, 381.

(30) Petrovic, Z. S.; Ilavsky, M.; Dusek, K.; Vidakovic, M.; Javni, I.; Banjanin, B., The Effect of Crosslinking on Properties of Polyurethane Elastomers. *J. App. Polym. Sci.,* **1991,** 42, 391.

(31) Petrovic, Z. S.; Javni, I.; Banhegyi, G., Mechanical and Dielectric Properties of Segmented Polyurethane Elastomer Containing Chemical Crosslinks in the Hard Segments. *J. Polym. Sci., Part B: Polym. Phys.* **1998,** 36, 237.

(32) Petrovic, Z. S.; Ferguson, J., Polyurethane Elastomers. *Prog. Polym. Sci.,* **1991,** 16, 695.

(33) Spathis, G., Niaounakis, M., Kontou, E., Apekis, L., Pissis, P., Christodoulides, C., Morphological Changes in Segmented Polyurethane Elastomers by Varying the NCO / OH Ratio. *J. App. Polym. Sci.,* **1994,** 54, 831.

(34) Huang, J.; Zhang, L., Effects of NCO/OH Molar Ration on Structure and Properties of Graft-Interpenetrating Polymer Networks from Polyurethane and Nitrolignin. *Polymer* **2002,** 43, 2287.

(35) Huang, S.-L., Lai, J.-Y., Structure-Tensile Properties of Polyurethanes. *Euro. Polym. J.* **1997,** 33, (10-12), 1563.

(36) Petrovic, Z. S.; Javni, I.; Divjakovic, V., Structure and Physical Properties of Segmented Polyurethane Elastomers Containing Chemical Crosslinks in the Hard Segments. *J. Polym. Sci., Part B: Polym. Phys.* **1998,** 36, 221.

(37) O'Sickey, M. J.; Lawrey, B. D.; Wilkes, G. L., Structure-Property Relationships of Poly(urethane urea)s with Ultra-low Monol Content Poly(propylene glycol) Soft Segments. I. Influence of Soft Segment Molecular Weight and Hard Segment Content. *J. App. Polym. Sci.,* **2002,** 84, 229.

(38) Meredith, J. C., Karim, A., Amis, E.J., Combinatorial Methods for Investigations in Polymer Materials Science. *MRS Bulletin* **2002,** 27, (4), 330.

(39) Smith, A. P.; Douglas, J. F.; Meredith, J. C.; Amis, E. J.; Karim, A., Combinatorial Study of Surface Pattern Formation in Thin Block Copolymer Films. *Phys. Rev. Lett.* **2001,** 87, (1), 15503.

(40) Green, A. E., Adkins, J. E., *Large Elastic Deformations*. Oxford University Press: Oxford, **1960**.

(41) Mooney, M., A Theory of Large Elastic Deformation. *J. Appl. Phys.* **1940,** 11, 582.

(42) Yang, X. F.; Vang, C.; Tallman, D. E.; Bierwagen, G. P.; Croll, S. G.; Rohlik, S., Weathering Degradation of Polyurethane Coating. *Polym. Deg. and Stab.* **2001,** 74, 341.

(43) Wan, K.-T., Liao, Kin, Measuring Mechanical Properties of Thin Flexible films by a Shaft-Loaded Blister Test. *Thin Solid Films* **1999,** 352, 167.

(44) Liu, K. K., Ju, B. F., A Novel Technique for Mechanical Characterization of Thin Elastomeric Membrane. *J. Phys. D. Appl. Phys.* **2001,** 34, (15), 91.

(45) Urayama, H., Kanamori, T., Kimura, Y., Properties and Biodegradability of Polymer Blends of Poly(L-lactide)s with Different Optical Purity of the Lactate Units. *Macromol. Materials and Eng.* **2002,** 287, (2), 116.

(46) Magonov, S. N., Elings, V., Papkow, V.S, AFM Studies of Thermotropic Structural Transitions in Poly(diethylsiloxane). *Polymer* **1997,** 38, (2), 297.

(47) McLean, R. S.; Sauer, B. B., Tapping-Mode AFM Studies Using Phase Detection for Resolution of Nanophase in Segmented Polyurethanes and Other Block Copolymers. *Macromolecules* **1997,** 30, 8314.

(48) Grandy, D. B.; Hourston, D. J.; Price, D. M.; Reading, M.; Silva, G. G.; Song, M.; Sykes, P., Microthermal Characterization of Segmented Polyurethane Elastomers and a Polystyrene-Poly(methyl methacrylate) Polymer Blend Using Variable Temperature Pulsed Force Mode Atomic Force Microscopy. *Macromolecules* **2000,** 33, 9348.

(49) Dickie, R. A. S., T. L., Ultimate Tensile Properties of Elastomers. 6. Strength and Extensibility of a Styrene-Butadiene Rubber Vulcanizate in Equal Biaxial Tension. *J. Polym. Sci., Part A-2: Polym. Phys* **1969,** 7, (4PA2), 687.

(50) Gent, A. N., Pulford, C.T.R., Micromechanics of Fracture in Elastomers. *J. Materials Science* **1984,** 19, 3612.

(51) Kuriakose, B., De, S.K., Scanning Electron Microscopy Studies of Tensile, Tear and Abrasion Failure of Thermoplastic Elastomers. *J. Materials Science* **1985,** 20, 1864.

CHAPTER 5

HIGH-THROUOGHPUT SCREENING OF MECHANICAL PROPERTIES ON TEMPERATURE-GRADIENT POLYURETHANEUREA LIBRARIES

Combinatorial libraries of segmented polyurethaneurea with gradients in curing temperature were prepared and characterized using a novel high-throughput mechanical instrument. Stress-strain profiles taken at different temperature positions on the libraries showed an optimum curing temperature of 94 ^{o}C for high-strain rate (0.9 m/s), but no optimum temperature for slow strain rates (1 mm/s). A structure-property relationship between microstructure and mechanical properties was established by correlating the measured strength and strain at break to high-throughput AFM and FTIR measurements on the same library. These results demonstrate the feasibility of rapid and accurate screening of mechanical properties, and their correlation to structure, by using gradient combinatorial polymer libraries.

5.1 INTRODUCTION

Segmented polyurethaneurea (SPUU) elastomers are block copolymers with a microphase-separated morphology that consists of alternating rubbery (soft) and glassy or crystalline (hard) segments. Phase-separation is driven by hard and soft segment incompatibility and hydrogen bonding between hard segments. The study of SPUU elastomers has attracted tremendous attention because of their superior elasticity and strength compared to polyurethanes,[1] and their many applications in coatings, adhesives, textiles, and other consumer products.

The mechanical properties of SPUUs, as well as other thermoset polymers, are a sensitive and complex function of the two-phase morphology, the strength of hydrogen bonds between segments, and processing variables. For example, the morphology and extent of H-bonding depends on cure temperature (T) and time, as characterized using FTIR, DSC, AFM, and X-ray Diffraction.[1-6] However, efficient exploration of these effects is an expensive, time-consuming task using conventional 1-sample-for-1-measurement techniques. We recently reported a T-gradient combinatorial library approach to characterizing the effects of processing on polymers, used to investigate phase separation and wetting phenomena.[7-10] Here, we demonstrate mechanical characterization of T-gradient libraries of SPUUs using a novel high-throughput impact characterization apparatus.[11] The goal is not to replace conventional detailed mechanics and fracture measurements, but rather to introduce a new high-throughput mechanical screening tool while giving up as little accuracy and precision as possible. To illustrate the potential for developing structure-property relationships, mechanical properties

measured with the high-throughput method are related to the microphase-separated structure and H-bonding using AFM and FTIR measurements.

5.2 EXPERIMENTAL

5.2.1 Materials and Synthesis

Separate solutions of toluene-diisocyanate end-capped poly(tetramethylene glycol) prepolymer (Air Product and Chemicals, AIRTHANE® PET-85A, M_w = 2500) and trimethylene glycol di-*p*-aminobenzoate (Air Products and Chemicals, VERSALINK® 740-M) curative (chain extender) were mixed to a total concentration of 30 mass % in tetrahydrofuran (VWR, ACS Grade). Tetrahydrofuran was dried with molecular sieve to prevent unwanted reactions with water. The prepolymer and curative solutions were mixed to achieve 95 mole % of the stoichiometric curative needed to react with all prepolymer isocyanate end groups. This mixture was coated on clean Si wafers using a knife coater.[7-10] The coated silicon wafers were cured for 6 h on a linear *T*-gradient stage[7-10] under vacuum of -1 bar, with lower and upper endpoint temperatures of 70 ^{o}C and 130 ^{o}C. After curing, the thickness at various positions on the film was measured by visible-near infrared interferometry (Stellar Net EPP 2000). The films, with an average thickness of 25 μm, were peeled from the Si wafer after soaking in water, and were dried under vacuum prior to analysis.

5.2.2 Characterization

Libraries were placed on a ZnSe substrate for chemical analysis by FTIR, recorded using an automated Bruker IRscope II at room temperature and 4 cm^{-1} resolution. Peak separation and analysis (Peakfit® 4.11) was used to resolve bands and

obtain peak areas (Gaussian line shape) in the carbonyl region (ν = 1630-1740 cm^{-1}). AFM amplitude images of the film were taken in non-contact mode using a Thermomicroscopes SPM Explorer, with SFM # 1650 probes. Stress-strain curves are measured at distinct points across the library with a high-throughput impact and strain apparatus developed for characterization of polymer gradient libraries. Details on the design and validation of this instrument can be found elsewhere.[11] Briefly, the sample library is contacted with a 500 μm diameter steel pin at a constant velocity ranging from (0.001 to 1) m/s, with the pin oriented normal to the film surface, resulting in equi-biaxial deformation. Measurement points are isolated on the library with a steel grid of 3 mm diameter holes at 4 mm spacing. A force-transducer records the force profile for each of the 100 measurement sites on a typical 40 mm x 40 mm library. After indentation, the films were coated with a thin layer of gold and SEM images of the fracture surfaces were taken using a Hitachi 3500H SEM.

5.3 RESULTS AND DISCUSSION

Surface temperature measurements were taken on a clean silicon wafer placed on a temperature gradient stage and the result of the analysis is presented in Figure 5.1. As expected, the temperature varied linearly from one endpoint to the other, and the same x, but different y-positions remained constant to within ± 0.5 ^{o}C. Figure 5.2 shows FT-IR spectra taken at different positions, corresponding to different cure temperatures on a temperature-gradient library. Quantitative analysis of the degree of hydrogen bonding as a function of temperature was performed using three peaks in the carbonyl region of the FTIR. These peaks are identified as: (1) free urea carbonyl, ν = 1690-1695 cm^{-1}, (2)

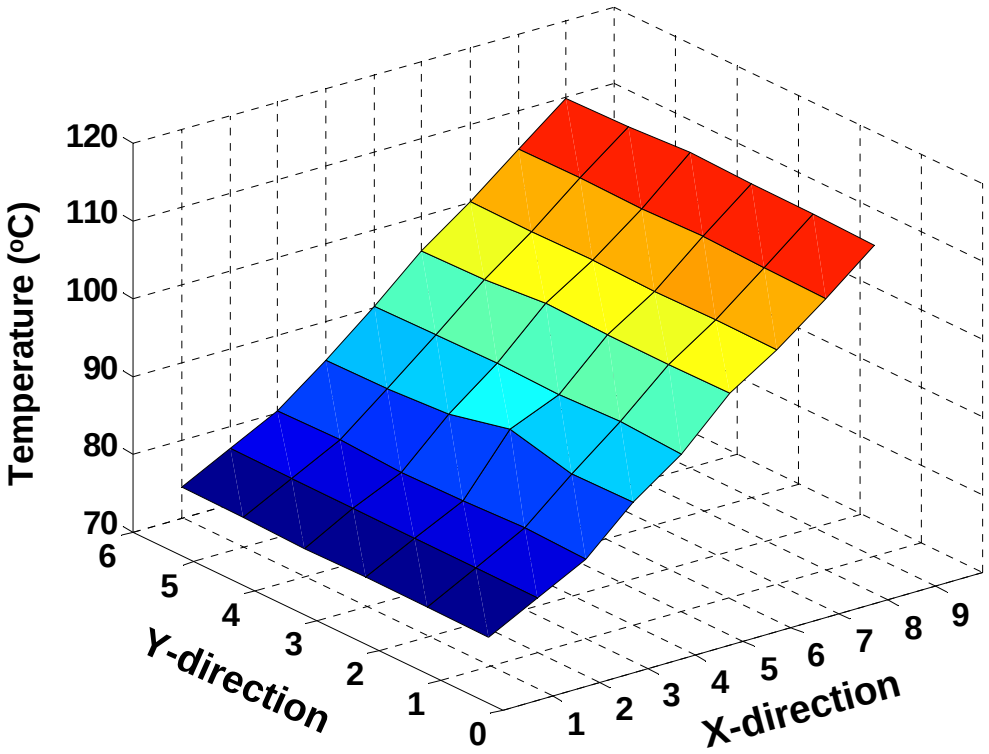

Figure 5.1: Surface temperature measurements at different x and y positions on the temperature gradient stage.

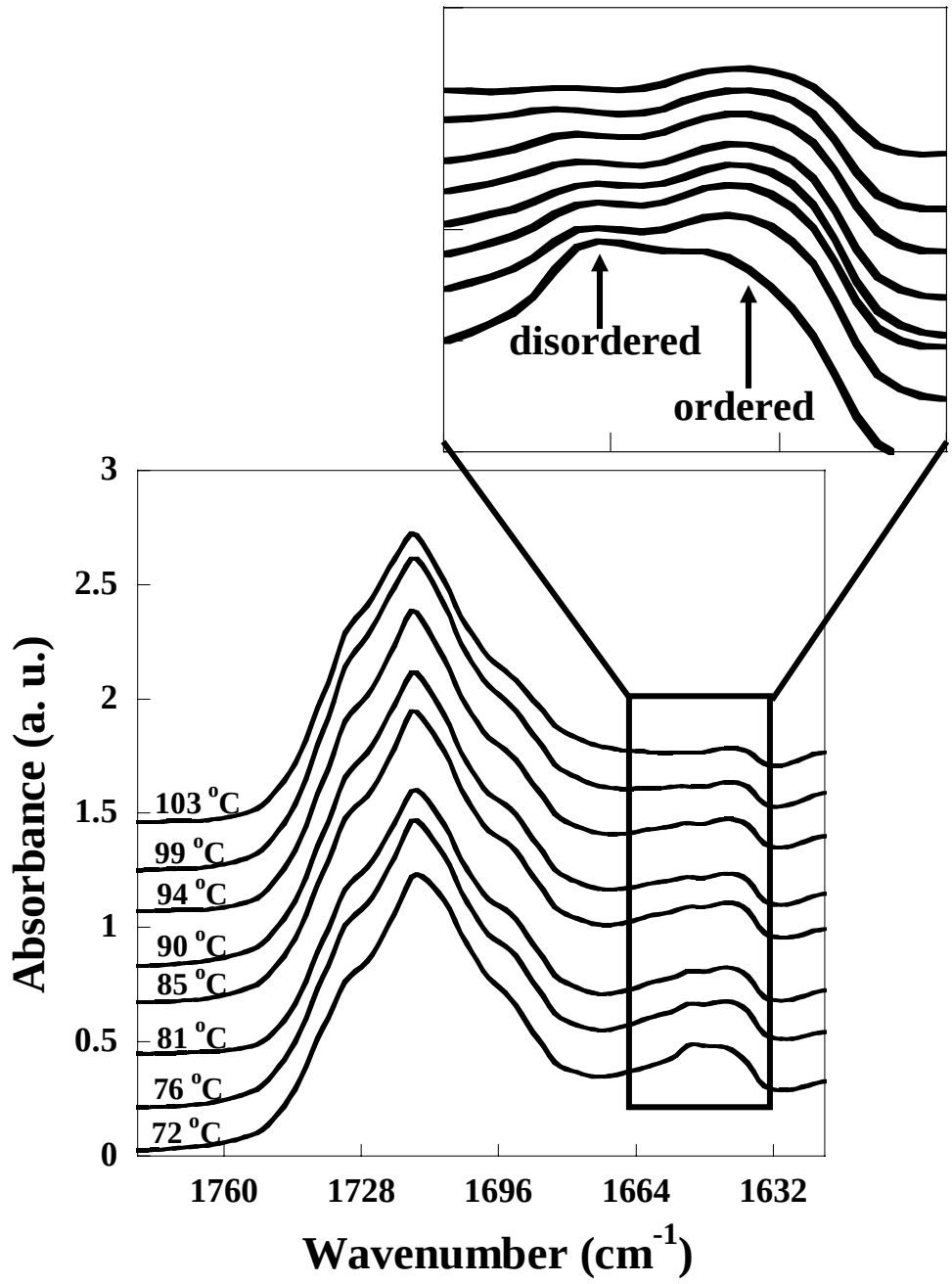

Figure 5.2: FT-IR spectra in the carbonyl region at different positions (cure temperatures) on a temperature gradient polyurethaneurea library, cured at 95 mole % stoichiometry for 6h. Spectra are equally offset at an absorbance of 0.2.

disordered H-bonded urea carbonyl, ν = 1650-1655, and (3) ordered (i.e., within hard domains) H-bonded urea carbonyl, ν = 1640-1645.[3,5-6] Qualitatively, Figure 5.2 shows an increase in the ratio of ordered H-bonded urea carbonyl to disordered H-bonded urea carbonyl with increase in cure temperature. As cure temperature increase, unfavorable H-bonds are broken and the added thermal energy increases the mobility of the chains, leading to the formation of more favorable ordered H-bonded urea carbonyl. We note that analysis of the isocyanate (NCO) peak at 2260 cm^{-1} showed that conversion was complete at all T values explored. The *total* mole fraction of H-bonded urea ($X_{T,UA}$) and the fraction of *ordered* H-bonded urea ($X_{O,UA}$) was calculated using the approach of Ning *et al.*[5] Since thermal energy favors H-bond dissociation, $X_{T,UA}$ decreases continuously with an increase in cure T, as shown in Figure 5.3. An interesting transition occurs between 94 and 99 ^{o}C, marked by a sharper decrease in $X_{T,UA}$ with T. Two types of urea-urea H-bonds are known in SPUUs: a *single* bond between one carbonyl and one NH and a *bidentate* H-bond between one carbonyl and two NH groups.[3] The bidentate bonds are stronger than single H-bonds and are expected to dissociate at higher temperatures than the single bonds. It appears that at T > 94 ^{o}C, sufficient thermal energy is provided to begin breaking the bidentate H-bonds, resulting in a sharp decline in $X_{T,UA}$. Also shown in Figure 5.3 is the dependence of $X_{O,UA}$ on temperature. An optimal $X_{O,UA}$ is observed between 76 and 94 ^{o}C, suggesting that more favorable H-bonding between hard segments occurred between 76 and 94 ^{o}C, leading to stronger hard domains. At T > 94 ^{o}C, $X_{O,UA}$ decreases, indicating H-bond dissociation within hard domains, weakening these domains.

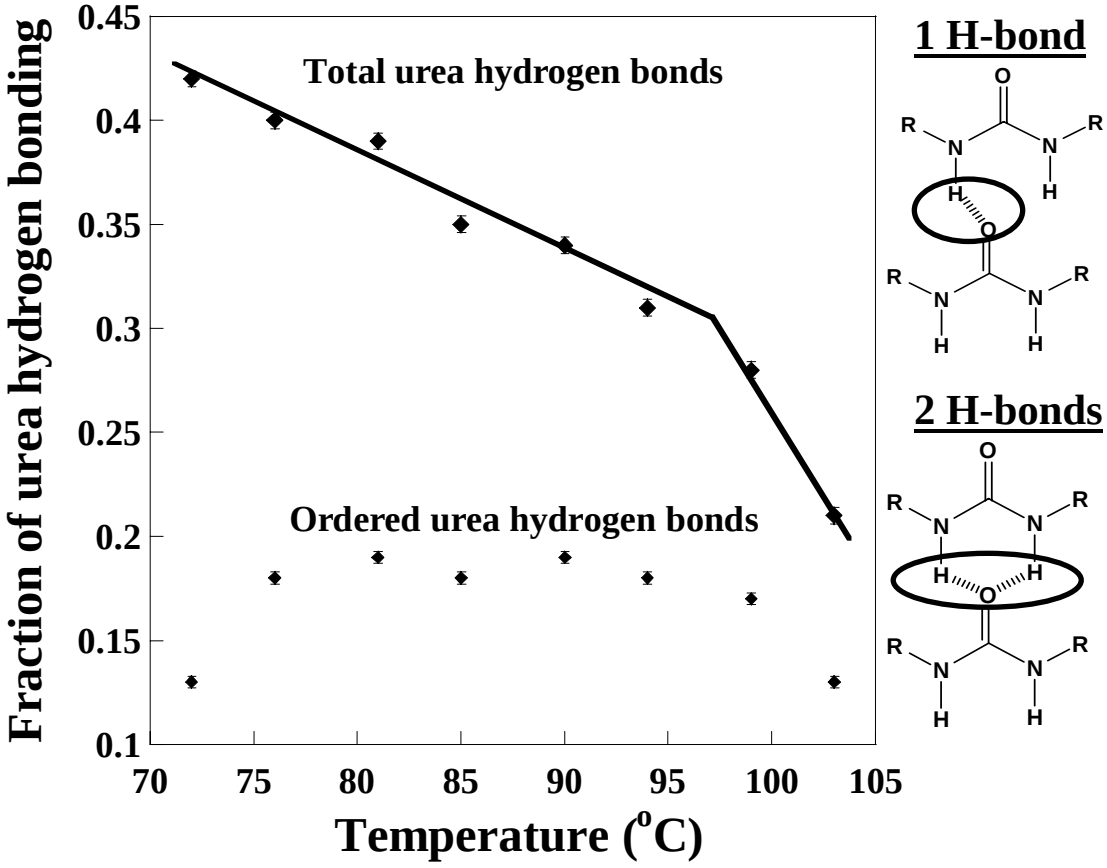

Figure 5.3: The influence of temperature on the extent of total urea ($X_{T,UA}$) and interurea ($X_{,O,UA}$) hydrogen bonds in a temperature gradient SPUU library; cured at 95 mole % curavite stoichiometry for 6h. Data is obtained from Figure 5.2.

Non-contact AFM allows characterization of contrast between hard and soft domains on the SPUU library surface due to contrast arising from differences in the local stiffness, which affects the phase of the oscillating cantilever. As a result, high modulus hard domains appear lighter than the low modulus soft domains.[12-15] During curing, the desired microphase-separation of hard domains made stable by urea-urea hydrogen-bonding, competes against aggregation of hard domains into large, micron-sized aggregates. This aggregation is driven by the need to minimize the hard-soft domain interfacial area. Fig 5.4 shows AFM images taken at different positions on a *T*-gradient library. The 94 ^{o}C image indicates the least hard domain aggregation along with a nearly uniform dispersion of microphase-separated hard domains (average diameter 120 nm). At temperatures other than 94 ^{o}C, more hard domain aggregation to a large range of sizes is observed, which has a negative impact on strength since the large hard domains serve as flaws for crack initiation. This may be explained by considering that the thermal energy added as *T* is increased to 94 ^{o}C may allow hard-segment chain alignment into bidentate H-bonds that stabilize the microphase-separated morphology. At temperatures greater than 94 ^{o}C, the additional thermal energy apparently begins to break bidentate H-bonds (Fig 5.3).

Force-time data obtained from the combinatorial libraries are plotted as engineering stress (σ) versus strain (ε) in Figure 5.5. The strain was calculated as the ratio of radial elongation to the initial radius of the measurement hole (r_o = 1.5 mm), and stress was calculated as the force divided by the area at the clamped sample perimeter ($2\pi rh$, h = film thickness). Fig 5.5a shows that the σ vs. ε curves are sensitive to cure *T* at high strain rate (0.9 m/s), whereas Fig 5.5b shows that cure *T* does not have a

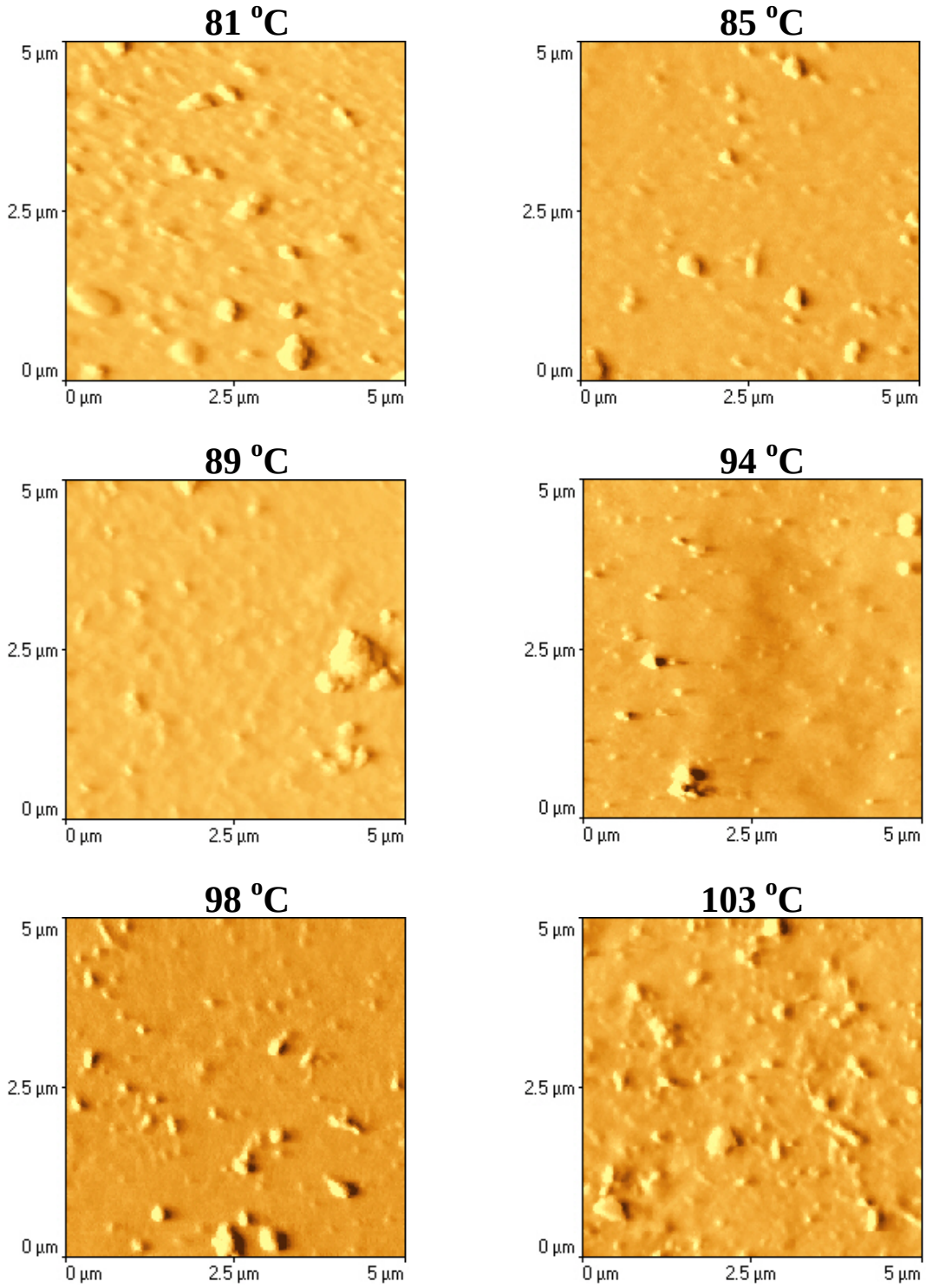

Figure 5.4: Non-contact-mode AFM phase images at different positions (cure temperatures) on a SPUU library; cured at 95 mole % curative stoichiometry for 6h.

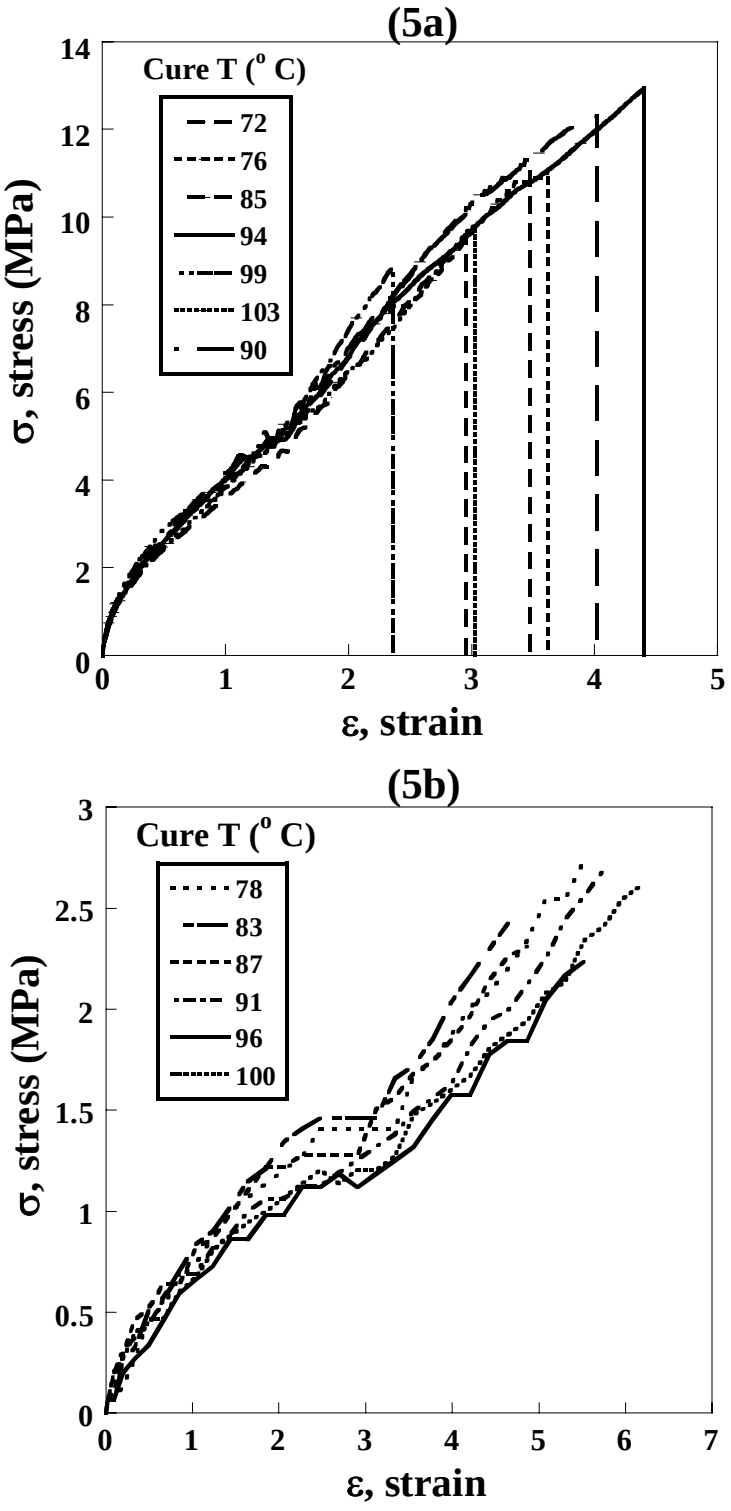

Figure 5.5: Stress-Strain curves for a *T*-gradient SPUU library at different cure temperatures. Library was cured at 95 mole % stoichiometry for 6h.

significant effect at low strain rate (1 mm/s). Since cure *T* primarily influences hard domain H-bonding (Fig 1) and distribution (Fig 5.5), significant differences at low strain rates are not expected, since the flexibility of the soft segments dominates mechanical response. However, at high strain rate the soft segments have considerably less time to relax during deformation, and the stress is influenced strongly by differences in the strength and distribution of urea hard domains. Both the high and slow strain rate curves show three nonlinear regions characteristic of elastomers under tension, e.g., the initial elastic rise, a plateau region probably induced by nonaffine deformation, and an upturn in slope indicative of strain-induced crystallization.[16-17] The low density of data points recorded in the high-throughput measurements prevents further detailed comparisons between the slow and fast deformation curves. The trends in Figures 5.5a and 5.5b are repeatable by impacting multiple rows on the same *T* gradient film, as well as on 2 additional libraries prepared at identical conditions. Fig 5.6 shows that the elongation at break and impact energy (area under the σ vs. ε curve from Fig 5.4a) pass through a maximum at 94 ^{o}C, which corresponds to the cure *T* yielding the best microphase-separated morphology (AFM, Fig 5.4) and at which bidentate H-bonds dissociate (FTIR, Fig 5.4).

SEM observations of the impact surfaces were analyzed to elucidate the failure mode at different cure temperatures. As shown in figure 5.7, all fractured surfaces were rough and contained micrometer-sized fragments, with no dramatic differences in farcture surface with cure temperature. The surface roughness and presence of fragments is indicative of a blunt tear with a brittle failure. This conclusion of a brittle failure is

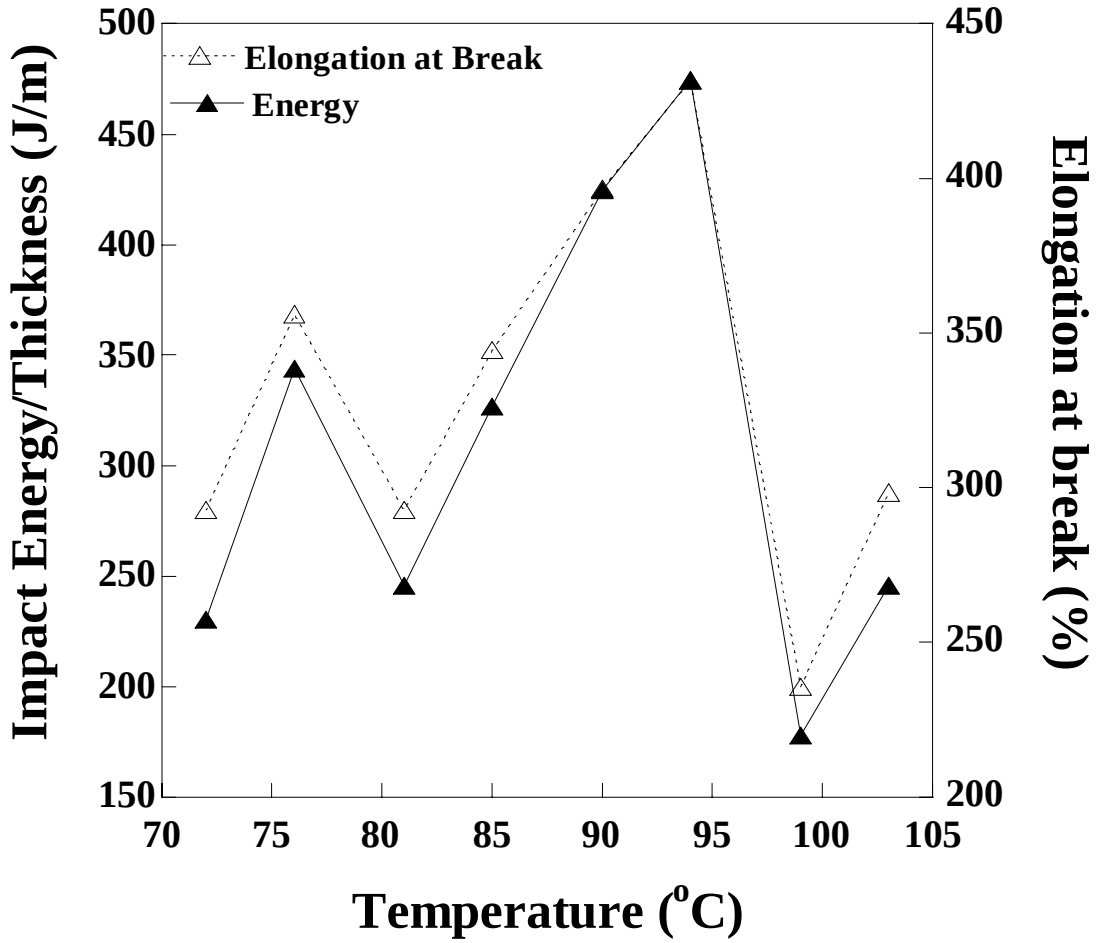

Figure 5.6: Thickness corrected impact energy and elongation at break versus cure temperature for a temperature gradient SPUU library.

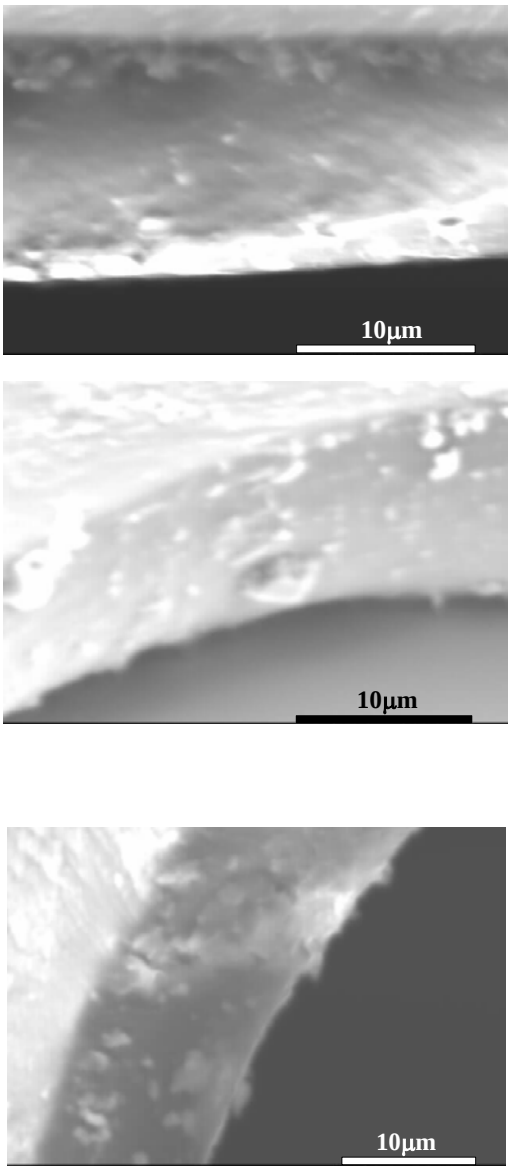

Figure 5.7: SEM images of the fracture surfaces for the temperature gradient SPUU library at impacted at 0.9 m/s; cured at 95 mole % stoichiometry for 6h.

supported by Figure 5.5a. These correlations suggest a structure-property relationship between crosslink density, interurea H-bonding, fracture surface roughness and mechanical strength of SPUU elastomers.

Care must be taken in comparing the results from biaxial characterization to conventional uniaxial tensile tests. The biaxial modulus (slope σ vs. ε) is predicted to be twice Young's modulus measured in uniaxial tension.[16] We verified this for the high-throughput apparatus using 100 μm thick polyethylene films, which gave a biaxial modulus of 12 MPa and a uniaxial modulus of 5.7 MPa, a ratio of 2.1. In addition the ultimate strength of materials measured in biaxial tension differs from uniaxial, with some materials giving higher strengths and others giving lower strengths in biaxial mode. These variations are dependent upon Poisson's ratio,[16] strain-rate, failure mode (brittle vs. ductile) and the presence of crack initiation sites.[17] The *T*-gradients could induce gradients in structure or chemistry that introduce artifacts. However, comparison between uniform and *T*-gradient samples yields the same spectra and mechanical properties. Based upon work with microphase-separating block copolymers,[10] we expect these artifacts to occur only for large gradients in which significant *T*-changes (those producing observable changes in microstructure) occur on the same lengthscale as microstructures (≈1 μm). The 1 °C/mm *T*-gradient used here leads to a 0.001 °C variation over 1 μm, well within the 0.1 °C accuracy of our heating stage.

5.4 CONCLUSIONS

We report the measurement of structure-mechanical property relationships using high-throughput mechanical, spectroscopic and microscopic measurements on *T*-gradient combinatorial SPUU polymer libraries. Impact results were correlated to the phase-separated morphology and degree of interurea H-bonding, with an optimum strength in mechanical properties at a cure *T* of 94 ^{o}C. At low strain rates, the effect of cure *T* had little effect, indicating that the primary determinant of *T*-dependence appears to be the structure and distribution of hard-domains that dominate the high-strain rate mechanical response.

5.5 REFERENCES

(1) Paik Sung, C. S.; Hu, C. B.; Wu, C. S., Properties of Segmented Poly(urethaneureas) Based on 2,4-Toluene Diisocyanate. **1**. Thermal Transitions, X-ray Studies, and Comparison with Segmented Poly(Urethanes). *Macromolecules* **1980,** 13, 111.

(2) Teo, L.-S.; Chen, C.-Y.; Kuo, J.-F., Fourier Transform Infrared Spectroscopy Study on Effects of Temperature on Hydrogen Bonding in Amine-Containing Poly(urethane-urea)s. *Macromolecules* **1997,** 30, 1793.

(3) Wang, C. B.; Cooper, S. L., Morphology and Properties of Segmented Polyether Polyurethaneureas. *Macromolecules* **1983,** 16, 775.

(4) Xiu, Y. Y.; Zhang, Z. P.; Wang, D. N.; Ying, S. K.; Li, J., Hydrogen Bonding and Crystallization Behaviour of Segmented Polyurethaneurea: Effects of Hard Segment Concentration. *Polymer* **1992,** 36, (6), 1335.

(5) Ning, L., De-Wing, W., Sheng-Kang, Y., Crystallinity and Hydrogen Bonding of Hard Segments in Segmented Poly(urethaneurea) Copolymers. *Polymer* **1996,** 37, (16), 3577.

(6) Paik Sung, C. S.; Smith, T. W., Properties of Segmented Polyether Poly(urethaneureas) Based on 2,4-Toluene Diisocyanate. 2. Infrared and Mechanical Studies. *Macromolecules* **1980,** 13, 117.

(7) Meredith, J. C., Karim, A., Amis, E.J., Combinatorial Methods for Investigations in Polymer Materials Science. *MRS Bulletin* **2002,** 27, (4), 330.

(8) Meredith, J. C.; Karim, A.; Amis, E. J., High-Throughput Measurement of Polymer Blend Phase Behavior. *Macromolecules* **2000,** 33, (16), 5760.

(9) Meredith, J. C.; Smith, A. P.; Karim, A.; Amis, E. J., Combinatorial Materials Science for Polymer Thin-Film Dewetting. *Macromolecules* **2000,** 33, (26), 9747.

(10) Smith, A. P.; Douglas, J. F.; Meredith, J. C.; Amis, E. J.; Karim, A., Combinatorial Study of Surface Pattern Formation in Thin Block Copolymer Films. *Phys. Rev. Lett.* **2001,** 87, (1), 15503.

(11) Sormana, J.-L., Meredith, J.C., High-Throughput Dynamic Impact Characterization of Polymer Films. *Mater. Res. Innov.* **2003,** 7, (5), 295.

(12) Garrett, J. T., Runt, J., Microphase Separation of Segmented Poly(urethane urea) Block Copolymers. *Macromolecules* **2000,** 33, 6353.

(13) Garrett, J. T.; Siedlecki, C. A.; Runt, J., Microdomain Morphology of Poly(urethane urea) Multiblock Copolymers. *Macromolecules* **2001,** 34, 7066.

(14) Magonov, S. N., Elings, V., Papkow, V.S, AFM Studies of Thermotropic Structural Transitions in Poly(diethylsiloxane). *Polymer* **1997,** 38, (2), 297.

(15) McLean, R. S.; Sauer, B. B., Tapping-Mode AFM Studies Using Phase Detection for Resolution of Nanophase in Segmented Polyurethanes and Other Block Copolymers. *Macromolecules* **1997,** 30, 8314.

(16) Extrand, C. W.; G.ent, A. N., Strength Under Various Modes of Deformation. *Int. J. Fracture* **1991,** 48, (4), 281.

(17) Gent, A. N., Strength of Elastomers. In *Science and Technology of Rubbers*, Eirich, F. R., Ed. Academic Press: London, **1978**.

CHAPTER 6

SYNTHESIS OF NOVEL SEGMENTED POLYURETHANEUREA NANOCOMPOSITES USING REACTIVE LAPONITE® PARTICLES

A novel class of polymer/silicate nanocomposites based on segmented polyurethaneurea was prepared by reacting a polydiisocyanate with reactive Laponite® particles. These reactive Laponite® particles contain surface-active free amines that allow chemical bond formation between the polymer and the particle, thereby increasing the particle dispersion. Adding reactive Laponite® particles to the polymer resulted in significant simultaneous improvement in both tensile strength and elongation at break. In particular, tensile properties were optimum at a particle concentration of 1 wt. %, with a nearly 200 % increase in tensile strength, and a 40 % increase in elongation at break, compared to pristine segmented polyurethaneurea. This improvement is attributed to the nearly uniform dispersion of exfoliated Laponite® platelets (25 – 30 nm) in the polymer matrix as shown by TEM. At a particle concentration of 3 wt. %, TEM showed aggregated Laponite® platelets (160 – 180 nm), leading to a reduction in tensile strength. These aggregated platelets could be acting as weak points in the material where stress can concentrate, and also as nucleating sites for hard domain crystallization, rather than providing reinforcement for the polymer. The properties of nanocomposites prepared with non-reactive Laponite® and reactive Cloisite®-Na (Montmorillonite) particles (100 – 1000 nm) were compared with nanocomposites made with reactive Laponite® at a particle concentration of 1 wt. %. Nanocomposites made with reactive Laponite®

particles are superior in strength compared to nanocomposites made with non-reactive Laponite® and reactive Montmorillonite particles. This may be an indication that both particle size and strength of the polymer-particle interactions are important in achieving improvement in the mechanical properties of polymer/silicate nanocomposites.

6.1 INTRODUCTION

Dispersions of nanometer size silicates in polymers have become commonplace in materials research. This is because these nanocomposites have demonstrated significant improvement in mechanical, thermal and barrier properties, compared to pristine polymers.[1, 2] Most synthesis routes involve physical mixing of layered silicate particles with the polymer in solution or melt, and rely on the penetration of the polymer chains between the silicate layers to form intercalated and/or exfoliated nanocomposites. In the early 90's, Toyota researchers demonstrated the enhancement of mechanical and thermal properties of Nylon 6 by dispersing nanometer size clay particles in the polymer matrix.[3-6] Since then, many polymer/silicate nanocomposite systems[1, 2] have been investigated, including polyurethane[7-18] and polyurethaneurea[19] nanocomposite systems.

Segmented polyurethaneurea (SPUU) elastomers are block copolymers consisting of alternating rubbery (soft) and glassy or crystalline (hard) segments. The hard and soft segments undergo microphase separation due to the incompatibility of the two segments. Phase separation is influenced by the polarity and size difference between segments, hydrogen bonding between hard segments to form hard domains, composition and cure temperature. The study of SPUU elastomers has attracted tremendous attention because

of their superior elasticity and strength compared to polyurethanes[20], and their many applications in coatings, textile and other consumer products.

The mechanical, thermal, gas and water permeability properties of SPUU depend on their two-phase morphology.[21-24] The soft segment, which contributes elasticity is usually composed of low molecular weight (500 -5000 g/mol) polyester or polyether diol, and the hard segment, which is the urea reaction product between a diisocyanate and a diamine, provides physical crosslinks that act as reinforcing fillers for the soft matrix. SPUU elastomers have excellent elastic properties, but they are permeable to water and air, and the hard domains tend to disintegrate at temperatures greater than 200 ^{o}C. Due to the immense potential applications of these materials, it is desired to improve the mechanical, thermal and barrier properties of these materials, without sacrificing elasticity and strength.

One way of possibly improving the mechanical, thermal and barrier properties of SPUU elastomers is by dispersing silicate particles in the matrix of the polymer to make SPUU/silicate nanocomposites. To observe improvement in properties, it is imperative to have nanometric dispersion of the silicate layers in the polymer matrix to give intercalated and/or exfoliated microstructure. Intercalated nanocomposites consist of well-ordered multilayers with alternating polymer-silicate layers and a repeat distance of few nanometers, and exfoliated nanocomposites consist of individual nanometer-thick silicate layers suspended in the polymer matrix.[25] Silicate particles are hydrophilic, with a large net negative charge and positive counter-ions on the surface, which make them incompatible with organophilic polymers. The dispersion of silicates in polymers is

facilitated by organic modification of the silicate surfaces through ion-exchange reactions with organic cations.

To our knowledge, there are limited literature citations that address the synthesis and characterization of polyurethaneurea nanocomposites.[19] These nanocomposites were prepared by physically mixing a solution containing organically modified non-reactive Montmorillonite particles with pre-made polyurethaneurea in solution. This resulted in intercalated nanocomposites that showed an increase in mechanical properties and a decrease in water vapor permeability compared to pure polyurethaneurea at a clay content of 6 volume %. The tensile modulus, strength and elongation to break, all increased with clay content. This observation is contrary to conventional polymer composites, wherein adding particles often increases the tensile modulus, but decreases the elongation to break.

The primary objective of this research endeavor is to prepare novel polyurethaneurea nanocomposites using reactive Laponite® RD particles as the filler. Laponite® ($Na^{+}_{0.7}[(Si_8Mg_{5.5}Li_{0.3})O_{20}(OH)_4]^{0.7-}$) is a synthetic layered silicate that hydrates in water to give a homogenous dispersion of exfoliated nanometric disks (1 nm x 25 nm).[26-28] Laponite® is hydrophilic, with a net negative surface charge, indicated by its chemical formula, and has positive counter-ions (e.g. Na^{+}, Ca^{2+}) on the surface. Laponite® is made organophilic through ion exchange reactions with organic cations. The organic cations are prepared by treating a monoamine and a diamine with excess HCl. Organic modification with diamine resulted in Laponite® particles with a free reactive amine group tethered to the surface of the particle. This free amine can react with the isocyanate in the prepolymer to form urea linkages, allowing chemical

incorporation of the Laponite® particle in to the polymer matrix. On the other hand, particles modified with monoamines do not have a free reactive amine group. Hence, the resulting nanocomposites will rely heavily on physical mixing to achieve good dispersion of the particles in the polymer. In addition to demonstrating the differences between nanocomposites prepared with reactive versus non-reactive Laponite®, it is important to benchmark these effects by comparison to nanocomposites made with Cloisite®-Na (Montmorillonite), the particle of choice in most polymer/silicate nanocomposite systems. Cloisite®-Na was modified with a diamine to produce reactive Montmorillonite particles. Compared to Laponite®, natural Montmorillonite does not exfoliate very easily in water, and has a lateral size of about 100 – 1000 nm, compared with 25 nm for Laponite®.

6.2 EXPERIMENTAL SECTION

6.2.1 Materials and Synthesis of Polyurethaneurea/Silicate Nanocomposites

Laponite® RD and Cloisite®-Na, having a cationic exchange capacity of 75 mequiv/100 g and 92.6 mequiv/100 g respectively, were obtained from Southern Clay Products Inc., and used as received. Trimethylene glycol di-*p*-aminobenzoate (Air Products and Chemicals Inc., Versalink® 740-M, 98.2 % purity) and 4-Benzylaniline (Lancaster Synthesis, 98 % purity) were treated with excess concentrated HCl to form ammonium salt. For the remainder of this chapter, trimethylene glycol di-*p*-aminiobenzoate and 4-Benzylaniline will be referred to as diamine and monoamine respectively. The excess HCl was allowed to evaporate under ambient conditions for several days until a dry salt resulted. The dried monoamine and diamine salts were

crushed in a mortar and washed several times with tetrahydrofuran (VWR, ACS grade) to remove all untreated amines. The tetrahydrofuran (THF) used was dried over molecular sieves to remove water prior to use. These "amine-free" ammonium salts were dried under ambient condition, producing salts that were used to modify Laponite® RD and Cloisite®-Na.

The modification process involved cationic exchange reaction between one of the ammonium salts and either Laponite® RD or Cloisite®-Na. Three different exchange reactions were performed: (1) monoamine salt and Laponite® RD, (2) diamine salt and Laponite® RD, and (3) diamine salt and Cloisite® Na. For exchange reaction 1, 6 g of Laponite® RD was added to 600 g of deionized water and stirred with a magnetic stirring bar under ambient conditions for approximately 30 min. The clear Laponite® RD dispersion was slowly added to a solution of excess monoamine salt (twice the exchange capacity of Laponite® RD) in water. The mixture was stirred with a magnetic stirring bar at room temperature for 24 h. The monoamine modified Laponite® RD (*MAML*) particles were collected by centrifuge and repeatedly washed and centrifuged until all halide anions were removed. The absence of halide anions was confirmed by adding $AgNO_3$ to the supernatant solution after centrifuge to form white AgCl precipitate. The washed particles were dried under ambient conditions for several days and subsequently crushed in a mortar and screened with a 325-mesh sieve. This procedure was repeated for exchange reactions 2 and 3 with minor alterations. Both exchange reactions 2 and 3 were carried out at 60 ^{o}C. In exchange reaction 3, Cloisite®-Na was dispersed in hot water at 60 ^{o}C, prior to addition to the diamine salt solution. Exchange reactions 2 and 3 produced diamine modified Laponite® RD (*DAML*) and diamine modified Cloisite®-Na

(*DAMC*) respectively. The organic surface content of the modified particles was determined by the difference in weight between pure and modified particles from thermogravimetric analysis in the temperature range from 150 – 1000 ^{o}C.

Diamine modified particles are expected to have one free amine, capable of reacting with the isocyanate in the toluene diisocyanate (tetramethylene glycol) prepolymer (Air Products and Chemicals Inc., AIRTHANE PET-90A, $M_w \approx 2350$, NCO functionality = 2.0, mass % NCO = 3.58 %). SPUU nanocomposites were prepared by first mixing a 1 wt. % modified particle dispersed in THF with melted prepolymer to give a 30 wt. % prepolymer solution. All reactions, except otherwise stated, were carried out at 95 mole % of the stoichiometric amount of diamine needed to react with all the isocyanate groups present in the prepolymer, and cured in a vacuum oven at 90 ^{o}C for 6h. The extra diamine needed to achieve the desired stoichiometry was added from a 30 wt. % stock solution in THF. The reacting mixture was stirred with a magnetic stirring bar for several minutes and the solution was coated on a Piranha cleaned silicon wafer (Silicon Inc.) using a knife coater.[29-31] SPUU/DAML nanocomposites were prepared at different DAML weight fractions to optimize DAML concentration in the nanocomposites. Optimum particle concentration was based on uniaxial tensile strength and elongation at break. SPUU nanocomposites were also prepared using MAML and DAMC at the optimum particle weight fraction (1 wt. %) obtained with DAML nanocomposites. Pure SPUU samples were prepared using 30 wt. % solutions of pure prepolymer and diamine in THF

6.2.2 Characterization

All nanocomposite film thicknesses were measured by visible-near infrared interferometry (Stellar Net EPP 2000).[32] Thermogravimetric analysis (TGA) was carried out using a TA Instrument (Model # TGA-Q500) at a heating rate of 10 ^{o}C/min in a nitrogen atmosphere from 30 ^{o}C to 1000 ^{o}C. FT-IR spectra of monoamine, diamine, Laponite® RD, Cloisite®-Na, MAML, DAML, DAMC and nanocomposite films were recorded at a resolution of 4 cm^{-1} under ambient condition using a Bruker IRscope II. The sample area was purged with dry air to prevent the appearance of atmospheric water bands in the spectra. All spectra were corrected for thickness and a peak separation and analysis software package (Peakfit® 4.11, Jandel Scientific) was used to resolve the bands in the carbonyl (ν = 1630 – 1760 cm^{-1}) region to obtain the relative ratios of the peak areas, assuming Gaussian peak shapes. Wide angle X-ray Diffraction (WAXD) patterns of the unmodified particles (Laponite® RD and Cloisite®-Na), modified particles (MAML, DAML and DAMC) and the nanocomposite films were recorded using a PANanalytical X'Pert diffractometer with nickel-filtered Cu Kα (λ = 0.15406 nm) radiation in a sealed tube, operated at 40 kV and 200 mA. The diffraction patterns were obtained from 2 to 15 degrees at a scan rate of 6 deg/min. Mechanical properties of Pure SPUU and SPUU nanocomposite films were determined using a commercial uniaxial tensile apparatus (INSTRON® 5842) at a strain rate of 30 mm/min. Differential Scanning Calorimetry (DSC) measurements of the nanocomposites were performed on a Seiko DSC220C at a heating rate of 5 ^{o}C/min over the temperature range of -90 to 320 ^{o}C in a nitrogen atmosphere. Transmission electron microscopy (TEM) was performed using a JEOL® JEM-100CX II at an acceleration voltage of 100 kV. Samples (ca. 10 – 20 nm

thick) for TEM were prepared by putting a drop of solution on a PELCO® support film of formvar, stabilized with carbon on 200-mesh copper grid (Ted Pella, Inc.). The grids were place in a vacuum oven at 90 ^{o}C for 6h, prior to imaging.

6.3 RESULTS AND DISCUSION

FT-IR spectra of all modified particles were analyzed to determine the presence of reactive amine (N-H) groups that can serve as chain extenders in the synthesis of the nanocomposites. Figure 6.1 shows an FT-IR spectra in the amine region (ν = 3100 – 3500 cm^{-1}) of the modified particles, monoamine, diamine, Laponite® RD and Cloisite®-Na. The presence of amine peaks in the spectra of DAML and DAMC indicates that modification of the particles with a diamine produces reactive particles with a surface-active free amine. These free amine groups can react with isocyanate groups from the prepolymer to form urea linkages, thereby chemically incorporating the particle in to the matrix of the polymer. Particles obtained from modification with monoamine (MAML) did not show any peak in the amine region. Since the MAML particles do not have any reactive functional groups tethered to the particle, nanocomposites made with MAML will rely primarily on physical mixing of the particles with the polymer, and on the penetration of the polymer chains between the silicate layers, to achieve good dispersion of the particles. Nanometric dispersion of the silicate particles is necessary in order to achieve significant improvement in mechanical and thermal properties.

TGA graphs used to determine the amount of monoamine or diamine tethered to the particles are shown in Figure 6.2. It was estimated that nearly 20 % of the total weight of DAML was contributed by the tethered diamine, 17 % of the total of weight of

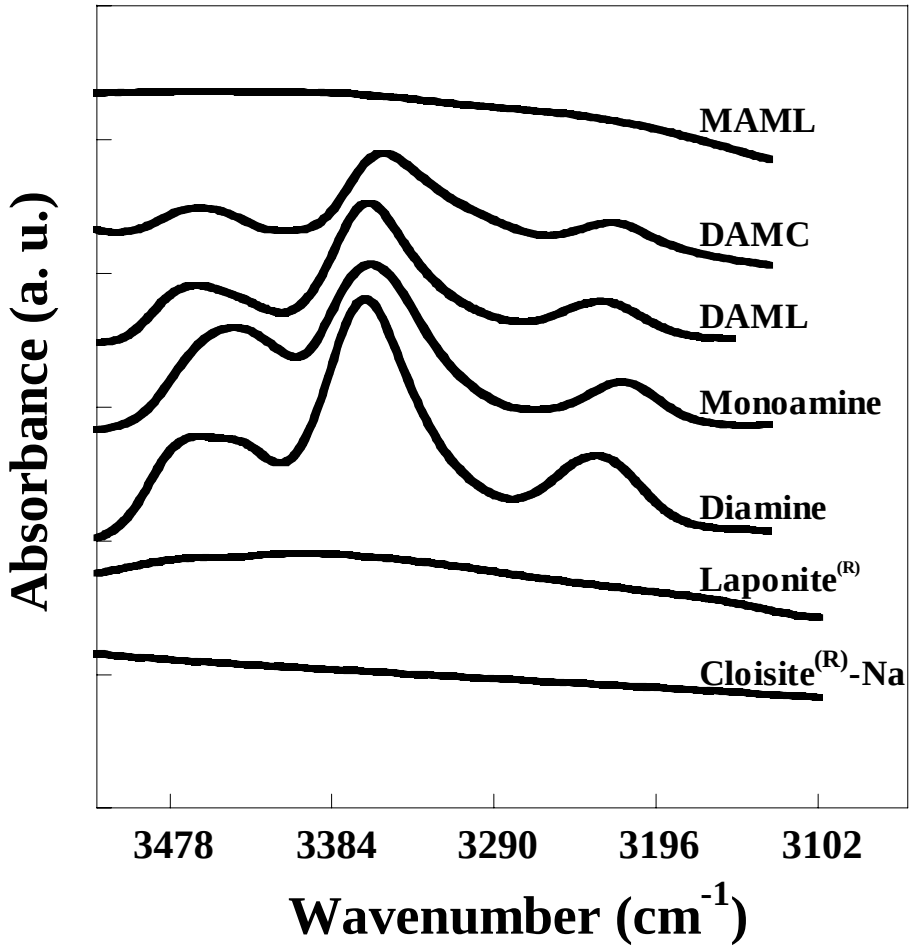

Figure 6.1: FT-IR spectra in the amine region demonstrating successful modification of silicate particles to produce reactive and non-reactive silicates; reactivity is indicated by the presence of free amine peaks in the spectra.

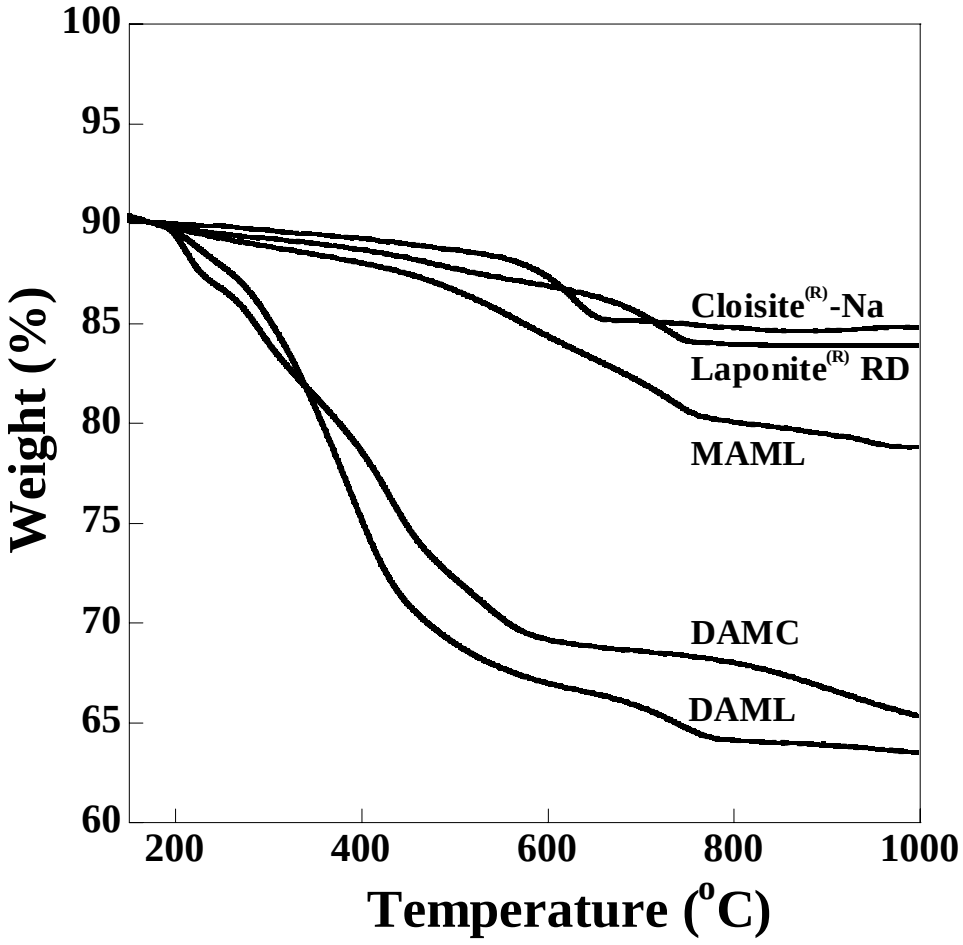

Figure 6.2: TGA curves of unmodified and modified silicates.

DAMC was contributed by the tethered diamine, and 10 % of the total weight of MAML was contributed by the monoamine over this temperature range (150 ^{o}C to 1000 ^{o}C). The pure monoamine and diamine (TGA graphs not included) showed complete decomposition in this temperature range. The difference in weight loss between the modified particles and the corresponding unmodified particle was used to determine the mass fraction of amine attached to the surface of the particles. This quantity was needed to determine the amount of excess diamine needed for a desired total diamine stoichiometry.

WAXD spectroscopy is a powerful technique commonly used to study the regular lattice arrangement of crystals. The gallery spacing of silicates, d, can be determined using Bragg's equation: $n\lambda = 2d \sin(\theta)$, where λ is the wavelength of the x-ray (1.5406 Å) used and θ is the diffraction angle. WAXD patterns of Laponite®, Cloisite®-Na, and the modified particles, MAML, DAML and DAMC are presented in Figure 6.3. The diffraction pattern corresponding to Cloisite®-Na has a peak centered about $2\theta = 7.5^{o}$. This peak position corresponds to a d_{001} spacing of 11.7 Å . The modified Cloisite®-Na particle, DAMC, shows a diffraction peak at $2\theta = 4.5^{o}$ (d_{001}= 19.6 Å), a shift towards lower angle when compared with pure Cloisite®-Na. This shift implies an expansion of the gallery spacing as a result of modification with diamine salt. The WAXD patterns of pure Laponite® and modified Laponite® particles, MAML and DAML show no discernable differences. A broad peak ($2\theta = 1.5 - 9^{0}$) is observed in all three diffraction patterns, as shown in Figure 6.3. The nature of the peaks can be attributed to the very low crystallinity and very small aspect ratio of Laponite® compared to other silicates such as Montmorillonite. Contrary to clays with large aspect ratio that tend to aggregate in a

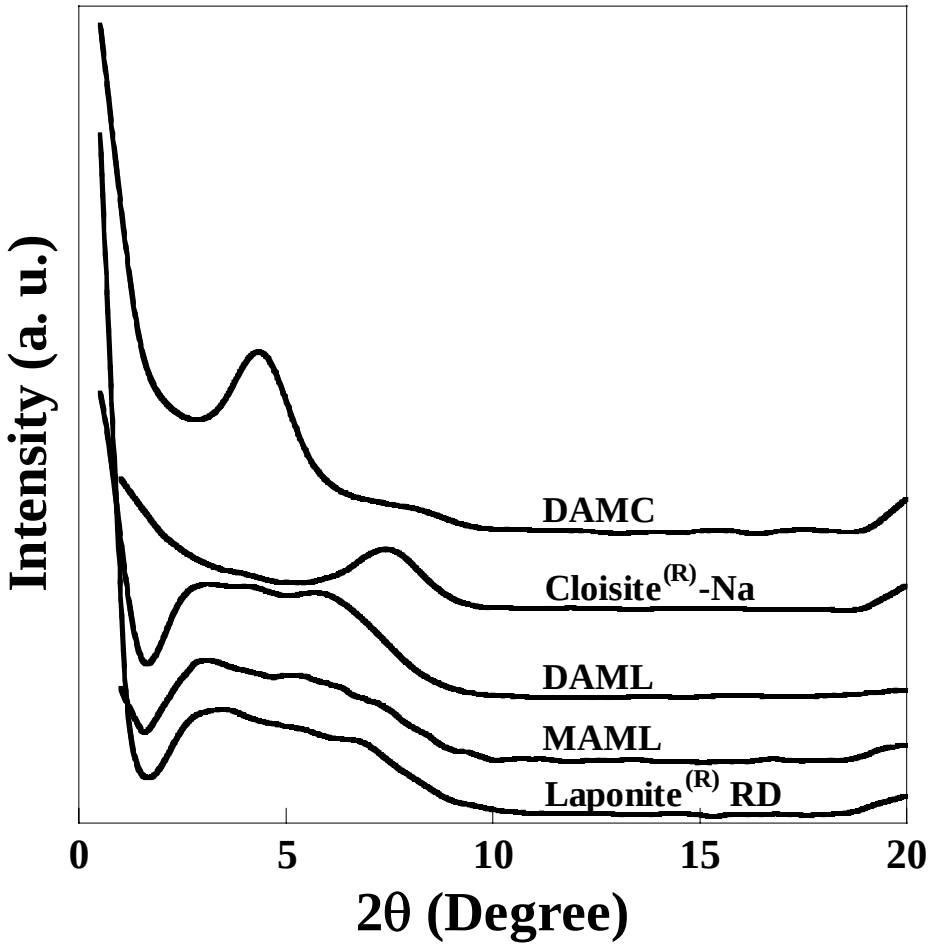

Figure 6.3: WAXD patterns of unmodified and modified silicates.

face-to-face lamellar fashion, Laponite® has a tendency to form partially delaminated disordered aggregates through edge-to-face interactions.[33, 34] Also, the cations in Laponite® that participate in ion exchange reactions are present at the surface of the silicate. Hence, all ion exchange with organic salts takes place at the surface, rather than inside the gallery. This could possibly explain why the position of the peak does not change (shift to lower angles) after modification.

Figure 6.4 shows FT-IR spectra in the carbonyl region of pure SPUU and SPUU/silicate nanocomposites prepared with different modified particles and at different particle concentrations. Detailed classification of the peak positions in the carbonyl region can be found in an earlier publication.[32] The position of the peaks found in the spectrum of the pure SPUU is identical to those found in the nanocomposites. This suggests that the presence of the particles does not significantly affect the chemical structure of SPUU. Hydrogen bonding in SPUU, especially favorable urea-urea hydrogen bonding between hard segments to form hard domains, improves the phase-separated morphology of these materials. In general, stabilization of nanoscale hard domains results in materials with enhanced mechanical and thermal properties.[24, 35, 36] The amount of urea-urea hydrogen bonding in all samples were determined using the equations developed by Ning.[37] The degree of urea-urea hydrogen bonding for all nanocomposites were similar to the amount estimated in pure SPUU. This might indicate uniform nanometric dispersion of exfoliated silicate layers of modified particles in the matrix of the polymer.[7]

WAXD patterns for the pure SPUU and several SPUU nanocomposites are presented in Figure 6.5. The diffraction peaks found in the curves for the modified

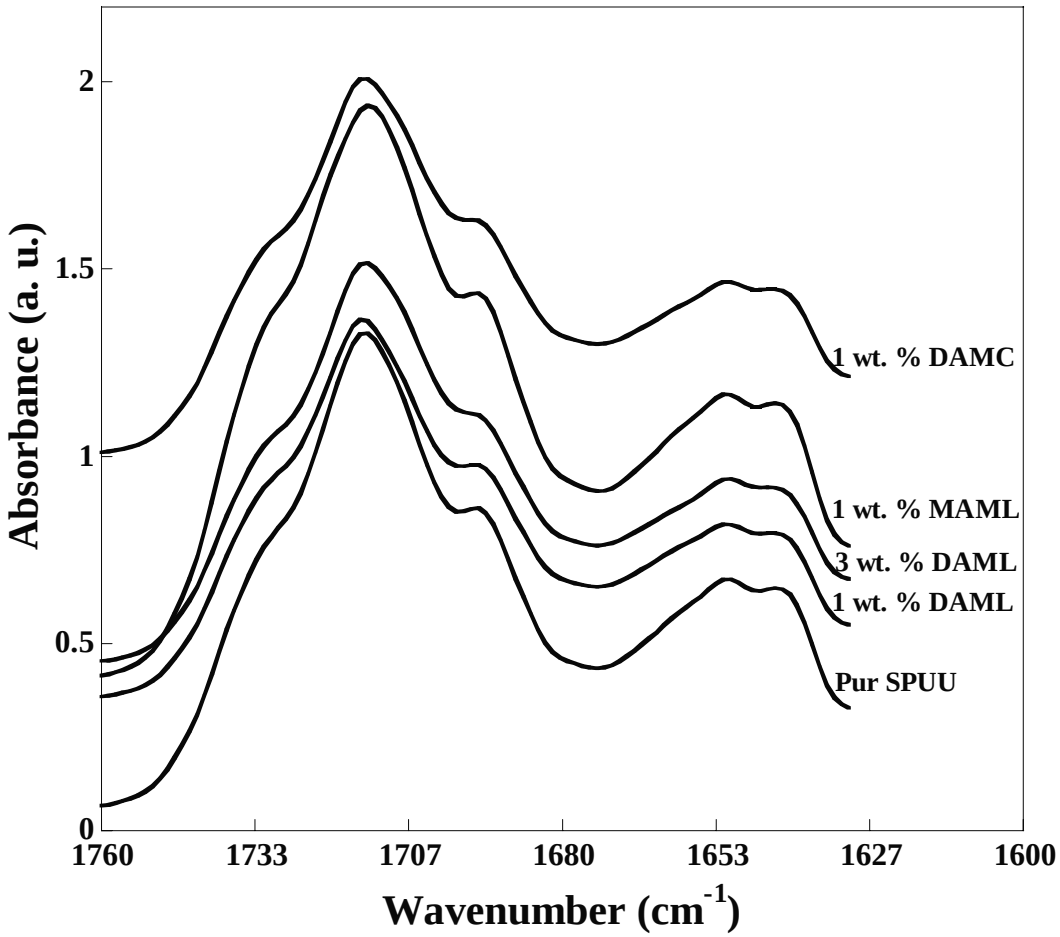

Figure 6.4: FT-IR spectra of pure SPUU and SPUU nanocomposites prepared with different particles at the specified particle concentration.

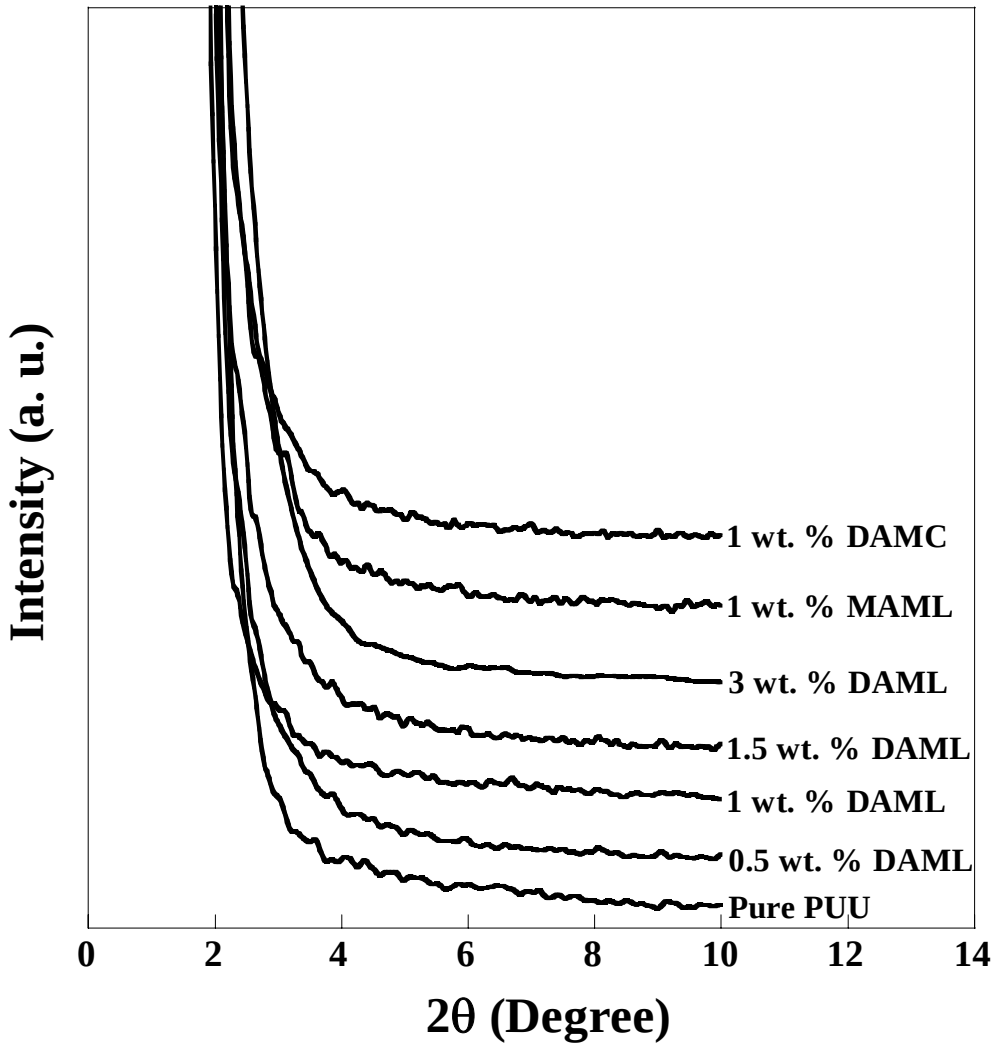

Figure 6.5: WAXD patterns of pure SPUU and SPUU nanocomposites prepared with different particles, at the specified particle concentration.

particle (see Figure 6.3) are not present in the result nanocomposites. This indicates that the parallel registry in the modified particles has been destroyed, suggesting exfoliation of silicate layers in the matrix of the polymer.[38]

TEM has emerged as a routine technique for probing the morphology of polymer/silicate nanocomposites. TEM provides information about the intercalated and exfoliated state of the silicate layers in the matrix of the polymer. The level of dispersion of the silicate layers in the polymer matrix, nanometric or otherwise, can also be discerned from TEM micrographs. TEM micrographs of pristine SPUU and SPUU/DAML nanocomposites prepared with 1 wt. % DAML and 3 wt. % DAML are presented in Figure 6.6. The micrograph of the pure SPUU shows a clear image (Figure 6.6a), without any characteristic feature, due to the low electron density of the polymer, and the lack of contrast between the hard and soft phases. Nanocomposites prepared with 1 wt. % DAML contained particles resembling circular disks, with a diameter of about 25-30 nm (Figure 6.6b). The shape and size of these particles suggests that they could be platelets of Laponite® dispersed in the matrix of the polymer.[26-28, 39] These particles are nicely dispersed in a disordered fashion in the polymer matrix, indicating an exfoliated morphology. Increasing the concentration of DAML to 3 wt. % in the nanocomposites resulted in aggregation of Laponite® platelet to give particles with a diameter of about 160-180 nm as shown in Figure 6.6c. The aggregated particles at 3 wt. % DAML were also randomly dispersed in the matrix of the polymer. The exfoliated morphology at 1 wt. % DAML is corroborated by the absence of diffraction peaks in the WAXD pattern displayed in Figure 6.5.

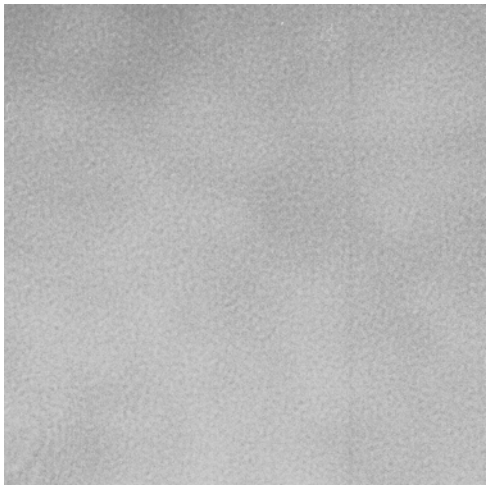

6a.

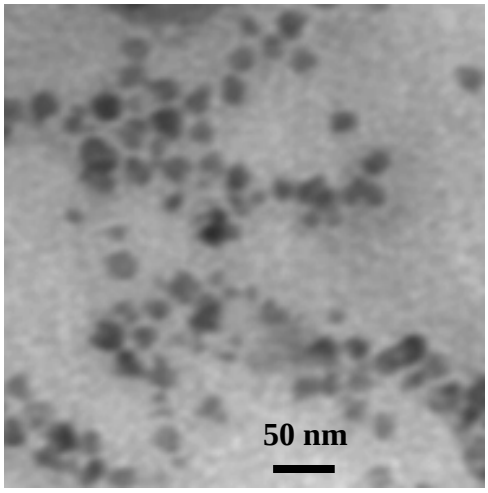

6b.

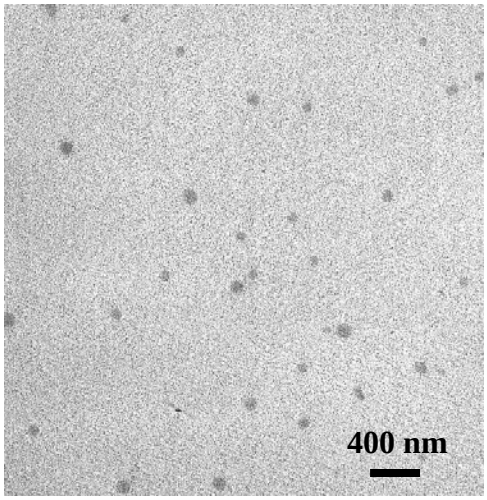

6c.

Figure 6.6: TEM micrographs of (6a) pure SPUU, (6b) 1 wt. % DAML nanocomposite, and (6c) 3 wt. % DAML nanocomposite.

Figures 6.7 and 6.8 show DSC thermographs of pure SPUU and SPUU nanocomposites prepared with different particles at the specified particle weight fraction. The thermal properties are summarized in Table 6.1. The soft segment glass transition temperatures of all nanocomposites are nearly identical to the glass transition temperature

Table 6.1: Mechanical Properties and Endothermic Transitions for SPUU and SPUU Nanocomposites.

Nanocomposite Composition (wt. % Silicate)	Tensile Strength[a] (MP)	Elongation at Break[a] (%)	Modulus, E_{100}[a] (MPa)	T_g[b] (^oC)	Endo[c] 1 Peak, T (^oC)	Endo[c] 2 Peak, T (^oC)
Pure SPUU	16.7 ± 1.7	501.3 ± 34.3	11.1 ± 1.2	-72	192	274
0.5 wt. % DAML	33.0 ± 3.9	604.4 ± 17.3	11.7 ± 0.9	-70	192	270
1 wt. % DAML	48.8 ± 1.4	715.5 ± 40.2	11.6 ± 1.0	-70	197	265
1.5 wt. % DAML	26.4 ± 2.7	607.8 ± 37.0	10.4 ± 1.4	-69	192	273
3 wt. % DAML	16. ± 2.1	642.0 ± 35.0	10.9 ± 0.8	-68	188	277
1 wt. % MAML	22.1 ± 3.0	734.0 ± 20.9	13.2 ± 1.4	-68	189	271
1 wt. % DAMC	28.4 ± 0.7	750.7 ± 35.5	10.3 ± 0.6	-71	189	285

[a] Error represents a 95 % confidence level from at least 3 samples.
[b] Soft segment glass transition temperature.
[c] Endo means endothermic.

of pure SPUU. This suggests that the dispersed silicates do not have a significant effect on the free volume of SPUU. A common feature of all the thermographs in Figures 6.7 and 6.8 is the presence of two melting endotherms: one at about 190 ^oC and another at about 270 ^oC. The presence of multiple endotherms in segmented polyurethane block copolymers has been attributed to melting of hard segments with different crystal lengths, and microphase mixing of hard domains with different thickness.[40-43] In general, trends observed with polyurethanes are expected to hold true for SPUU.[44] The high temperature

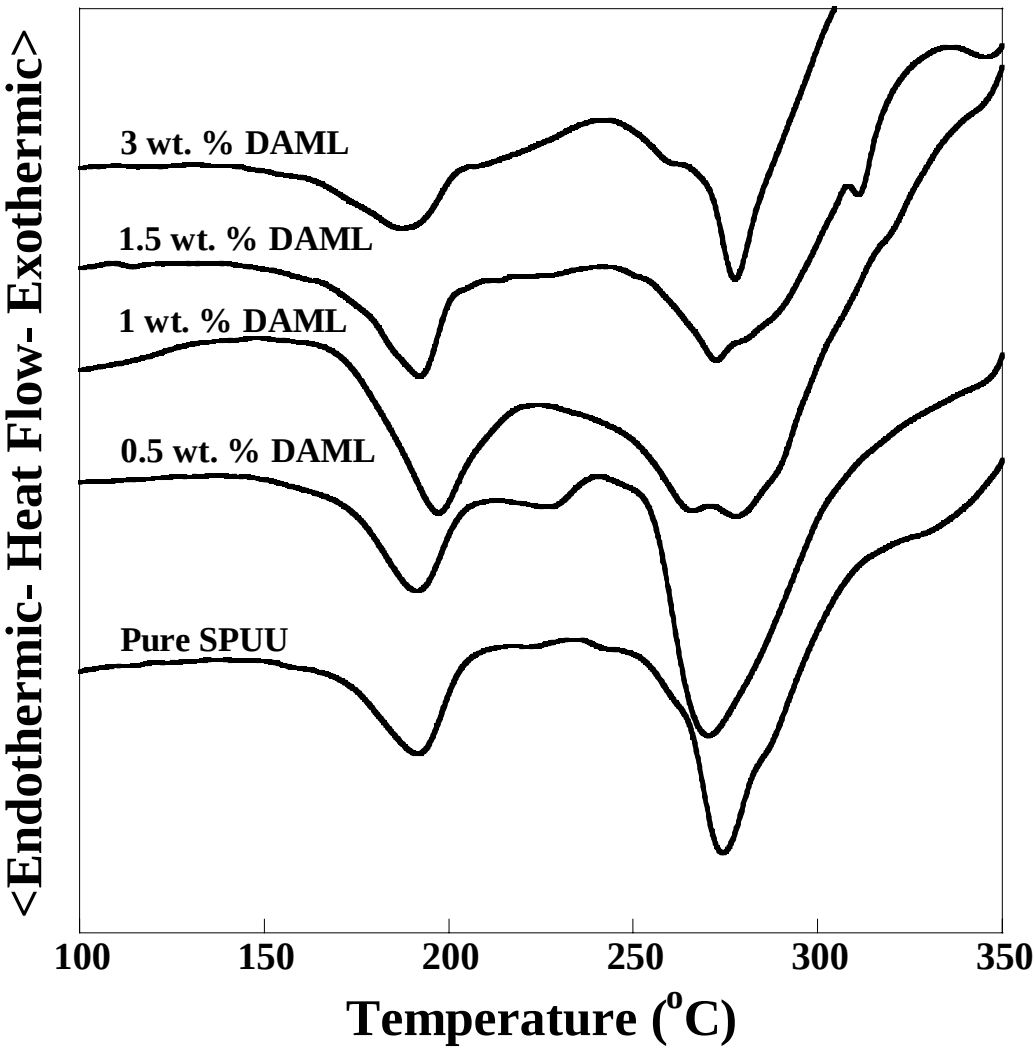

Figure 6.7: DSC curves comparing the melting and crystallization behavior of pure SPUU and SPUU nanocomposites prepared at different concentrations of DAML.

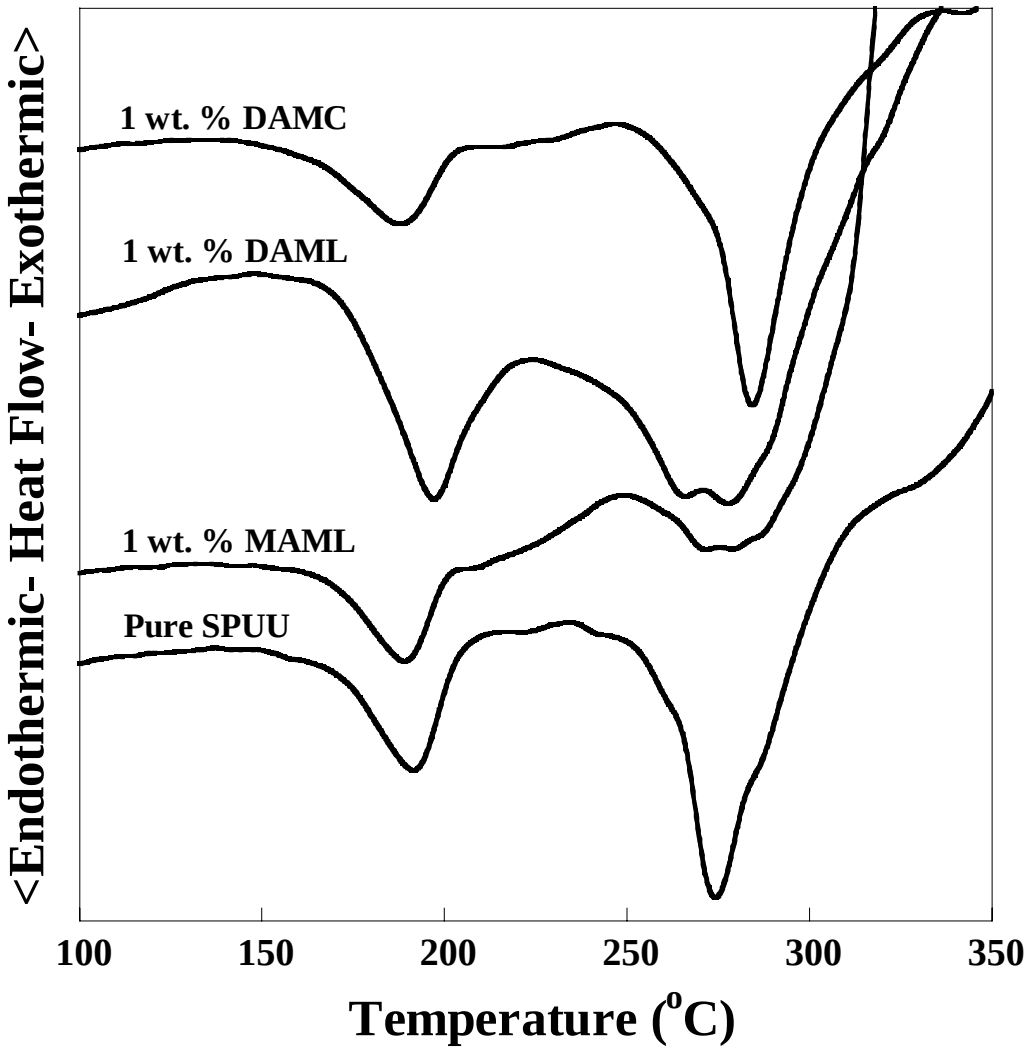

Figure 6.8: DSC curves comparing the melting and crystallization behavior of pure SPUU and SPUU nanocomposites prepared with different modified silicates at the same silicate concentration of 1 wt. %.

endotherm at 270 ^{o}C represents the melting of the crystalline hard domain. The endotherm at 190 ^{o}C could be associated with melting of hard domains with different thicknesses, or hard segment mixed in the soft phase of the polymer. The difference in the two endotherms could serve as a measure of the degree of phase mixing. Larger temperature differences between the endotherms indicate a more phase-separated morphology. As shown in Figure 6.7 and Table 6.1, the degree of phase mixing initially increases with increase in DAML concentration, and is maximum in nanocomposites containing 1 wt. % DAML. At DAML concentrations of 1 and 1.5 wt. %, the endotherms around 270 ^{o}C appear broader, compared to the pure SPUU, and also contain multiple peaks. This may suggest reduction in hard domain crystallization and the formation of crystals with different sizes. Nanocomposites containing 3 wt. % DAML show a very sharp endotherm at about 278 ^{o}C, similar to pure SPUU, suggesting enhancement in hard domain crystallization compared with nanocomposites at 1 and 1.5 wt. % DAML. TEM images shown in Figure 6.6 show that nanocomposites with 3 wt. % DAML contain aggregated silicate with an average diameter of about 160-180 nm. These aggregated silicates could be acting as nucleating sites for hard domain crystallization.

Figure 6.8 compares the thermographs obtained from nanocomposites prepared with all three modified particles at the same particle concentration of 1 wt. %. Maximum phase mixing is observed in composite made with DAML (see Figure 6.8 and Table 6.1), and both nanocomposites made with modified Laponite® RD show broad endotherms with multiple peaks near 270^{o}C indicates multiple types of hard domains. Hard domains resulting from hydrogen bonding between urea linkages directly attached to the particle are expected to show a slightly different thermal behavior when compared to hard

domains resulting from hydrogen bonding between urea groups that are further away from, or not attached to the particle. Nanocomposites prepared with modified Montmorillonite show enhanced crystallization compared to nanocomposites made with other particles. Cloisite®-Na, commonly referred to as Montmorillonite is comprised of 1 nm thick platelets with diameters of about 100 – 1000 nm. These larger particles, compared to unaggregated Laponite® RD platelets, could potentially serve as nucleating sites, thus explaining the improved hard domain crystallization observed in nanocomposites prepared with Cloisite®-Na.

Uniaxial tensile stress-strain curves for pure SPUU and SPUU nanocomposites with different amounts of DAML are presented in Figure 6.9 and the mechanical properties are summarized in Figure 6.10 and Table 6.1. Both the tensile strength and elongation at break increased with increase in DAML concentration up to a maximum at a DAML concentration of 1 wt. %. Simultaneous increase in both tensile strength and elongation at break has been reported for polyurethane[15] and polyurethaneurea[19] nanocomposites prepared with non-reactive modified Montmorillonite . Enhancement in strength is directly related to the presence of dispersed silicate layers in the polymer. Improvement in elongation at break may be attributed in part to the plasticizing effect of the gallery oniums and to their contribution to the formation of dangling chains, but also to conformational effects at the silicate-matrix interface.[1, 15] The mechanical property trends observed in Figures 6.9, 6.10, and Table 6.1 can be explained by the morphological information provided by DSC and TEM. Figure 6.7 and Table 6.1 show maximum phase mixing in nanocomposites prepared at 1 wt. % DAML, suggesting highest possible interaction of the 25 - 30 nm diameter silicate with the polymer matrix,

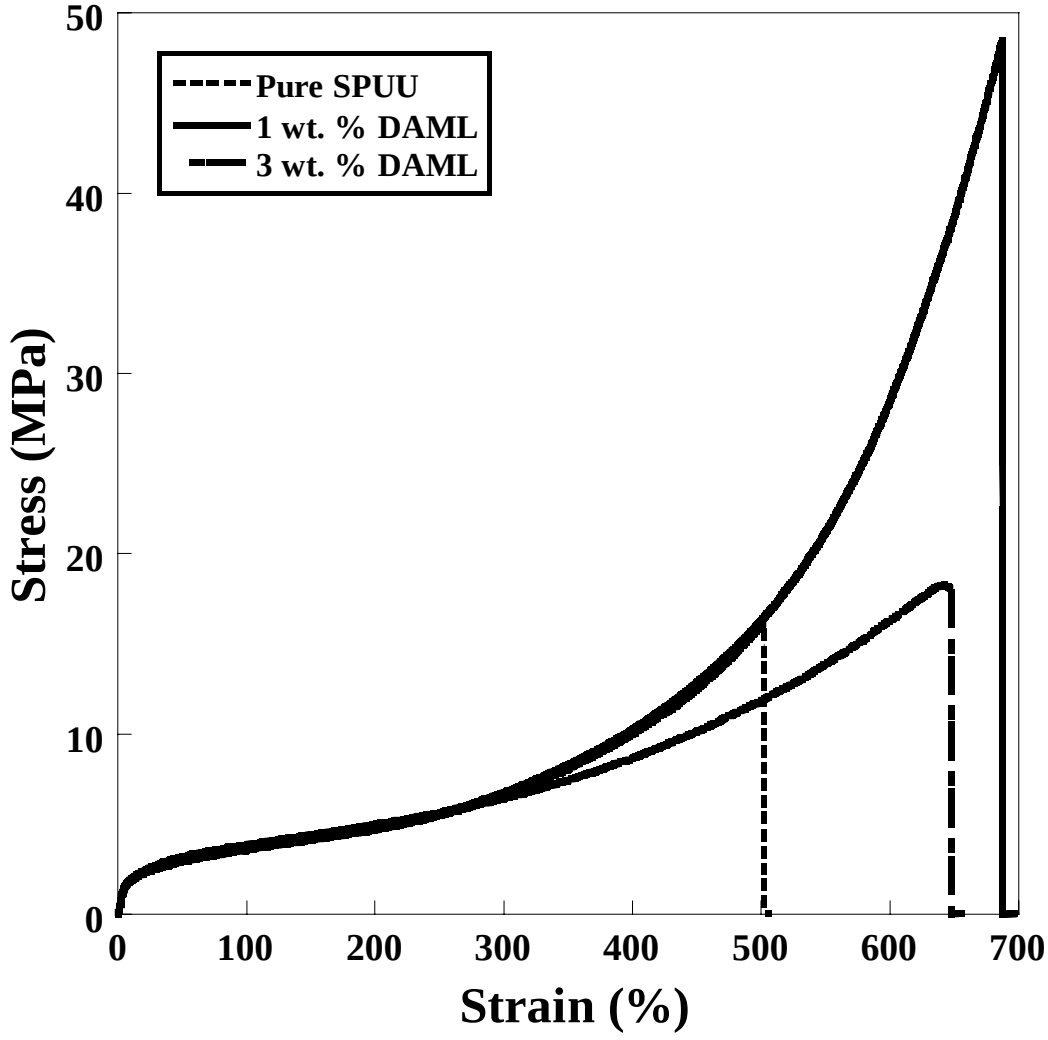

Figure 6.9: Stress-Strain curves for pure SPUU and SPUU nanocomposites prepared with DAML at 1 and 3 wt. % DAML.

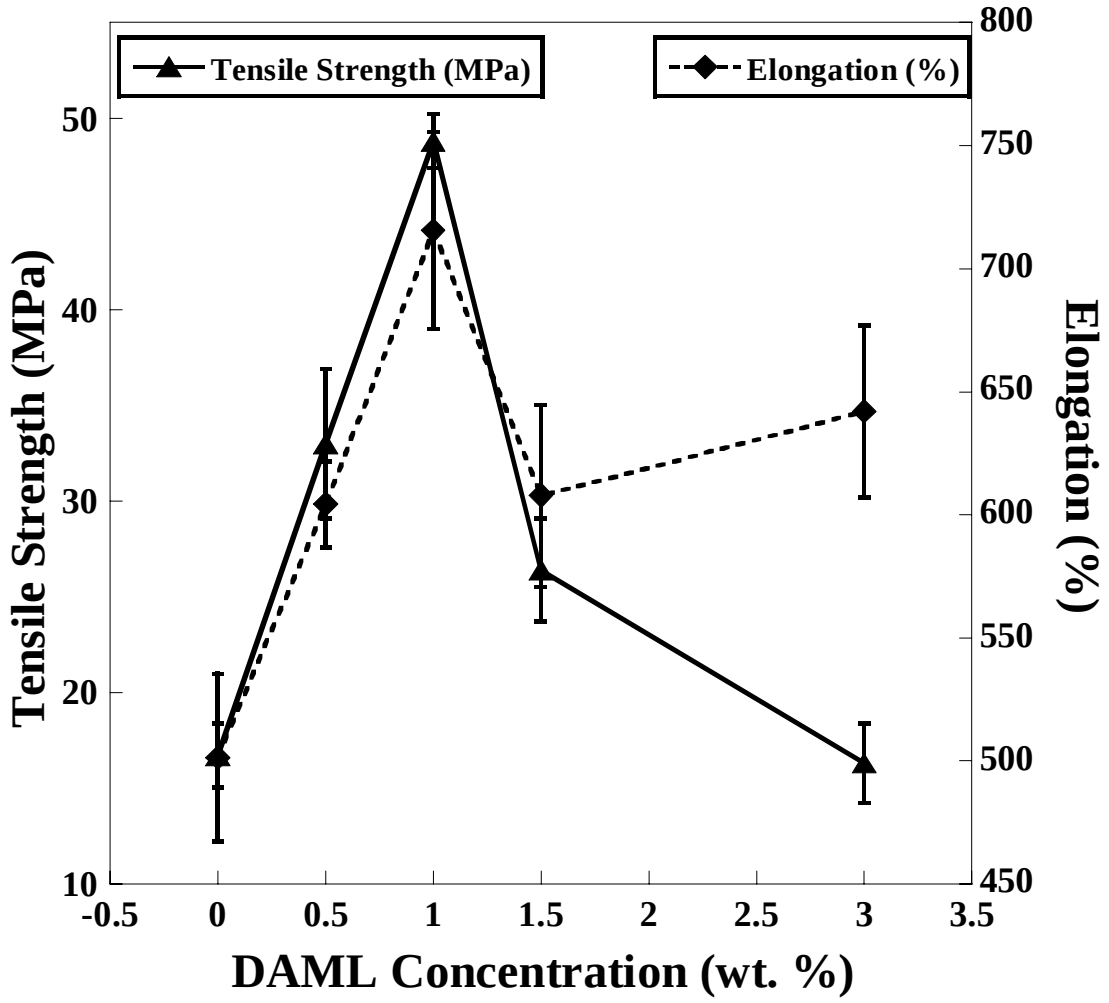

Figure 6.10: Mechanical properties of SPUU and SPUU Nanocomposites prepared at different DAML concentrations.

compared with other nanocomposites. Nanocomposites with smaller particles and stronger particle-polymer interactions typically exhibit significant improvement in properties compared to nanocomposites with larger particles and weaker interactions.[45] Increasing the DAML concentration to 3 wt. %, resulted in larger, aggregated silicate particles (160 - 180 nm), as shown in Figure 6.6c. It is likely that these aggregated particles are acting as nucleating sites rather than mechanical reinforcement for the polymer matrix. Improvement in hard domain crystallization at 3 wt. % DAML compared to 1 and 1.5 wt. % DAML is evident by comparing the corresponding hard domain melting endotherm in Figure 6.7.

On of the main goals of this research was to demonstrate the difference between the mechanical properties of nanocomposites prepared with reactive versus non-reactive silicates. Since Montmorillonite has been the particle of choice in polyurethane/silicate nanocomposite synthesis[7, 10, 13-15, 18, 19] we aimed also to demonstrate the effect of particle type (Laponite® or Cloisite®-Na) on the mechanical properties of SPUU nanocomposites. Figure 6.11 shows tensile stress-strain curves for nanocomposites prepared with reactive Laponite® (DAML) and non-reactive Laponite® (MAML) particles at 1 wt. % particle concentration. Also included in Figure 6.11 are the tensile stress-strain curves for pure SPUU and SPUU nanocomposite made with 1 wt. % reactive Montmorillonite (DAMC). The mechanical properties in Figure 6.11 are summarized in Table 6.1. At very low elongations, up to 200%, the shape of the stress-strain curves for pure SPUU, 1 wt. % DAML nanocomposite and 1 wt. % DAMC nanocomposite are almost superimposable. However, the curve corresponding to 1 wt. % MAML reaches a slightly higher stress in the same elongation range. At low elongations, the resistance to deformation is primarily

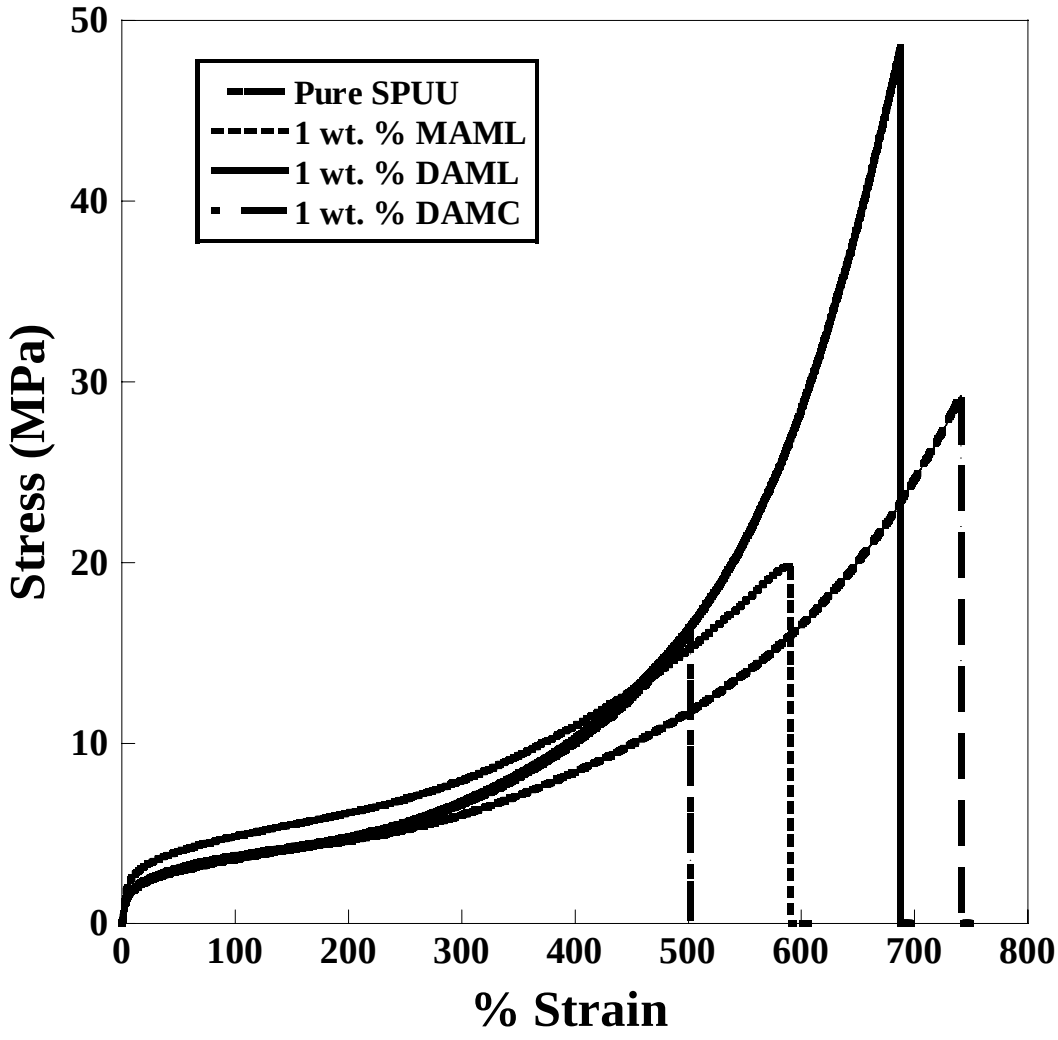

Figure 6.11: Stress-Strain curves of pure SPUU nanocomposites prepared with different modified silicates at the same silicate concentration of 1 wt. %.

due to straightening of soft-segment chains in pure SPUU and nanocomposites made with reactive silicates. In the case of the non-reactive silicate, MAML, the presence of the hard inorganic silicates that are not chemically bonded to the polymer matrix contributes to the overall resistance to deformation. The increase in strength in MAML at low elongation is small because a very small amount of silicate (1 wt. %) is added to the polymer.

6.4 CONCLUSIONS

Segmented polyurethaneurea nanocomposites were successfully prepared using reactive and non-reactive silicates. The silicates used in this study, Laponite® and Cloisite®-Na, were made reactive through ion exchange reactions with ammonium salts of a diamine. Non-reactive Laponite® particles were also prepared through ion exchange reaction with ammonium salt of a monoamine. The presence of a free amine attached to the surface of the silicate was verified by FT-IR for reactive particles. Non-reactive particles did not show any peaks in the amine region of their FT-IR spectrum. SPUU nanocomposites were made using reactive Laponite® particles at different particle concentration. FT-IR spectra for all nanocomposites made with reactive Laponite® did not show any significant shift in peak position in the carbonyl region, indicating that the presence of the particles does not influence on the chemical structure of the polymer. No peaks were observed in WAXD patterns for all nanocomposites. This implies that the particles were probably exfoliated. Exfoliated morphology was corroborated by TEM for nanocomposites made with 1 wt. % DAML. The tensile strength and elongation at break were optimum at a particle concentration of 1 wt. % for reactive Laponite® particles. A

two-fold increase in tensile strength, and more than 40 % increase in elongation was obtained, compared with pure SPUU. At 1 wt. % particle loading, TEM micrograph showed a uniform dispersion of individual Laponite® platelets of about 25 - 30 nm in diameter. Increasing the particle concentration above 1 wt. % led to significant reduction in tensile strength. Nanocomposites prepared at 3 wt. % showed aggregated Laponite® particles with a diameter of about 160-180 nm. DSC thermographs showed improved hard domain crystallization at 3 wt. %, suggesting that these aggregated particles could be acting as nucleating site for hard domain crystallization. These aggregates could also serve as weak points in the material where stress can concentrate, thus explaining the reduction in strength at a particle loading greater than 1 wt. Nanocomposites prepared with reactive Laponite® exhibit higher tensile strength when compared with nanocomposite made with non-reactive Laponite® and reactive Cloisite®-Na. Since Cloisite®-Na is significantly larger than Laponite®, and reactive particles, through chemical bonding have a stronger interaction with the polymer compared to non-reactive particles, one can conclude that the mechanical properties of SPUU/silicate nanocomposites are influenced by both the polymer-particle interactions and size particle size.

6.5 REFERENCES

(1) Alexandre M. and Dubois, P., Polymer-Layered Silicate. *Mater. Sci. and Eng.* **2000,** 28, 1.

(2) LeBaron, P. C., Wang, Z., Pinnavaia, T.J., Polymer-Layered Silicate Nanocomposites: An Overview. *Applied Clay Science* **1999,** 15, 11.

(3) Kojima, Y., Usuki, A., Kawasumi, M., Okada, A., Fukushima, Y., Mechanical Properties of Nylon 6-Clay Hybrid. *J. Mater. Res.* **1993,** 8, (5), 1185.

(4) Kojima, Y., Usuki, A., Kawasumi, M., Okada, A., Kurauchi, T., Kamigaito, O., Synthesis of Nylon 6-Clay Hybrid by Montmorillonite Intercalated with e-Caprolactam. *J. Polym. Sci., Part A: Polym. Chem* **1993,** 31, 983.

(5) Usuki, A., Kojima, Y., Kawasumi, M., Okada, A., Fukushima, Y., Synthesis of Nylon 6-Clay Hybrid. *J. Mater. Res.* **1993,** 8, (5), 1179.

(6) Usuki, A., Kawasumi, M., Kojima, Y., Okada, A., Kurauchi, T., Swelling Behavior of Montmorillonite Cation Exchanged for ω-Amino Acids by ε-Caprolactam. *J. Mater. Res.* **1993,** 8, (5), 1174.

(7) Chen, T.-K.; Tien, Y.-I.; Wei, K.-H., Synthesis and Characterization of Novel Segmented Polyurethane/Clay Nanocomposites. *Polymer* **2000,** 41, 1345.

(8) Hu, Y., Song, L., Xu, J., Yang, L., Chen, Z., Fan, W., Synthesis of Polyurethane/Clay Intercalated Nanocomposites. *Colloid Polym. Sci.* **2001,** 279, 819.

(9) Ma, J.; Zhang, S.; Qi, Z., Synthesis and Characterization of Elastomeric Polyurethane/Clay Nanocomposites. *J. App. Polym. Sci.,* **2001,** 82, 1444.

(10) Ni, P., Li, J., Suo, J., Li, S, Novel Polyether Polyurethane/Clay Nanocomposites Synthesized with Organic-Modified Montmorillonite as Chain Extenders. *J. App. Polym. Sci.* **2004,** 94, 534.

(11) Petrovic, Z. S., Javni, I., Waddon, A., Banhegyi, G., Structure and Properties of Polyurethane-Silica Nanocomposites. *J. App. Polym. Sci.,* **2000,** 76, 133.

(12) Song, M., Hourston, J. D., Yao, K. J., Tay, J. K. H., Ansarifar, M. A., High Performance Nanocomposites of Polyurethane Elastomer and Organically Modified Layered Silicate. *J. App. Polym. Sci.* **2003,** 90, 3239.

(13) Tien, Y.-I., Wei, K.H., Hydrogen Bonding and Mechanical Properties in Segmented Montmoillonite/Polyurethane Nanocomposites of Different Hard Segment Ratios. *Polymer* **2001,** 42, 3213.

(14) Tien, Y.-I., Wei, K.H., High-Tensile-Property Layered Silicates/Polyurethane Nanocomposites by Using Reactive Silicate as Psuedo Chain Extenders. *Macromolecules* **2001,** 34, 9045.

(15) Wang, Z.; Pinnavaia, T. J., Nanolayer Reinforcement of Elastomeric Polyurethane. *Chem. Mater.* **1998,** 10, 3769.

(16) Xu, R., Manias, E., Synder, A. J., Runt, J., Low Permeability Biomedical Polyurethane Nanocomposite. *J. Biomed. Matter. Res.* **2003,** 64A, 114.

(17) Yao, K. J., Song, M., Hourston, D.J., Luo, D.Z., Polymer/Layered Clay Nanocomposites: 2 Polyurethane Nanocomposites. *Polymer* **2002,** 42, 1017.

(18) Zhang, X., Xu, R., Wu., Z., Zhou, C., The Synthesis and Characterization of Polyurethaneure/Clay Nanocomposite. *Polym. Int.* **2003,** 52, 790.

(19) Xu, R.; Manias, E.; Snyder, A. J.; Runt, J., New Biomedical Poly(urethaneurea)-Layered Silicate Nanocomposites. *Macromolecules* **2001,** 34, 337.

(20) Paik Sung, C. S.; Hu, C. B.; Wu, C. S., Properties of Segmented Poly(urethaneureas) Based on 2,4-Toluene Diisocyanate. **1**. Thermal Transitions, X-ray Studies, and Comparison with Segmented Poly(Urethanes). *Macromolecules* **1980,** 13, 111.

(21) Garrett, J. T., Runt, J., Microphase Separation of Segmented Poly(urethane urea) Block Copolymers. *Macromolecules* **2000,** 33, 6353.

(22) Garrett, J. T.; Siedlecki, C. A.; Runt, J., Microdomain Morphology of Poly(urethane urea) Multiblock Copolymers. *Macromolecules* **2001,** 34, 7066.

(23) Miller, J. A.; Lin, S. B.; Hwang, K. K. S.; Wu, K. S.; Gibson, P. E.; Cooper, S. L., Properties of Polyether-Polyurethane Block copolymers: Effects of Hard Segment Length Distribution. *Macromolecules* **1985,** 18, 32.

(24) Wang, C. B.; Cooper, S. L., Morphology and Properties of Segmented Polyether Polyurethaneureas. *Macromolecules* **1983,** 16, 775.

(25) Vaia, R. A., Giannelis, E.P., Polymer Melt Intercalation in Organically-Modified Layered Silicates: Model Predictions and Experiments. *Macromolecules* **1997,** 30, 8000.

(26) Avery, R. J., Ramsay, J.D.F, Colloidal Properties of Synthetic Hectorite Clay Dispersions. II. Light and Small Angle Neutron Scattering. *J. Colloidal and Interface Science* **1985,** 109, (2), 448.

(27) Ramsay, J. D. F., Colloidal Properties of Synthetic Hectorite Clay Dispersions. I. Rheology. *J. Colloidal and Interface Science* **1985,** 109, (2), 441.

(28) Rosta, L., von Gunten, H. R., Light Scattering Characterization of Laponite Sols. *J. Colloidal and Interface Science* **1990,** 134, 397.

(29) Meredith, J. C., Karim, A., Amis, E.J., Combinatorial Methods for Investigations in Polymer Materials Science. *MRS Bulletin* **2002,** 27, (4), 330.

(30) Meredith, J. C.; Karim, A.; Amis, E. J., High-Throughput Measurement of Polymer Blend Phase Behavior. *Macromolecules* **2000,** 33, (16), 5760.

(31) Meredith, J. C.; Smith, A. P.; Karim, A.; Amis, E. J., Combinatorial Materials Science for Polymer Thin-Film Dewetting. *Macromolecules* **2000,** 33, (26), 9747.

(32) Sormana, J.-L., Meredith, J.C., High-Throughput Discovery of Structure Property Relationships for Segmented Polyurethaneureas. *Macromolecules* **2004,** 37, (6), 2186.

(33) Herrera, N. N., Letoffe, J.-M., Putaux, J.-L., Laurent, D., Bourgeat-Lami, E., Aqueous Dispersions of Silane-Functionalized Laponite-Clay Platelets. A First Step Toward the Elaboration of Water-Based Polymer/Clay Nanocomposites. *Langmuir* **2004,** 20, 1564.

(34) Herrera, N. N., Letoffe, J.-M., Reymond, J.-P., Bourgeat-Lami, E., Silylation of Laponite Clay Particles with Monofunctinal and Trifunctional Vinyl Alkoxysilanes. *J. Mater. Chem.* **2005,** 15, 863.

(35) Musselman, S. G.; Santosusso, T. M.; Barnes, J. D.; Sperling, L. H., Domain Structures and Interphase Dimensions in Poly(urethaneurea) Elastomers Using DSC and SAXS. *J. Polym. Sci., Part B: Polym. Phys.* **1999,** 37, 2586.

(36) Paik Sung, C. S.; Smith, T. W., Properties of Segmented Polyether Poly(urethaneureas) Based on 2,4-Toluene Diisocyanate. 2. Infrared and Mechanical Studies. *Macromolecules* **1980,** 13, 117.

(37) Ning, L., De-Wing, W., Sheng-Kang, Y., Cryatallinity and Hydrogen Bonding of Hard Segments in Segmented Poly(urethaneurea) Copolymers. *Polymer* **1996,** 37, (16), 3577.

(38) Tyan, H.-L., Liu, Y.-C., Wei, K.-H., Enhancement of Imidization of Poly(amic acid) through forming Poly(amic acid)/Organoclay Nanocomposites. *Polymer* **1999,** 40, 4877.

(39) Balnois, E., Durand-Vidal, S., Levitz, P., Probing the Morphology of Laponite Clay Colloids by Atomic Force Microscopy. *Langmuir* **2003,** 19, 6633.

(40) Koberstein, J. T. a. G., A.F., Multiple Melting in Segmented Polyurethane Block Copolymers. *macromolecules* **1992,** 25, 5618.

(41) Koberstein, J. T. a. R., T.P., Simultaneous SAXS-DSC Study of Multiple Endothermic Behavior in Polyther-Based Polyurethane Copolymers. *Macromolecules* **1986,** 19, 714.

(42) Martin, D. J., Meijs, G. F., Renwick, G. M., McCarthy, S. J., Gunatillake, P. A., The Effect of Average Soft Segment Length on Morphology and Properties of a Series of Polyurethane Elastomers. I. Characterization of the Series. *J. Appl. Polym. Sci.* **1996,** 62, 1377.

(43) Martin, D. J., Meijs, G. F., Renwick, G. M., McCarthy, S. J., Gunatillake, P. A., The Effect of Average Soft Segment Length on Morphology and Properties of a Series of Polyurethane Elastomers. II. SAXS-DSC Annealing Study. *J. Appl. Polym. Sci.* **1997,** 64, 803.

(44) O'Sickey, M. J.; Lawrey, B. D.; Wilkes, G. L., Structure-Property Relationships of Poly(urethane urea)s with Ultra-low Monol Content Poly(propylene glycol) Soft Segments. I. Influence of Soft Segment Molecular Weight and Hard Segment Content. *J. App. Polym. Sci.,* **2002,** 84, 229.

(45) Nielsen, L. E., Landel, R. F., *Mechanical Properties of Polymers and Composites*. 2nd ed.; Marcel Dekker: New York, **1994**.

CHAPTER 7

CONCLUSIONS AND RECOMMENDATIONS FOR FUTURE STUDY

Combinatorial synthesis and high-throughput screening techniques were combined with conventional one-sample-one-measurement techniques to synthesized segmented polyurethaneurea (SPUU)/Laponite® nanocomposites. Combinatorial synthesis allows a large parameter space to be explored using limited number of samples, and the effect of multiple parameters (synergistic or counteracting) can be explored in 2-D libraries with orthogonal variations in two process parameters. High-throughput screening of the libraries provide useful information about the effect of process parameters on the desired properties. Although Combinatorial synthesis and high-throughput screening techniques can reduce a very complex problem into one that is tractable, conventional one-sample-one-measurement techniques are always necessary to validate results from combinatorial studies.

7.1 CONCLUSIONS

7.1.1 *High-Throughput Screening of Mechanical Properties in Polymer Libraries*

The application of combinatorial methods (CM) as a viable tool for discovering novel polymeric materials or improving the properties of existing materials has gained momentum in both academia and industry in the past five years. With numerous library preparation techniques available (gradient and discrete), the limitation in polymer CM appears to be in the screening and characterization stage. A novel apparatus (*HTMECH*) for characterizing the mechanical property of free-standing gradient polymer films is described in this work.[1, 2] Although intended for characterizing gradient films, this instrument can also be used for characterizing uniform films. This instrument is capable of characterizing polymer films that are 5 – 100 μm thick at a wide range of strain rates, ranging from near-static to high speed (1 m/s) impact. Rapid and accurate characterization of mechanical properties of up to 100 distinct positions on a combinatorial library film can be achieved with this instrument, facilitating the discovery of new materials, or development of structure – mechanical property relationships.

Validation measurements were performed by characterizing different classes of polymers, from glassy to thermoplastic elastomers. Force-time profiles obtained from characterizing poly methacrylate (PMMA), polyamide, polyethylene, segmented polyurethaneurea (SPUU) and polyetheramide demonstrates the instrument's sensitivity to changes in chemistry and structural differences. Reproducibility of measurements obtained with the *HTMECH* was determined by characterizing 25 neighboring point on a uniform polyethylene film. Results obtained from this experiment indicate excellent reproducibility with a 95 % confidence level of 2.05 ± 0.11 N in the maximum force

(strength), and also suggests that measurement at one position within a combinatorial library does not affect subsequent measurements at neighboring positions within the same library

The measurements obtained from the *HTMECH* are biaxial in nature. This is a consequence of the geometry of the instrument's design and setup. Geometrically, the *HTMECH* is similar to the shaft-loaded blister test. A basic understanding of the deformation mechanics of the shaft-loaded blister test provides insight in to the deformation of films using the *HTMECH*. It was determined that three types of stresses, namely, bending, tensile and shear, contribute to the overall stress in a film during deformation with the *HTMECH*. The relative contributions of these three stresses depends heavily on a geometric factor, ρ (ratio of indenter diameter to hole diameter). As $\rho \rightarrow 0$, also referred to as the point load condition, tension is the dominant contributor to the total stress in the film, with negligible bending and shear stresses. At higher ρ values, the contribution due to shear becomes significant because of the increased contact area between the indenter and the sample. An optimum value of ρ was determined to be 0.17.

Ideally, operating under point load condition ($\rho \rightarrow 0$) is desired because results can be easily compared with measurements from a commercial instrument like the INSTRON®, which operates primarily in tension. However, the point load condition allows limited number of experiments, making the *HTMECH* invaluable as a tool for high-throughput screening. At $\rho = 0.17$, the shear contributions are negligible and bending contributions are minimized, making tension the dominant stress in the film. Measurements at $\rho = 0.17$ were performed on SPUU films prepared at different

conditions of cure temperature and chain extender composition, and the results compared with measurements obtained from an INSTRON®. This comparison showed a remarkable agreement between the two measurement methods, especially at chain extender composition of 100 mole % stoichiometry. The modulus at 100 % strain for all measurements were calculated, and a strong linear correlation was found between the *HTMECH* the uniaxial INSTRON® results, with a coefficient of $E_{HTMECH} = 1.34E_{UNIAXIAL}$. Remarkably, this correlation coefficient (1.34) is almost equal to the coefficient of 1.375 predicted by Wan and Liao[3] for the analytical solution to the theoretical equations used to determine the mechanical properties of the thin films using the shaft-loaded blister test in the point-load limit ($\rho \rightarrow 0$).

7.1.2 *Combinatorial Synthesis and High-Throughput Screening of Gradient Polymer Libraries*

One of the first examples demonstrating the application of combinatorial synthesis and high-throughput screening of reactive gradient polymer libraries is presented in this dissertation.[4, 5] Reactive gradient libraries of SPUU were synthesized with linear gradients in the chain extender concentration, cure temperature, or both, using the techniques described elsewhere.[6, 7] SPUU represents an ideal system for combinatorial synthesis and high-throughput screening due to the strong dependence of their mechanical properties on cure temperature and chain extender concentration.

Combinatorial libraries of SPUU with continuous linear gradients in chain extender concentration ($60 < \phi < 160$ mole % stoichiometry), cure temperature ($70 < T < 130$ ^{o}C), both were synthesized and characterized. The mechanical properties were characterized using the *HTMECH* described above and the results compared with measurements obtained from an INSTRON®. Mechanical measurements were combined

with structural information from FT-IR, AFM, DSC and SEM to develop structure-mechanical property relationships.

For this particular combination of prepolymer (AIRTHANE® PET-85A, Air Products and Chemicals, M_W = 2500, NCO functionality = 2.0, mass % NCO = 3.3) and chain extender (VERSALINK®, 740-M, Airproducts and Chemicals) used in this thesis, the mechanical properties of SPUU were optimum at a chain extender concentration of 85 mol % stoichiometry, and a cure temperature of 94 ^{o}C. This condition of cure temperature and chain extender concentration produced materials with enhanced phase-separated morphology with hard domains (diameter ~ 110 – 130 nm) nearly uniformly dispersed in the polymer matrix as shown by AFM micrographs. In general, enhancement in phase-separation results in materials with improved strength. FT-IR and DSC also show enhancement in phase-separation at a cure temperature of 94 ^{o}C and chain extender composition of 85 mole % stoichiometry. Analysis of the fracture surfaces of a composition gradient film after high speed (1 m/s) impact with the *HTMECH* suggests a transition from brittle to ductile failure with increase in chain extender composition. These results validate the *HTMECH* as an accurate and effective screening tool for developing mechanical property-structure relationships in gradient combinatorial libraries.

7.1.3 *Segmented Polyurethaneurea/Laponite$^{(R)}$ Nanocomposites*

Novel segmented polyurethaneurea/Laponite® nanocomposites were prepared using reactive Laponite® particles with surface-active free amines. The presence of these surface-active free amines was verified by FT-IR. These surface-active amines facilitated chemical incorporation of the Laponite® particle in the matrix of the polymer through

chemical bond formation between the isocyanate in the prepolymer and the surface amines. SPUU Nanocomposites were prepared at different reactive particle concentration while maintaining the total chain extender stoichiometry at 95 mole % and cured at 90 ^{o}C. These conditions of chain extender stoichiometry and cure temperature were determined from previous combinatorial studies with a similar prepolymer and chain extender combination. The mechanical properties of these nanocomposites were optimum at a particle concentration of 1 wt. %, with a nearly 200 % increase in tensile strength, and a 40 % increase in elongation at break. TEM micrographs show a uniform dispersion of individual Laponite® platelets of about 25-30 nm in diameter at 1 wt. %. Increasing the particle concentration to 3 wt. % led to particle aggregation and a significant reduction in tensile strength.

SPUU nanocomposites were also prepared with non-reactive Laponite® and reactive and reactive Montmorillonite (100 – 1000 nm) to investigate the effect of particle size and polymer-particle interaction on the mechanical properties of SPUU nanocomposites. At 1 wt. % particle loading, nanocomposites prepared with reactive Laponite® have higher tensile strength compared to nanocomposites made with non reactive Laponite® and reactive montmorillonite. These results suggest that the mechanical properties of SPUU nanocomposites are influenced by both particle size and polymer-particle interactions. Smaller particles (Laponite® vs. montmorillonite) with stronger polymer-particle interactions (reactive vs. non-reactive Laponite) through chemical bond formation yielded stronger nanocomposites.

7.2 RECOMMENDATIONS FOR FUTURE STUDY

7.2.1 *Modeling of HTMECH Deformation Mechanics*

Theoretical equations that describe the deformation mechanics of the shaft-loaded blister test have been developed by others using plate and membrane theories.[3, 8, 9] Due to the similarity in geometry between the shaft-loaded blister test and *HTMECH*, these theoretical equations could also be used to understand the deformation mechanics of the *HTMECH*. A central issue in understanding the deformation mechanics of the *HTMECH* is the ability to decouple the individual stress components in a material during deformation. In Chapter 2, these stresses were identified as bending, tensile and shear. Modifying the assumptions in the membrane and plate theories could lead to the development of model equations that describe the bending and tension in *HTMECH* deformation mechanics respectively. Shear contributions could be estimated by incorporating contact mechanics in the final model equations. Such a development could increase the acceptance of the *HTMECH* as an alternative tool for characterizing the mechanical properties of polymer films

7.2.2 *Extension of HTMECH for Measurement of Other Properties and in Different Environmental Conditions*

The *HTMECH* is also capable of measuring other material properties. Specifically, by controlling the rate of data acquisition and the motion of the actuator attached to the sample plate holder, cyclic loading measurements and tensile stress relaxation experiments can be performed using the *HTMECH*. Figures 7.1 and 7.2 show results obtained from cyclic loading and stress relaxation experiments respectively. From

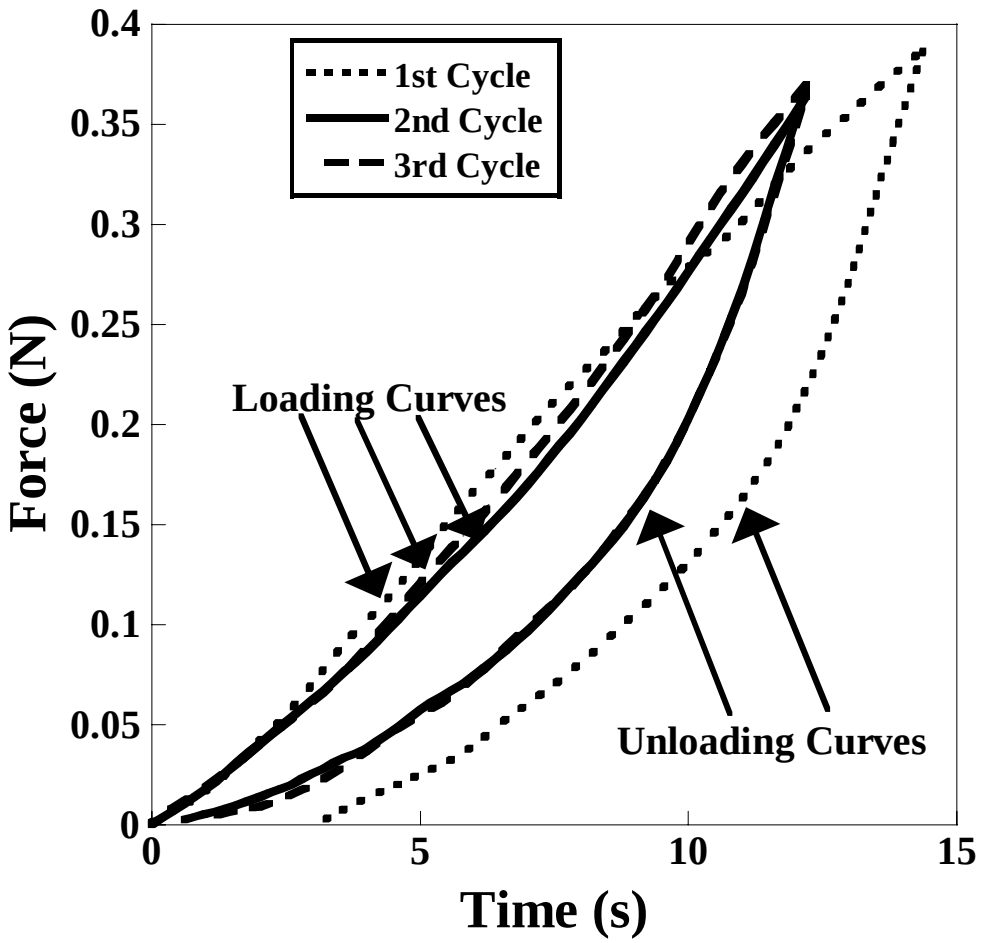

Figure 7.1: Cyclic loading of a segmented polyurethaneurea film using the *HTMECH*; film prepared at 95 mole % stoichiometry, cured at 90 ^{o}C.

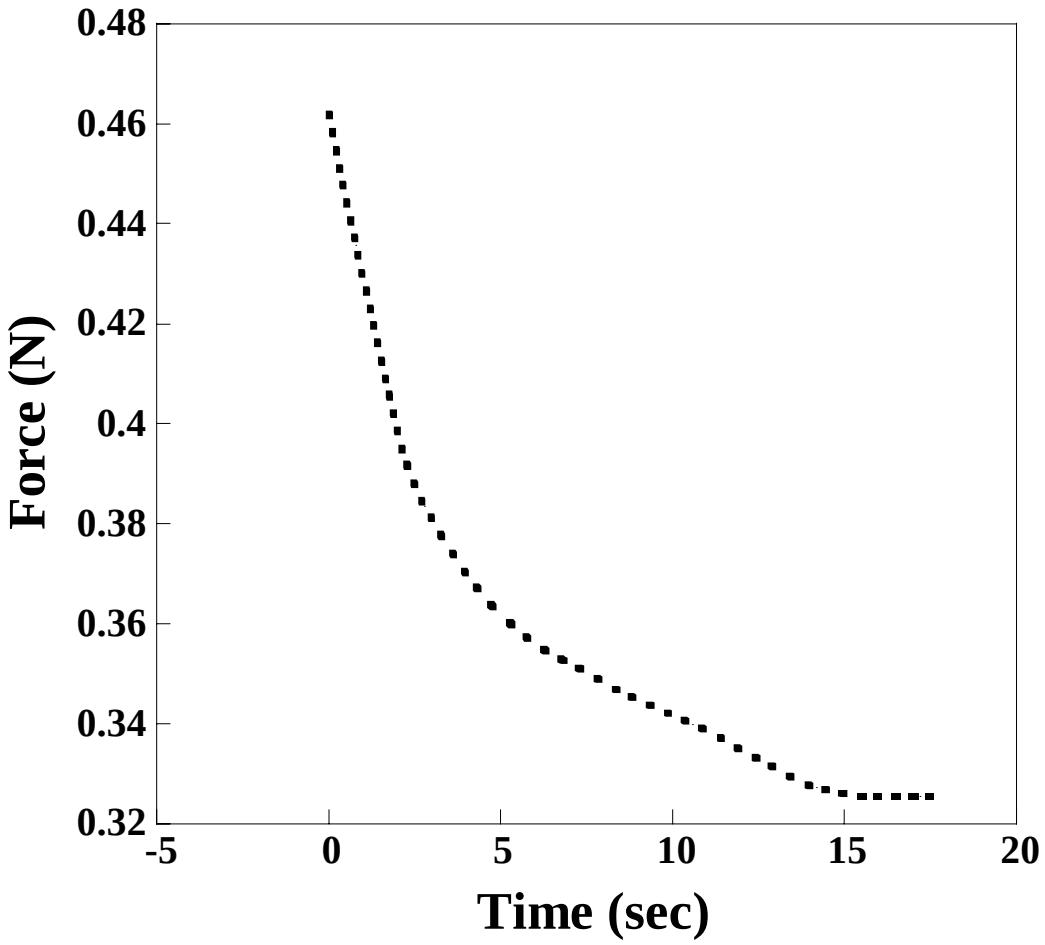

Figure 7.2: Demonstration of stress-relaxation experiment with the *HTMECH*; measurement taken on segmented polyurethaneurea film prepared at 95 mole % stoichiometry, cured at 90 ^{o}C.

cyclic loading experiments, hysteresis and permanent set information can be obtained. Stress relaxation experiments were obtained by subjecting the sample to a constant strain and monitoring the force with time. Force and time can be converted in to stress and strain using the equations developed in Chapters 2, 3 and 4.

All *HTMECH* measurements in this thesis were performed under ambient conditions. The mechanical properties of polymeric materials are very dependent on the temperature at which the test is performed. For example, a polymeric material can be classified as either a plastic or an elastomer depending on whether the final use temperature is below or above the glass transition temperature (T_g). Minor modifications to the design of the *HTMECH* described in Chapters 2 and 3 could allow measurements to be performed at different temperatures. Measurement temperatures can be controlled by connecting a temperature-controlled circulating bath to the *HTMECH*'s sample plate holder. Changing the temperature of the circulating liquid will change the temperature of the sample plate holder and sample plates. A major concern with this approach is the low thermal conductivity of polymers. The temperature profile at a grid position will vary radially with a maximum temperature at the edges where the polymer is in direct contact with the stainless steel sample plates. This concern could be circumvented by first sandwiching the polymer between thin aluminum sheets (~ 50 μm thick) prior to sandwiching between the sample plates. Preliminary results shown in Figure 7.3 demonstrate the feasibility of this idea. Figure 7.3 shows force-time profile taken on a thin (~ 20 μm thick) poly (D,L-lactide) (PDLLA) film prepared by casting a solution of PDLLA in chloroform solution. The measurement temperatures were varied by adjusting

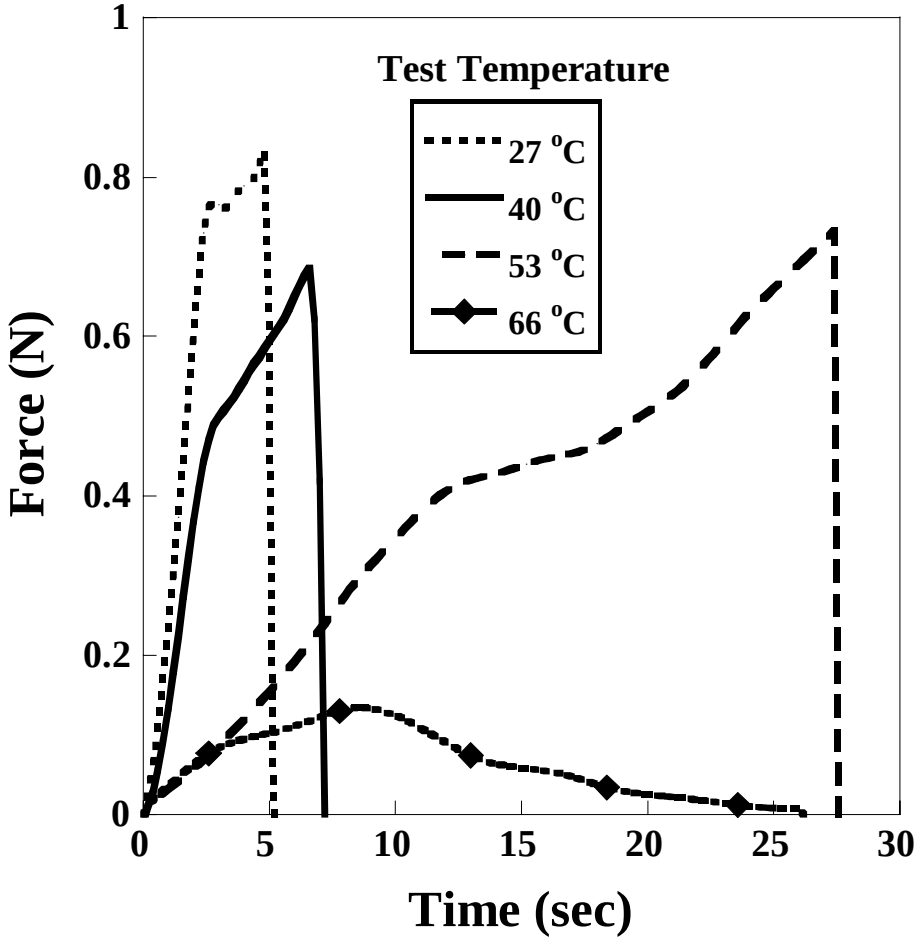

Figure 7.3: Effect of measurement temperature on the mechnical properties of poly (D,L-lactide) film using the *HTMECH*.

the temperature of the connected circulating bath. As show in Figure 7.3, the shape of the force-time profiles, force at failure (strength), and the time to failure (elongation at break) are all influenced by the measurement temperature. PDLLA is a plastic material with a very low degree of crystallinity and a has a reported T_g between 50 – 60 ^oC.[10, 11] Below the T_g, the force-time profiles of PDLA are representative of a plastic material: an initial elastic region, followed by plastic yield before failure. At 53 ^oC (between the glass transition temperature range), the shape of the curve is typical of a thermoplastic elastomers, with strain-induced crystallization. A significant increase in time to failure compared to the curves at 27 and 40 ^oC is also observed. Increasing the measurement temperature above the T_g to 63 ^oC resulted in a significant reduction in strength. These observations can be explained by the increased molecular motions at the T_g and the reduction in chain entanglement. Another possible means of controlling the measurement temperature could be by enclosing the entire apparatus in a controlled environment, where temperature and humidity can be controlled.

By combining the ability of the ***HTMECH*** to measure various mechanical properties (stress-strain, cyclic loading and stress relaxation) at different strain rates and at different temperatures, it is foreseeable that this device could be used to:

1. generate master curves using the time-temperature superposition principle.
2. provide information on a material's creep compliance. The stress relaxation modulus is related to the creep compliance through the Boltzmann superposition principle.[12]
3. determine hysteresis and time-dependent properties.

4. ultimately replace or serve as an alternative to expensive commercial instruments in academia and industry.

7.2.3 *Adaptation of HTMECH for High-Throughput Measurement of Polymer Adhesion to Different Substrates.*

The adhesion of polymers to different substrates is very important in many industrial processes. For example, the adhesion of thin polymer films on solid substrates is an integral part of the microelectronic industry. Also, accurate determination of the adhesive properties of pressure sensitive adhesives (PSAs) is very important in the adhesive industry. Several factors, including surface chemistry, geometry, strain and thermal history affect the strength of polymer adhesion. However, there is limited understanding of how these parameters combine to influence the overall adhesion. Combinatorial synthesis and high-throughput screening techniques present an opportunity to rapidly elucidate the combined effects of the above parameters on the adhesive properties of polymers. The 90 ^{o} peel test, which is a standard technique for measuring adhesive properties of PSAs have been modified recently for high-throughput screening.[13]

The geometry of the *HTMECH* makes this device amenable to high-throughput adhesion measurements. The geometry of the *HTMECH* is similar to the shaft-loaded blister test, an established technique for measuring polymer adhesion.[14] In order to make adhesion measurement using the *HTMECH,* the individual grid positions need to be independent of each other to allow debonding without interference from neighboring grid positions. Combinatorial techniques can be used to produce samples with combined variations in surface chemistry[15, 16], temperature[6] and substrate surface energy[17].

7.2.4 *Properties of Segmented Polyurethaneurea/Laponite® at High Particle Concentration*

In Chapter 6, segmented polyurethaneurea nanocomposites were prepared with reactive Laponite® particles and characterized. The mechanical properties of these nanocomposites were optimum at a particle loading of 1 wt. %. The synthesis of these nanocomposites suggests an obvious competition between amines attached to the surface of Laponite® and free amine in solution for the isocyanate in the prepolymer. At any given stoichiometry, the relative ratio of these two types of amines in the final solution can be varied by changing the overall reactive Laponite® concentration. It can be hypothesized that nanocomposite with different microstructures could result depending on the major source of amine in the final solution. At low particle concentration, the major contributor of amines is obviously the free amine in solution. However, at higher reactive particle concentration ($\geq$ 10 wt. %), the amines from the surface of the reactive particles could play a more significant role is dictating the final morphology of the nanocomposites. Since the mechanical properties of polymer/silicate nanocomposites are sensitive to changes in microstructure, such an investigation could shed light on the following question: *does the source of the amine or the overall stoichiometry determine the final properties of segmented polyurethaneurea/Laponite® nanocomposites*.

7.3 REFERENCES

(1) Sormana, J.-L., Meredith, J.C., High-Throughput Dynamic Impact Characterization of Polymer Films. *Mater. Res. Innov.* **2003,** 7, (5), 295.

(2) Sormana, J.-L., Chattopadhyay, S., Meredith, J.C., High-Throughput Mechanical Characterization of Free-Standing Polymer Films. *Review of Scientific Instruments* **2005,** 76, (062214).

(3) Wan, K.-T., Liao, Kin, Measuring Mechanical Properties of Thin Flexible films by a Shaft-Loaded Blister Test. *Thin Solid Films* **1999,** 352, 167.

(4) Sormana, J.-L., Meredith, J.C., High-Throughput Screening of Mechanical Properties on Temperature-Gradient Polyurethaneurea Libraries. *Macromol. Rapid Comm.* **2003**, 118.

(5) Sormana, J.-L., Meredith, J.C., High-Throughput Discovery of Structure Property Relationships for Segmented Polyurethaneureas. *Macromolecules* **2004,** 37, (6), 2186.

(6) Meredith, J. C., Karim, A., Amis, E.J., Combinatorial Methods for Investigations in Polymer Materials Science. *MRS Bulletin* **2002,** 27, (4), 330.

(7) Meredith, J. C.; Karim, A.; Amis, E. J., High-Throughput Measurement of Polymer Blend Phase Behavior. *Macromolecules* **2000,** 33, (16), 5760.

(8) Cotterell, B., Chen, Z., The Blister Test - Transition from Plate to Membrane Behavior for an Elastic Material. *Int. J. Fracture* **1997,** 86, 191.

(9) Wan, K.-T., Fracture Mechanics of a Shaft-Loaded Blister Test - Transition from Bending Plate to a Stretching Membrane. *J. Adhesion* **1999,** 70, 209.

(10) Meredith, J. C.; Amis, E. J., LCST Phase Separation in Biodegradable Polymer Blends: Poly(D,L-Lactide) and Poly(ε-Caprolactone). *Macromol. Chem. Phys.* **2000,** 201, 733.

(11) Urayama, H., Kanamori, T., Kimura, Y., Properties and Biodegradability of Polymer Blends of Poly(L-lactide)s with Different Optical Purity of the Lactate Units. *Macromol. Materials and Eng.* **2002,** 287, (2), 116.

(12) Aklonis, J. J., Macknight, W. J., *Introduction to Polymer Viscoelasticity*. Second ed.; John Wiley and Sons: New York, **1983**.

(13) Chiche, A., Zhang, W., Stafford, C.M., Karim, A., A New Design for High-Throughput Peel Tests: Statistical Analysis and Example. *Meas. Sci. Technol.* **2005,** 16, 183.

(14) O'Brien, E. P., Ward, T. C., Guo, S., Dillard, D. A., Strain Energy Release Rates of a Pressure Sensitive Adhesive Measured by the Shaft-Loaded Blister Test. *J. Adhesion* **2003,** 79, 69.

(15) Wu, T., Efimenko, K., Vlcek, P., Subr, V., Genzer, J., Formation and Properties of Anchored Polymers with a Gradual Variation of Grafting Densities on Flat Substrates. *Macromolecules* **2003,** 36, 2448.

(16) Wu, T., Tomlinson, M., Efimenko, K., Genzer, J., A Combinatorial Approach to Surface Anchored Polymers. *J. Materials Science* **2003,** 38, 4471.

(17) Ashley, K. M., Meredith, J.C., Amis, J., Raghavan, D., Karim, A., Combinatorial Investigation of Dewetting: Polystyrene Thin Films on Gradient Hydrophilic Surfaces. *Polymer* **2003,** 44, 769.

VITA

Joe-Lahai Sormana was born on September 4, 1977 in Sierra Leone, West Africa to Joseph Dauda and Margaret Sormana. Joe-Lahai attended Christ the King College and Prince of Wales before migrating to the United States in January, 1993. While in the United States, he graduated from Southwest High School (Minneapolis, MN) in 1995 and subsequently enrolled as an undergraduate in the Institute of Technology at the University of Minnesota. While pursing a Bachelor of Chemical Engineering degree at the University of Minnesota, he interned at 3M and H.B. Fuller Company during the summers. In 2000, he graduated with a Bachelor of Chemical Engineering degree from the University of Minnesota, and entered the Georgia Institute of Technology to pursue graduate studies in the School of Chemical and Biomolecular Engineering. As a graduate student, he was awarded both GEM and GAANN Fellowships. He obtained a Masters degree in Chemical Engineering from the Georgia Institute of Technology in 2002 under the guidance of Dr. J. Carson Meredith. After graduating with a Ph.D. in Chemical Engineering in August 2005, he will work at the Rohm and Haas Company in Spring House, Pennsylvania.